



University of HUDDERSFIELD

University of Huddersfield Repository

Kramer, Virginia

Design and development of an innovative controller for small wind turbines

Original Citation

Kramer, Virginia (2016) Design and development of an innovative controller for small wind turbines. Masters thesis, University of Huddersfield.

This version is available at <http://eprints.hud.ac.uk/30299/>

The University Repository is a digital collection of the research output of the University, available on Open Access. Copyright and Moral Rights for the items on this site are retained by the individual author and/or other copyright owners. Users may access full items free of charge; copies of full text items generally can be reproduced, displayed or performed and given to third parties in any format or medium for personal research or study, educational or not-for-profit purposes without prior permission or charge, provided:

- The authors, title and full bibliographic details is credited in any copy;
- A hyperlink and/or URL is included for the original metadata page; and
- The content is not changed in any way.

For more information, including our policy and submission procedure, please contact the Repository Team at: E.mailbox@hud.ac.uk.

<http://eprints.hud.ac.uk/>

DESIGN AND DEVELOPMENT OF AN INNOVATIVE CONTROLLER FOR SMALL WIND TURBINES

VIRGINIA KRAMER

A thesis submitted to the University of Huddersfield in partial fulfilment of the requirements for the degree of Master of Science by Research

The University of Huddersfield in collaboration with the Frankfurt University of Applied Sciences

April 2016

Copyright statement

- i. The author of this thesis (including any appendices and/or schedules to this thesis) owns any copyright in it (the "Copyright") and s/he has given The University of Huddersfield the right to use such copyright for any administrative, promotional, educational and/or teaching purposes.
- ii. Copies of this thesis, either in full or in extracts, may be made only in accordance with the regulations of the University Library. Details of these regulations may be obtained from the Librarian. This page must form part of any such copies made.
- iii. The ownership of any patents, designs, trademarks and any and all other intellectual property rights except for the Copyright (the "Intellectual Property Rights") and any reproductions of copyright works, for example graphs and tables ("Reproductions"), which may be described in this thesis, may not be owned by the author and may be owned by third parties. Such Intellectual Property Rights and Reproductions cannot and must not be made available for use without the prior written permission of the owner(s) of the relevant Intellectual Property Rights and/or Reproductions

Abstract

Recent demand for decentralized renewable energy on a small scale has led to the advancement of micro-wind turbines and customized control systems. In this work, the arising need for an innovative control system for small scale wind turbines particularly suited to a low wind speed urban environment has been addressed.

This work focuses on the stand-alone application of a vertical-axis wind turbine (VAWT) cross-flow prototype with the prospect of being able to grid-tie the system without any major modification to the control system. This constraint has led to the inclusion of a magnetic brake with various advantages over conventional braking methods which are addressed in the literature review of this thesis. Furthermore, the latter revealed lack of computerized models for the setup described, therefore it has been decided in this work to focus on software-based controller development utilizing models which have been validated by various experiments.

In the first development stage, a novel test bench prototype has been developed for prior evaluation of the brake characteristics. The prototype has been utilized for deriving a model dedicated to the low-speed region and for developing an efficient design strategy to be able to customize control systems for future small scale wind turbines.

The second development stage has been dedicated to the development of a suitable model for the wind turbine. Different modelling strategies are evaluated, i. e. the use of look-up tables (LUT), analytical models and CFD models, and the most suitable selected. This work uses an analytical model based on experimental data.

The third and last development stage leads to a software-based controller development approach with emphasis on two control modes common in variable speed wind turbine control: a. braking to a reference speed once the maximum allowable rotor speed has been reached or exceeded and b. braking to track the maximum power point when a turbine has not yet reached its rated power. A supervisory control template is given for future development for use in an embedded microcontroller design.

Contents

Abstract.....	3
Contents.....	4
List of Figures.....	6
Dedications and Acknowledgements.....	7
List of abbreviations.....	8
1. Introduction.....	9
1.1 Basic aerodynamics.....	11
1.2 Wind turbine design differences.....	14
1.3 Power transmission.....	15
1.3.1 Battery applications.....	17
1.3.2 Power grid connection.....	18
1.4 Speed control of wind turbines.....	19
1.5 Supervisory control.....	20
1.6 Modes of operation.....	21
1.6.1 Maximum power point tracking.....	21
1.6.2 Constant speed mode.....	22
1.6.3 Constant power mode.....	22
1.7 Motivation.....	22
1.8 Thesis organization.....	23
2. Literature review.....	25
3. Development of a novel brake controller.....	30
3.1 Magnetic braking.....	30
3.2 Literature review on magnetic brake models.....	32
3.3 A modelling approach from a control perspective.....	37
3.4 Prototype design suggestion.....	38
3.4.1 Hardware description.....	39
3.4.2 Software environment.....	39
3.4.3 Development of a novel sensor setup.....	40
3.4.4 Development of a novel power stage setup.....	44
3.5 Brake model comparison with experiment.....	50
3.6 Magnetic Field B.....	54
3.7 Complete Simulink model.....	56
3.7.1 DC Motor.....	56
3.7.2 Brake model.....	61
3.7.3 Complete model.....	61
3.8 Model verification.....	64
3.9 Controller development.....	65
3.9.1 Ziegler-Nichols tuning.....	66
3.9.2 HIL verification.....	66
4. Development of a novel wind turbine model.....	69
4.1 Wind turbine laboratory setup.....	69
4.2 Experimental evaluation of power output characteristics.....	70
4.3 Comparison of wind turbine modelling.....	72
4.3.1 Look-up table design.....	73
4.3.2 Analytical model.....	74
4.3.3 CFD-based control design.....	75
4.4 Development of a novel numerical wind turbine model.....	77
5. Development of a novel SSWT controller.....	82
5.1 Brake design and brake rating.....	82
5.2 Wind turbine dynamics and control requirements.....	85
5.3 Scaled brake model in Simulink.....	87
5.4 Braking to a reference speed above rated wind speeds.....	87
5.5 Maximum power point tracking.....	88
5.6 Supervisory control regime.....	89

5.7 Performance evaluation.....	90
5.7.1 Speed control.....	91
5.7.2 MPPT.....	92
6. Conclusions.....	94
6.1 Review of objectives and attainment.....	94
6.2 Original contribution to knowledge.....	96
6.3 Conclusions and future recommendations.....	97
Appendices.....	100
Bibliography.....	102

Word count: 30820

List of Figures

Figure 1.1: European map of annual wind speeds	10
Figure 1.2: Savonius rotor	14
Figure 1.3: Darrieus/ H-Rotor type	14
Figure 1.4: Angle of attack of an airfoil (cross-section)	21
Figure 3.1: Eddy currents in a thin metal sheet.....	31
Figure 3.2: Stepwise eddy currents.....	31
Figure 3.3: Magnetic brake assembly	38
Figure 3.4: US Digital Encoder.....	42
Figure 3.5: Encoder signal processing.....	43
Figure 3.6: Schematics of L298 bridge driver.....	47
Figure 3.7: Assembled L298 PCB.....	47
Figure 3.8: Second PWM driver stage.....	48
Figure 3.9: PWM losses from iron core.....	49
Figure 3.10: PWM output.....	50
Figure 3.11: Net braking force.....	51
Figure 3.12: Model comparison.....	52
Figure 3.13: Hysteresis: H-field – B-field	54
Figure 3.14: Motor equivalent circuit.....	56
Figure 3.15: Motor model subsystem.....	60
Figure 3.16: Brake model subsystem.....	61
Figure 3.17 Subsystem: sum of torques and calculation of angular speed.....	62
Figure 3.18 Subsystem: Feedback model.....	63
Figure 3.19 Top model: Feedback loop, controller and plant.....	64
Figure 3.20: Motor model verification.....	65
Figure 3.21: Plant model verification.....	65
Figure 3.22: HIL controller development.....	68
Figure 4.1: VAWT prototype.....	69
Figure 4.2: Torque transducer, gear train and generator.....	70
Figure 4.3: Set of power curves for VAWT.....	71
Figure 4.4: Three sets of λ -CP curves.....	72
Figure 4.5: Fit of maxima.....	73
Figure 4.6: Power feedback MPPT.....	74
Figure 4.7: Analytical VAWT model.....	75
Figure 4.8: Turbine and generator shaft model.....	79
Figure 4.9: Equivalent rotor subsystem.....	80
Figure 4.10: Equivalent shaft model.....	80
Figure 4.11: WT step response.....	81
Figure 5.1: Linear regression of torque curves.....	82
Figure 5.2: Magnetic core placement.....	84
Figure 5.3: Scaled brake model.....	87
Figure 5.4: Simulink model – max. speed mode.....	88
Figure 5.5: Simulink model: MPPT mode.....	89
Figure 5.6: Supervisory control.....	90
Figure 5.7: Speed control mode.....	91
Figure 5.8: Step response.....	92
Figure 5.9: MPPT mode.....	93

Dedications and Acknowledgements

I would like to thank my supervisors for having given me this unique opportunity of studying in this format. It was a pilot experiment and sometimes quite challenging to study abroad but I am hugely grateful for the experience now and all the knowledge I have gained. I would also like to thank my supervisors for their generous and enduring support. I hope the completion of this thesis has made it worthwhile.

List of abbreviations

HIL:	Hardware-In-the-Loop
LUT:	Look-Up-Table
HAWT:	Horizontal Axis Wind Turbine
VAWT:	Vertical Axis Wind Turbine
TSR:	Tip Speed Ratio
SSWT:	Small Scale Wind Turbine
WECS:	Wind Energy Conversion System
VSWT:	Variable Speed Wind Turbine
MPPT:	Maximum Power Point Tracking
PCB:	Printed Circuit Board
PDE:	Partial Differential Equations
CFD:	Computational Fluid Dynamics
LQG:	Linear-Quadratic-Gaussian (control)

1. Introduction

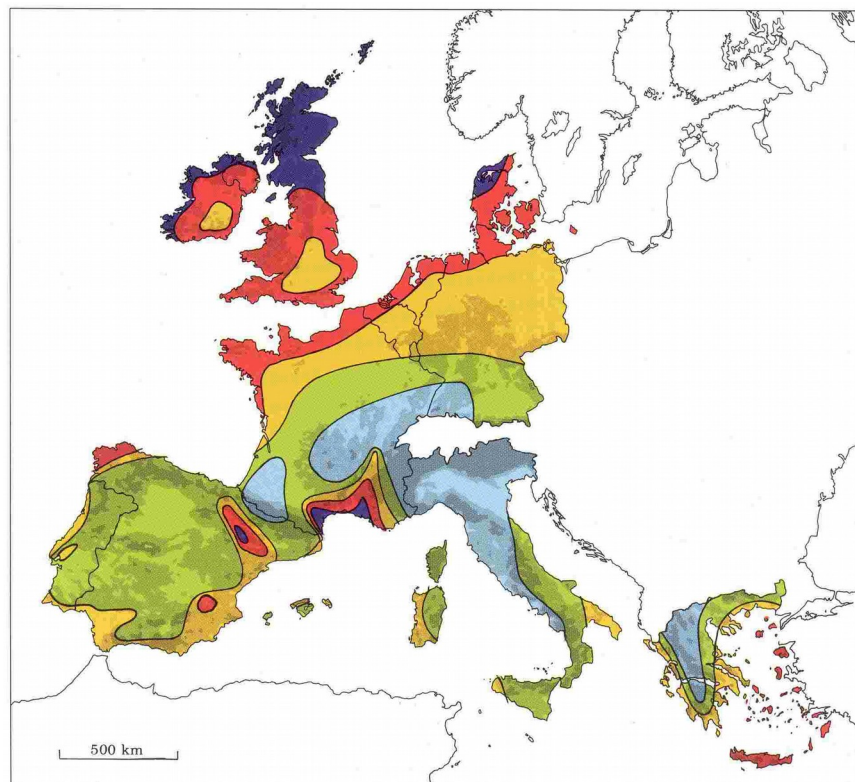
Our demand for energy keeps growing due to our increasing standard of living and the exponential growth in the world population. While conventional resources have been used extensively over the past century and have covered our needs thus far, non-depletable sources of energy will increasingly need to be integrated with, and will ideally replace, exhaustible resources in the long term. However, an optimal solution has yet to be found which fully exploits the potential of renewable energy. Current technologies cannot entirely meet peak demand as their power output varies and often it cannot be guaranteed that supply can easily be located in proximity to large cities. In addition, due to the stochastic nature of the sources and the energy conversion process, the grid connection requirements are often difficult to meet as they ask for a certain standard of electrical energy quality with reference to factors such as reactive power, flicker and harmonics etc. [1].

This work focuses on wind turbines that generate electricity on a small scale. Their large counterparts, onshore and offshore wind turbines in particular, have to withstand extreme weather conditions and therefore require a rugged design for larger wind speeds at greater heights. A high power output can be a desirable advantage and if these types of wind turbines are distributed and combined in wind farms, large variations in output can be levelled out. Volatile output can be caused by wind stagnation, but also by locally occurring faults and the emergency shut down of any electricity generating plant [2]. However, energy distribution on a large scale requires a good power transportation infrastructure which is expensive and also prone to losses. Decentralized electricity generation is therefore increasingly gaining interest since this avoids the long distances between end users and electricity plants. A widely distributed and decentralized network still offers the aforementioned advantages of levelling out volatile energy output and also helps improve the efficiency of the power grid when a major part of locally occurring power demand is directly provided by individual domestic wind turbines or other small-scale renewables [3]. Combining what is called "micro-generation" with a future "smart grid" would also ensure short distances between supply and demand through use of an intelligent network that communicates with both end user devices and supply sources [4]. Also, stand-alone operation of wind turbines and other technologies such as solar power to supply a home network helps to make some network infrastructure redundant.

Creating energy on a small scale through the utilization of small wind turbines would also provide a more cost-effective solution in part due to the absence of risky extreme weather conditions that occur at greater heights. If system costs could be reduced while offering a promising annual energy yield, there would be an incentive for buyers to invest in turbines for their homes or for enterprise premises. So far, small wind turbines have already proved useful in remote-network applications, for example, on islands or remote mountain ranges.

Undeniably, the cost of a wind turbine would be a key deciding factor for buyers to invest in their private property, as well as the rated turbine power output (which will be explained later in this chapter). Currently, pole-mounted wind turbines for exposed areas can yield up to 5–6 kW of rated power, whereas building-mounted wind turbines range from about 1-2 kW, depending on size [5]. Generally, small-scale generation is considered to be up to 50 kW [6].

Like Denmark, the UK is one of the windiest regions in Europe. Figure 1.1 shows a wind map of Europe with average annual wind speeds at 50m above ground level [7]. Wind power generation in Denmark accounted for about 18% of total national energy production in 2009. Despite having less wind on average, Germany has still reached 6.5 % in the same year; by contrast, the inclusion of wind energy in the UK has only contributed an annual yield of 2.48% of total electricity generation [8]. Clearly there is a large potential to be harnessed.



Wind resources ¹ at 50 metres above ground level for five different topographic conditions									
Sheltered terrain ²		Open plain ³		At a sea coast ⁴		Open sea ⁵		Hills and ridges ⁶	
$m s^{-1}$	Wm^{-2}	$m s^{-1}$	Wm^{-2}	$m s^{-1}$	Wm^{-2}	$m s^{-1}$	Wm^{-2}	$m s^{-1}$	Wm^{-2}
> 6.0	> 250	> 7.5	> 500	> 8.5	> 700	> 9.0	> 800	> 11.5	> 1800
5.0-6.0	150-250	6.5-7.5	300-500	7.0-8.5	400-700	8.0-9.0	600-800	10.0-11.5	1200-1800
4.5-5.0	100-150	5.5-6.5	200-300	6.0-7.0	250-400	7.0-8.0	400-600	8.5-10.0	700-1200
3.5-4.5	50-100	4.5-5.5	100-200	5.0-6.0	150-250	5.5-7.0	200-400	7.0- 8.5	400- 700
< 3.5	< 50	< 4.5	< 100	< 5.0	< 150	< 5.5	< 200	< 7.0	< 400

Figure 1.1: European map of annual wind speeds [7]

Two categories of wind turbines exist: horizontal and vertical axis wind turbines, both of which will be explained in more detail in this chapter. Current vertical axis wind turbine designs are mechanically unsuitable for higher power output ranges as they can only be installed close to the ground. Furthermore, their material costs per square meter outweigh the theoretical advantage of exploiting strong wind gusts [9]. On a smaller scale, however, selection of either design can be considered since both turbine types offer advantages and disadvantages. A major advantage of utilizing a horizontal axis wind turbine (HAWT) is the considerably larger power coefficient; however, their audible noise level may be an undesirable side effect in residential areas. Another drawback may be their slower reaction when dealing with wind direction shifts. Looking at the wind source and the surroundings, a choice can be made depending on the proposed location of the wind turbine. Wind patterns between buildings, for example, have proven to be stronger but more turbulent [10], therefore, a vertical axis wind turbine (VAWT) would be more suitable. A VAWT can capture the wind from any direction, therefore these types of wind turbines are able to process turbulent air flow. Selecting a turbine for deployment on roof tops, however, depends again on the urban environment. If there are high-rises surrounding the building in question, it is still advantageous to utilize a VAWT. If the building stands in isolation and is tall enough, a HAWT may be a better option. The expected wind speeds, wind directions shifts and turbulence are all important deciding factors for choosing a wind turbine type and its rating. Both vertical and horizontal turbine designs have also been compared in terms of their performance in wind farms. HAWTs need to be set apart about five turbine diameters in order that each turbine can harness the full wind speed and is not exposed to the wind shadow of an adjacent turbine [11]. The effect of a rotating VAWT, however, could potentially be beneficial for a neighbouring turbine in close proximity. This is known as the "von Karman vortex street", a flow phenomenon of regular eddy patterns that occurs at a certain range of flow velocities, or at Reynolds numbers larger than 90, respectively. Reynolds numbers specify the ratio of inertial to viscous forces in fluid flow. If turbines were spaced apart correctly and at an appropriate angle, the overall average power coefficient could likely be improved. A similar effect can be observed in nature in a school of fish [12].

1.1 Basic aerodynamics

Typical wind turbines, HAWT, account for the majority of installed wind turbines today and are mainly deployed for large-scale installations. Currently, sizes range from a few Kilowatts to approximately 7 Megawatts. However, these numbers have to be treated with care. While the aforementioned range seems to give a more intuitive feel for a wind turbine's capacity, a direct measure would be the swept area as shown below in equation 1.1. The power output ratings typically refer to the rated power of the wind turbine generator rather than that of the wind turbine itself; in that regard, the swept area is technically more meaningful

and hence widely used when comparing wind turbines [13]. Whether or not the generator rating corresponds to the full wind turbine power rating depends on the type of generator configuration. For example, a generator stator connected to the grid using a frequency converter would require the generator to have the same ratings as the wind turbine [14].

As mentioned above, the swept area A directly relates the power available in the wind to the power output of the wind turbine [15]:

$$P_w = \frac{C_p}{2} \cdot \rho \cdot v_w^3 \cdot A \quad (1.1)$$

with C_p the power coefficient of the turbine in percent, ρ the density of air and v_w , the wind speed. Equation 1.1 can be derived from the kinetic energy equation:

$$E_{kin} = \frac{1}{2} \cdot \Delta m \cdot v^2 = \frac{1}{2} \cdot \rho \cdot R^2 \cdot \pi \cdot \Delta L \cdot v^2 \quad (1.2)$$

where the volume of a cylinder differential multiplied with the air density equals the differential mass of the volume. Equation 1.2 can be transformed into the power equation above since the kinetic energy divided by a time differential yields the wind speed on the right hand side of the equation. The latter is the exact speed which the air molecules travel with through the differential length:

$$\frac{E_{kin}}{\Delta t} = \frac{1}{2} \cdot \rho \cdot A \cdot \frac{\Delta L}{\Delta t} = \frac{1}{2} \cdot \rho \cdot A \cdot v^3 \quad (1.3)$$

Equation 1.1 also contains the power coefficient, i.e. the factor of power extracting efficiency of a given wind turbine. However, the mechanical power output is not proportional to the cubed wind speed as the coefficient C_p varies depending on the wind speed and the angular speed of the rotor. The variation of C_p therefore depends on any load attached. This has led to another measure used in wind engineering, the tip-speed ratio, TSR (λ), as mentioned before, which relates the tangential wind speed of the rotor tip to the wind speed:

$$\lambda = \frac{v_{tan}}{v} = \frac{\omega \cdot r}{v} \quad (1.4)$$

The TSR accommodates both the wind speed as well as the rotor speed and therefore allows a direct relationship between the wind and the mechanical turbine output. Typical values for drag-based turbines are $\lambda < 1$ and for lift-based turbines are $\lambda > 1$. The types of wind turbines and how they are driven by the wind will be given in the section following. If a wind

turbine is operated at variable speed for optimized energy capture, the TSR is constant and in this case the rotational speed is proportional to the wind speed. The tip speed ratio is of particular importance for analytical models of wind turbines.

A wind turbine rotor can only extract a limited amount of the full kinetic energy from the wind and convert it into rotational energy. This is owing to the fact that air molecules passing through the wind turbine “block” subsequent colliding molecules which cannot provide the same amount of kinetic energy as before. A theoretical limit was analytically found by a German physicist, Albert Betz. He discovered that the power efficiency, expressed by the power coefficient and called the “Betz” limit, can theoretically reach a ratio of $16/27 \approx 59\%$. In practice, however, maximum efficiency typically ranges from 35 – 45% for a HAWT [16].

The power coefficient for a VAWT is typically lower than that of HAWT, in particular for drag-based wind turbines. But as mentioned before, HAWT are also practically limited by the design of the turbine rotor as well as the presence of the tower, and for this reason, the Betz coefficient only represents a theoretical limit which is based on idealized assumptions such as a thin rotor lacking a hub [14].

If a HAWT is to be described analytically, the dependency of the power coefficient on the TSR and the rotor pitch angle has to be found since the other parameters of equation 1.1 are known, assuming constant air density. If the full potential of a given wind turbine is to be harnessed, the pitch angle β is left at its maximum, i.e. at $\beta = 0$.

VAWT can be assumed to exhibit the same type of non-linear behaviour, usually expressed by a sinusoidal equation. The power coefficient of Darrieus type rotors were shown to relate similarly to the TSR [17]. According to other review studies, the Savonius turbine exhibits the same qualitative result [18] [19].

Therefore, the dependency of the power coefficient on the TSR has to be found. An example of a HAWT power coefficient using a fitted equation and an analytical approximation would be [20]

$$C_p(\lambda, \beta) = (0.44 - 0.0167\beta) \sin\left[\frac{\pi(-3+\lambda)}{15-0.3\beta}\right] - 0.00184(-3+\lambda)\beta \quad (1.5)$$

With $\beta = 0$, the power coefficient equation would simplify to

$$C_p(\lambda) = 0.44 \cdot \sin\left[\frac{\pi(-3+\lambda)}{15}\right] \quad (1.6)$$

1.2 Wind turbine design differences

Wind turbines are distinguished by their angle of rotation relative to the ground. HAWT are largely driven by lift and usually need a mechanism for following the wind direction so that their blades are perpendicular to the direction of the wind. One category of HAWT, the downwind turbine, does not require to be directed towards the wind as these types follow the wind automatically. Despite having to be guided in order to face the wind, the upstream HAWT is by far the more common. The rotor is only indirectly hindered by the wind shadow of the tower which is owing to the fact that the turbines are driven by the opposing wind force. Clearly, this is not the case for downwind turbines and the resulting periodic variations in output torque make these turbines more prone to mechanical failure.

VAWT rotate at 90 degrees relative to ground and can either be driven by drag or by a combination of drag and lift. Pure drag forces are parallel to the wind direction, i.e. the blades are literally dragged by the wind. Lift forces are directed upward and perpendicular to the fluid flow. Unlike modern HAWT, VAWT designs vary greatly. Three basic designs of VAWT exist: Darrieus, Savonius and the H-rotor, albeit the H-rotor was also patented with the Darrieus type and functions similarly. Both the Darrieus and the H-rotor are driven by lift as well as drag. Figure 1.2 - 1.3 show both types.

Savonius-Rotor

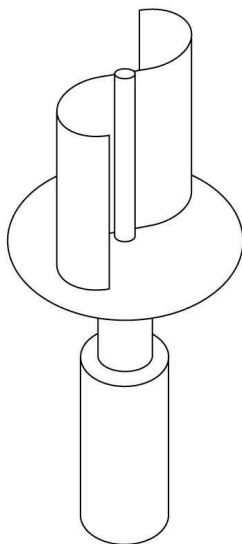


Figure 1.2:
Savonius
rotor [74]

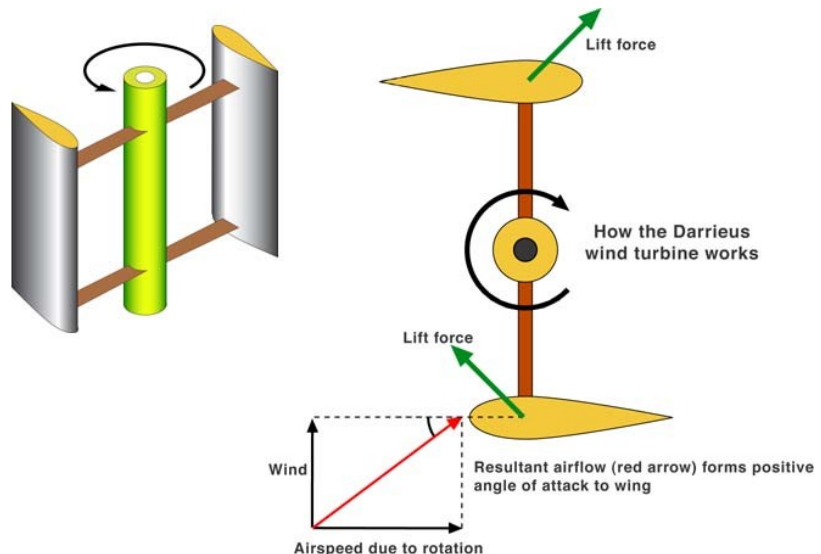


Figure 1.3: Darrieus/ H-Rotor type [75]

A Savonius rotor is purely driven by drag and comes in a variety of forms, such as the anemometer. Often, the blades have scoop-like shapes that capture the wind. One major

disadvantage of drag type VAWT is that the other side facing the wind is being driven upwind, i.e. pushed towards the wind source and hence the overall power efficiency is reduced. Attempts have also been made to improve this inherent disadvantage by using inlet guide vanes [21]. Without any modification to the basic design, only a considerably lower power coefficient of about $C_p=4/27 \simeq 15\%$ can be achieved [22]. However, Savonius rotors are self-starting whereas the Darrieus and the H-rotor do not have a sufficiently high starting torque to accelerate them to the reference speed. Attempts have been made to resolve this issue by combining the Savonius and Darrieus type rotors into a hybrid model. A more recent invention, the patented Vortexis turbine, is self-starting and can achieve a power coefficient of 35% alone [23].

1.3 Power transmission

So far, only the mechanical conversion part of a wind energy conversion system has been described. Purely mechanical systems were used historically for purposes such as grinding grain or pumping water, which was commonplace in the Netherlands as the land needed to be drained in order to be cultivated. Another example included pumping water with multi-blade wind turbines from deep underground in the US. If electricity is to be generated, the mechanical energy has to be converted using a generator. Depending on the application, i.e. whether the turbine needs to be operated with a fixed or variable speed, or whether the turbine should be operated stand-alone or grid-tied, different generators can be utilized.

In larger wind turbines, synchronous and induction machines are used. Synchronous generators (or alternators) have a fixed armature and a rotating field which is generated by a DC voltage. The output voltage of the stator connectors can be varied by controlling the field of the rotor. If a synchronous generator is to be connected to the grid, the voltage, the frequency and the phase angle have to match that of the grid, i. e. the generator has to be synchronized in order to avoid short circuits. This type of generator can be used in conjunction with an AC to AC inverter, if tied to the grid, which will be explained in more detail after this section.

In an induction generator, or asynchronous generator, the rotor is merely used for "cutting" the rotating field of the stator windings, which in turn generates a voltage in the stator windings if operated correctly. If the generator is driven by a turbine, eddy currents are induced in the rotor which generate a field that feeds electricity into the grid. The rotor has to turn at a frequency that lies above the synchronous frequency of the generator. The speed difference is called slip which in a cage rotor induction machine is proportional to the active power supplied to the grid.

Three types of induction motors exist for wind turbine applications; the cage rotor, the wound rotor and the doubly-fed induction machine (DFIG). If directly connected to the grid, the cage rotor is tied to the grid frequency, and rotates at a proportional speed that depends on the number of pole pairs deployed. This type of induction machine configuration is prone to mechanical wear, particularly on the gear box, if used, as wind gusts induce high torque pulsations. The torque peaks are directly related to the currents fed into the grid and are a result of the forced frequency operation. To limit the current and torque loads, soft-starters using thyristor technologies, are utilized [24]. Furthermore, two configurations of pole pairs can be used for lower and medium to high wind speeds, typically eight poles and four to six poles, respectively [1]. The stator of a cage rotor induction machine can also be connected to the grid using a full power electronics converter for variable speed operation. A wound rotor machine allows control of the rotor speed using either slip rings and resistors or a partially rated power converter. The latter configuration allows variable speed control of about 30% of the nominal speed by only using a converter with 30% of the full rating of the generator [24].

In a variable speed configuration, the aforementioned asynchronous generator can be used for grid applications with a fully rated power electronic system. In short, this means that the entire electricity generated has to run through a full power electronic system, i.e. the ratings of the wind turbine have to match the ratings of the electric conversion system. The disadvantages of a fully rated power electronic system are the added costs, in particular for the higher range of wind turbine ratings and also the losses induced in the semiconductor devices. To circumvent this problem, other solutions exist that optimize the cost and performance of the overall electromechanical system for a grid connection. An example would be the induction generator with a wound rotor where the electronic conversion system only has to be partially rated due to the direct grid connection of the stator, as mentioned before. However, being able to fully control the rotor speed by running the generated voltage through a back-to-back inverter system optimizes the power output further and enables the wind energy conversion system to operate more smoothly as wind fluctuations have less impact on the conversion chain. Usually, DFIG generators are used for the higher end of wind turbines which produce power in the MW range since semiconductor devices become very expensive for these ratings [24].

It is common practice to use AC generators for small-scale wind turbines as they can also be used in stand-alone operation if a connection to the utility grid is not planned. This type of generator is also referred to as alternator and is commonly used in cars, for example, to continuously charge the battery while driving. Depending on the application, the resulting

AC voltage can be converted further to a DC voltage by rectifying the three-phase output and possibly using a filter to reduce the ripple.

However, an asynchronous generator can also be used in stand-alone operation if a capacitor bank and an AC generator or a battery with a DC-AC converter is used for providing the reactive power needed for the excitation field. The generator is also able to start up with enough remaining magnetization of the iron in the stator.

A trend for small scale wind turbines (SSWT) is to use brushless alternator-type generators, either with permanent magnet fields or a self-excited variant where the DC field is generated by an auxiliary generator and rectification circuit enclosed. The disadvantage of the brushless solution is that the DC field of the rotor is fixed, i. e. the amplitude of the output cannot be changed by a field increase or decrease. However, an interfacing circuit and a transformer can take care of interfacing the wind turbine system with the grid, if required, which is explained in more detail in section 1.3.2. Another trend is to use induction generators for grid interfacing due to the direct stator connection which does not need synchronization. Also, an induction generator may be a cheaper solution for a SSWT system compared to an AC generator.

1.3.1 Battery applications

When a battery is used, the wind turbine is neither tied to any grid frequency nor does the voltage have to be converted back to a fixed AC voltage. Also, a battery can effectively be used as a buffer, provided the battery has not reached its full capacity. Currently, the most compact and efficient batteries are Lithium-Ion batteries. They are used in numerous devices, ranging from portable electronic consumer goods, mobile equipment like notebooks, smartphones, tablets and the like, to power tools and even more recently, in electric cars. If a battery is to be utilized in a renewable energy project, it is of great importance to use an intelligent charging system that ensures the longevity of the battery. Prices are significant when looking at higher capacity storage, as with electric cars [25], where costs are estimated to be approximately £ 7,000 for a smaller sized car. The objective in using a charging circuit is to continuously monitor the battery voltage and control the current input; particularly under- or over voltage have to be prevented by the circuitry. If budgeting permits, a second battery would be advantageous if the wind turbine continues to run once one battery has reached its full capacity. Other commercially available solutions of wind energy conversion systems (WECS) use a dump load for excess converted wind energy.

1.3.2 Power grid connection

As mentioned before, grid-tying a synchronous generator requires the power electronics unit to take care of synchronizing the electrical output of the generator to the grid, i.e. to ensure, that no voltage difference, frequency deviation or phase shifts occur which would generate current surges, possibly damaging the generator or any components for connection to the grid (wiring, any power electronics). Depending on the generator chosen, other variables that require control action are the active and reactive power of the generator, the DC-link voltage in an AC to AC inverter as well as the power factor on the grid side [1].

DFIG and their electronic power control units are the most widely used variable-speed WECS. In this configuration, the three phases of the stator are directly connected to the grid whereas the rotor windings are connected through an AC to AC inverter, hence the term "doubly-fed". Depending on the current control action of the conversion system, the rotor either draws or injects power and the stator permanently outputs power to the grid. Due to the generator control governed by the power electronics converter, the speed of the generator and therefore the turbine rotor shaft speed can be varied significantly. Depending on the converter, a certain range around the synchronous speed of the generator rotor can be achieved, typically $\pm 40\%$ [1].

An AC to AC inverter, also named a back-to-back inverter, is needed in a WECS for two reasons. As already mentioned, an inverter setup allows control of the electrical parameters mentioned previously, as well as the rotor speed. However, an inverter is also responsible for interfacing incompatible power systems. If a connection to the grid using a synchronous generator is aspired, a conversion via a DC-voltage link can be used to match the frequency of the grid. The highly stochastic nature of the wind patterns is reflected in the response of the wind rotor and therefore in the generator, i.e. a fluctuating rotor frequency as well as a varying AC generator voltage frequency result. An AC to AC converter takes care of converting the varying voltage to a DC voltage using a rectifier circuit and other components to control the reactive power of the generator circuit as well as filtering elements to smooth the DC level. Depending on the type of conversion, i.e. a voltage-source or a current-source conversion, the filter being used is a capacitor in parallel and an inductance in series, respectively. The DC conversion back to the AC requirements of the grid can be achieved by utilizing digital control of power switching devices, called insulated-gate bipolar transistors (IGTB). The required sine-wave is modulated by varying the on-off state such that the root mean square value of the modulating wave matches the sine wave required by the grid. The advantage is obviously that such a power stage can be controlled digitally; however, it is important that the harmonic frequencies induced by the square

waveform do not affect the grid too much, i.e. the power factor should be close to 1. The latter does not refer to a phase shift between current and voltage but instead, it is a measure of the fundamental current wave component compared to the total current.

In a SSWT, a full AC to AC inverter may be utilized since the ratings of smaller wind turbines do not require a bulky and expensive power circuitry. An example would be an interfacing circuit/ transformer mentioned in connection with the brushless alternators. First, a controller or circuitry has to take care of fixing the amplitude of the generated voltage. The next step is to rectify the AC voltage and to filter the resulting DC voltage. Then, a controller or a chopping circuit has to convert the DC voltage to a 50 Hz equivalent AC voltage which has to be transformed afterwards using a variable transformer (such as a transformer with a slidable iron core) to meet the grid requirements.

1.4 Speed control of wind turbines

The previous introductory sections shed light on the fact that variable speed control of a wind turbine is essential for a smooth operation of the wind turbine and also for being able to extract as much energy from the wind as possible. Furthermore, for safety reasons, it is a requirement to limit the speed as well as the generated power once the rated power of the wind turbine is exceeded. The wind turbine as well as the generator need to be protected against adverse weather conditions so that the mechanical structure is not damaged and the generator does not inject power above its rating, likely resulting in exceeding the allowable thermal limit. Furthermore, a property unique to VAWT is that torque pulsations occur depending on the design which may impose a necessity to dampen the spinning rotor accordingly.

Traditionally, fixed speed wind turbines had mechanical means of controlling the power injected which are still in use in variable speed wind turbines (VSWT): aerodynamic stall of the rotor blades after a critical wind speed is exceeded which is intrinsic in the rotor design; active stall control where a constant speed is maintained while the amount of generated power is limited; pitch control where the rotor blades are rotated such that the amount of wind energy capture is actively controlled by the blade position. Furthermore, a yaw mechanism can be used to turn the rotor facing or out of the wind, depending on the actual measurement readings and control requirements. If the wind turbine should not be exposed, it is turned parallel to the wind so that the turbine stops rotating; if power extraction should be maximized, a guide vane can be used to turn the rotor such that the swept area faces the wind perpendicularly.

As mentioned before, the speed of a wind turbine can also be controlled via the electric system using power converters or other control options which will be discussed in more

detail in the literature review of this thesis. A last possibility for controlling the rotor speed exists, which is mostly used for aiding the electric braking system once the speed or power ratings are exceeded: either a friction brake or an electromagnetic brake can be used to support braking the wind turbine when operated above its maximum ratings.

For VAWT, a pitch or stall mechanism may be out of question depending on the aerodynamic design of the turbine. As mentioned before, a wind following mechanism is not needed since the turbine can capture the wind from any direction. However, this inherent advantage also means that the turbine cannot be "taken out" of the wind. Therefore, braking electromagnetically, i. e. by load variation of the generator and/ or mechanically are the most practical options for a VAWT.

1.5 Supervisory control

The hierarchical top unit of a control system for a VSWT is the monitoring unit which is also referred to as supervisory control. For supervisory control, the possible power output for a wind turbine is divided into regions, depending on the wind input. Accordingly, the wind speeds at which the turbine starts generating power is called the cut in-wind speed; the region where power generation starts is denoted by the rated wind speed and the region where wind speeds exceed a wind turbine's maximum power ratings is the furling, cut-out or maximum wind speed. As mentioned before, each wind turbine is specifically suited for a particular wind site. The power regions mentioned above require different control strategies, hence the term "supervisory control". The objective for the region between cut-in and the rated wind speed is to extract as much power as possible as the wind turbine is not operating at its full capacity yet and power output varies with rotor speed changes. This control scheme is also referred to as "Maximum Power Point tracking" (MPPT) and is utilized by VSWT [26].

Wind turbine control requires a hierarchy of computer programs as well as control algorithms for the modes of operation previously described. The level of complexity increases when dealing with wind parks. A dedicated program is responsible for supervisory control over the different modes of operation and for initiating the appropriate control algorithms, once a mode can be established successfully. In a lot of wind turbines, variable speed control for MPPT is achieved by using constant pitch and controlling the tip speed ratio λ which has to be held constant at the optimal TSR. Pitch control refers to the angular position of the rotor blades about their rotational axis. Most control strategies for the constant power mode when the rated wind speed is exceeded operate with a variable pitch algorithm since the rotational speed and therefore the TSR can only be limited to a certain point, i.e. the power coefficient of the wind turbine is continuously lowered with increasing wind speeds by changing the angle of attack (see figure below). The angle of attack

determines the amount of lift the blade experiences. This process is referred to as furling [26].

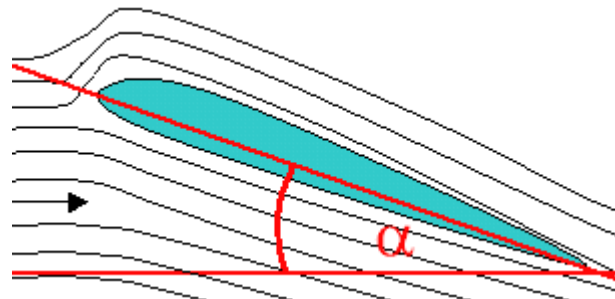


Figure 1.4: Angle of attack of an airfoil (cross-section) [76]

To account for an increasing wind speed in the constant speed region, the TSR has to be lowered accordingly. The limitation of power input is of particular importance when wind speeds are higher since the turbine extracts power which increases with the cube of the wind speed, as introduced in section 1.1 about aerodynamic power extraction.

1.6 Modes of operation

In this section, the three different modes that have proved expedient in supervisory wind turbine control are introduced in the order according to increasing wind speed ranges. For MPPT, three common algorithms are explained. The goal of the constant speed and constant power mode are explained as well.

1.6.1 Maximum power point tracking

In literature, three common MPPT methods are described, namely perturbation and observation, wind speed measurement and power signal feedback [20]. With perturbation and observation, the rotor speed is changed slightly and the difference in power output measured. Depending on the sign of the power difference, the controller determines whether the shaft speed should be increased or decreased. However, the author concludes that this scheme is not suitable for a slowly reacting turbine shaft with a higher inertial load as the system cannot follow a sudden change in wind speed. The second method, wind speed measurement, relies on accurate sensing of the wind speed. In order to achieve the accuracy, it has to be kept in mind that the wind flow in the immediate surrounding of the wind turbine may be turbulent and that further away, the measurement may differ from the actual wind speed that the WT is exposed to. Therefore, a sensor cluster should be favoured which takes readings at different locations close to the WT. With the wind speed and the

rotational speed, the TSR can be determined and compared to a reference TSR, the maximum C_p point given by the analytical model. The third method that the author suggests is the power signal feedback scheme, which uses a 1-D LUT for the ω - P_{opt} curve obtained by using a fit through all maximum power points. Instead of a feedback path using ω , the actual power output of the turbine is fed back and compared with the reference power obtained by a table lookup using ω .

1.6.2 Constant speed mode

In this mode, the maximum rotational speed of the rotor is reached and should not be exceeded. Therefore, the variable to be controlled is the angular speed ω . The lower boundary for this mode has to be defined according to the wind turbine's mechanical behaviour at no-load conditions and higher wind speeds. The upper boundary is given by the generator's maximum power ratings and the rated wind speed for this operating point has to be found.

1.6.3 Constant power mode

Once the rated wind speed is reached, the power of the generator has to be kept constant which can be achieved by braking the turbine to a speed that corresponds to a TSR below the optimum TSR until the reference power is reached. This essentially means that the power coefficient of the wind turbine is contentiously lowered with increasing wind speeds. If braking does not suffice to reduce the efficiency, the blades have to be pitched.

1.7 Motivation

This project came about with the increased interest in renewable energy on a small scale and the arising need for an innovative control system for a novel VAWT cross-flow design that was developed prior to this work to specifically suit a low wind speed urban environment [27].

From the generic description about wind turbines and their small-scale counterparts, a number of key matters have been determined in the introductory chapter that are further examined in this work.

The first mention in this introduction concerns stand-alone operation of wind turbines, with the advantage of servicing micro-demand and needing less grid infrastructure. This work therefore focuses on stand-alone applications. The developed system can also be advantageously used for future deployment in a grid-tied system if excess energy is stored in a battery. The particular focus of the current project is repeatability, i. e. the flexibility in the development since wind turbines are custom-selected depending on the wind site expectations. The routines developed in this project are easily adapted and tailored to a specific wind turbine design.

Since this project has been planned with the intention of developing a complete software-based model, it is essential that different modelling strategies of the VAWT design are evaluated and the most suitable choice selected.

The next important issue addresses variable speed control. From the braking methods available, a selection is made that allows independent speed control of the turbine which in turn allows changing remaining transmission components of the system to create or test other setups. Furthermore, since the aerodynamic behaviour of most VAWT designs cannot be changed easily, a robust solution has to be found which can aid to efficiently increase the braking force when dealing with high wind speeds in constant speed mode as well as in constant power mode as mentioned in the section about supervisory control.

Another important focus of this work concerns optimized energy capture. As mentioned in connection with the wind turbine characteristic TSR and the inherent lower power coefficient of drag-based VAWT, it is of particular importance that the wind turbine be operated in optimal conditions. Since the design of a VAWT control system calls for an inexpensive solution, it is deemed necessary to find a braking mechanism that can fully meet all of the requirements mentioned so far. Robust braking also means that with an initiated control procedure the torque pulsations inherent to some VAWT designs are dampened.

1.8 Thesis organization

This section gives an overview about the basic outline of the thesis.

Chapter One

Chapter One has introduced wind energy in the context of an urban environment and the potential of the renewable source in the UK. The necessity for efficient and inexpensive control strategies for small scale wind turbines is discussed and key matters based on the latter are highlighted which form the basis of this thesis.

Chapter Two

This chapter provides a review of existing literature about different braking strategies in the context of multi-mode operation and their suitability for VAWT. The advantages are contrasted with the disadvantages of each braking method and based on the best possible choice, a selection is made for the VAWT design in question. The possibilities of further development based on each major work are highlighted and details given on the scope of research by listing the specific research objectives at the end of this chapter.

Chapter Three

Chapter Three begins by introducing the problem of quantifying magnetic braking and reviewing major literature contributions on modelling magnetic brakes. After discussing the suitability of a particular low-speed model for a mathematical controller development

approach, a prototype test bench is introduced and the components explained that make up the system. Then the model chosen is used to be verified against experimental data taken from the test setup introduced previously. Next, a software-based model is derived from the experiment and verified again with a test. Then the controller development using a) the software-based model and b) the test setup to verify the procedure is documented, along with the development of a rapid prototyping program that can test different controllers or refine a controller obtained from the model. The chapter concludes with a summary and how the development of Chapter Three relates to the actual wind turbine setup and helps understanding the key issues involved in the development regime encountered.

Chapter Four

Chapter Four provides an introduction to the aforementioned VAWT setup and documents how experimental data was obtained for determining the WT power characteristics. Additionally, different WT modelling possibilities are discussed and at the end of the evaluation, a novel numerical model is shown that was derived from the experimental data. Furthermore, possibilities of future development are highlighted. The chapter finishes with a complete WT model using the analytical model developed beforehand. The no-load speed of different step inputs are analysed and compared to the experimental WT torque characteristics.

Chapter Five

This chapter begins with a calculation of the electromagnetic brake rating used for the wind turbine. Another calculation follows concerning the control requirements. These are derived from the turbine dynamics at the highest expected wind speed in order to give an estimate of the shortest transition time possible. After the requirement analysis, a scaled brake model is given that is used in two control mode simulations: a) braking to a reference (maximum) speed and b) braking to track the maximum power point. Finally, a supervisory control template is given for future development. The chapter concludes with a performance evaluation of the two control modes and a summary.

Chapter Six

Chapter Six reviews the objectives given Chapter Two and highlights the attainments of each research aim as well as the limitations encountered. Furthermore, the original contribution to knowledge based on the literature review in Chapter Two is provided. Concluding remarks and recommendations for future work then finish the thesis.

2. Literature review

The following chapter gives a detailed review of relevant literature in the field of speed control for VAWT and highlights the investigations carried out in this particular wind engineering project. As mentioned in the introduction, the key to wind turbine control is a suitable braking mechanism; this chapter is therefore dedicated to evaluating different braking methods, choosing the most suitable braking regime which can cover each of the modes described in the introduction and at the same time identifying limitations in literature which have laid the foundation for this research project.

As mentioned in the introduction, a change of the aerodynamics of a VAWT such as the VAWT this work is dedicated to, is often more involved due to the design. The VAWT prototype in question, for example, has 12 rotor blades in total and therefore it would add considerable more expense and development work to provide a pitch mechanism for a couple or all of the blades. Also, due to the lower expected annual wind speeds in an urban environment, a pitch mechanism has not been allotted in this project. Thus, the remaining two options for turbine speed control are considered only, i. e. electromagnetic/ electric braking using generator loads and mechanical braking. However, in the wake of a changing climate, more extreme weather patterns are to be expected, also in urban environments. Thereby, furling control of a VAWT may well have to be considered in future developments to be able to operate the turbines safely.

The remainder of this chapter is organized as followed: first, two different works on electrodynamic braking are reviewed and summarized briefly and the limitations of the latter are highlighted. The chapter then goes on to look at mechanical braking using friction brakes which is examined in two works that make use of hydraulic actuation and control. Again, the limitations of this approach are discussed which then leads to the third topic of braking the turbine mechanically using electromagnetism. The advantages of electromagnetic braking are pointed out and existing research as well as a patent are reviewed to be able to judge the knowledge gaps presented in this chapter. At the end of this chapter, a list of research goals is given which serves as a basis for the chapter structure continued.

Electrodynamic braking includes all regimes that cover slowing a turbine shaft down by varying the electric load attached to the generator. This can be achieved with the following examples setups:

1. The AC to AC inverters explained in Chapter One can be utilized, together with a dedicated controller, to vary the apparent power when connected to the grid [28];

2. A variable dissipative load/ a load bank or a battery for storage with control circuitry or a dedicated controller, such as in grid failure situations [29];
3. By short-circuiting the generator stator windings [30];

The first item in the list depends on the demand for electricity when considering an island mode of operation. In emergency situations, when the wind exceeds the rated wind speed, or also when a grid fault occurs, excess energy has to be bypassed and dissipated or stored in order not to damage the infrastructure. In this case, a solution like in the second listing would have to be provided. Yankov et al suggest a circuit using high power thyristors rated according to the turbine output that detect overvoltages when a grid fault occurs. The advantage of this method would be that the braking circuit can be installed on the ground and the reliability of the brake due to the contactless operation. However, the need for a full rating of the thyristors and dissipating resistors may call for a costly solution. Furthermore, the authors indicate that the proposed circuit is applicable with benefits in medium to high WT power systems. The third possibility, uses short-circuiting of the generator stator windings utilizing a permanent magnet generator of a small wind turbine installation. McMahon et al emphasize the importance of a high generator rating, making the generator capable of stopping the wind turbine as well as tolerating high thermal loads.

The second topic of this chapter is concerned with mechanical braking using friction brakes, and hydraulic actuation on brake callipers [31] [32]. In order to save cost and size, a friction brake is usually placed on the high speed shaft if a gear train is used. A friction brake is advantageous in terms of its ability to aid any other braking methods applied along with the benefit of being able to function as a parking brake. However, the obvious disadvantage of this type of braking is the need for maintenance due to wear, such as disk replacement, braking pads replacement and maintenance/ setup of the pipe system to eliminate enclosed air in the braking fluid. Also, the mechanical setup is more intricate, imposing the need for a pipe system, springs for the brake pads as well as a pump for actuation. However, irregularities in the mechanical system from wear and non-linearities imposed by friction or local heating may be compensated using disturbance control algorithms as suggested in both works.

The last topic examined covers electromagnetic braking using eddy current brakes. Magnetic brakes are particularly useful in high-speed applications such as in high speed trains or roller-coasters since the braking power depends on the speed of the vehicle. However, the low speed region can also be exploited by using high frequency operation of the magnet, provided that a laminated core material has been utilized so that eddy current losses do not counteract the gain in retarding torque. Like with the use of friction brakes, placing an eddy current brake on the high speed shaft of a geared WT also further increases

the braking power and reduces the size of the installation, in this case twofold due to the higher speeds leading to a higher braking torque in addition to the added benefit from the transmission.

Deploying a magnetic brake delivers many advantages compared to a friction brake; the most important advantage is that the magnetic brake requires no maintenance. The braking force is merely developed by induction which leads to a retarding motion due to two opposing magnetic fields when the brake is switched on. The braking energy is completely dissipated in the form of heat generated by the decaying eddy currents. Compared to the intricate installation of a friction brake using hydraulic actuation to achieve the torques needed, a magnetic brake is much simpler in that only a disk or multiple disks and one or more electromagnet(-s) are needed for creating a braking torque. Additionally, deploying an eddy current brake means that the installation is not sensitive to humidity and contamination, such as with oil. However, the inherent dependency on motion does not make the eddy current brake suitable for parking a wind turbine which, for example, is required for any maintenance work on the wind turbine.

To the knowledge of the author, only three works exist about investigations or inventions in the field of eddy current brakes for wind turbines, two of which are patented [33] [34] [35]. Jee et al suggest a magnetic brake with an adjustable air gap using a housing similar in design to a drum brake. The permanent magnets used are placed on the shaft, i. e. the aluminium housing is utilized for developing the eddy currents. If braking is needed, the permanent magnets are moved close to the drum and therefore exert a braking force on the shaft. The authors suggest that the magnetic brake be deployed as an auxiliary brake system to prevent excessive power output at high wind speeds [33]. The second work, a patent by Mongeau, describes a generator housing a two-stage eddy current brake system which is integrated into the cooling system using fluid flow, a heat exchanger and a blower. The methods associated with this type of generator for operating a wind turbine is patented as well [34]. Kloft/ Knestel, on the other hand, have patented the use of eddy current brakes and associated control algorithms for induction generators as well as for synchronous machines. Control of an induction generator using an eddy current brake is dedicated to slip control so that the generator is operated, yielding a high torque but does not reach the critical maximum torque characteristic of an induction machine. The authors have also patented speed control for synchronization of the generated voltage with the grid frequency using a synchronous generator or generally, speed control using a sensor connected to the rotor shaft and using that sensor for any speed control application [35].

The works discussed in this chapter have led to the decision to deploy an eddy current brake in the wind engineering project, partly for the advantageous reasons already

mentioned. Furthermore, the first topic dealing with generator load control led to the conclusion that the generator rating limits the braking torque which cannot be accepted in emergency situations. Particularly at high wind speeds, the generator may not be able to brake the turbine which strongly suggests to make use of an eddy current brake in this case. Additionally, it has been highlighted already that hydraulic actuation of friction brakes adds complexity as well as the need for maintenance; therefore a friction brake would only be deemed useful in a SSWT as a parking brake where electric actuation would likely suffice for parking the turbine. Since the braking torque of an eddy current brake can be customized according to the wind turbine rating, and also further improved by high frequency operation, as mentioned before, the eddy current brake is considered the best option for the requirements listed at the beginning of this chapter.

In the introduction, it has been mentioned that the focus of this work was repeatability and being able to customize a control design towards a specific SSWT design. To the authors knowledge, no work exists yet which simulates eddy current brakes in WT and exploits rapid prototyping technology for the development. It was therefore decided to build a software-based model of the entire plant, to develop a novel controller for different applications depending on the operating mode of the turbine and to verify the controller in a hardware-in-the-loop (HIL) experiment. Due to limited access to the turbine, it was decided to build a novel test bench setup first for collecting experimental data as well as for verifying the development process. The following chapters are dedicated to the core topic of this research project, i. e. software-based development of physical plant models for creating control systems with variable hardware parameters using a suitable simulation software, Matlab/Simulink, and state-of-the-art HIL technology. More specific, the research objectives of this project have been crystallized to the following:

1. Development of an innovative braking prototype/ controller development using Matlab/Simulink and HIL
 - (a) Development of a novel sensory system/ power stage
 - (b) Development of a brake model for the setup
 - (c) Controller development
2. Development of a novel numerical wind turbine model for a laboratory setup
3. Development of a novel small scale wind turbine controller
 - (a) Requirement analysis
 - (b) Development of a control scheme for braking to a reference speed

(c) Development of a simulation for MPPT control

(d) Performance evaluation

These objectives form the basis of the remainder of this report. The last concluding chapter will include a discussion on how each item was approached and whether the results were as expected.

3. Development of a novel brake controller

In this chapter, the principle of magnetic braking is explained first. A more detailed discussion on available models follows, which in turn compares the results and the usability of the models for a more experimental approach.

3.1 Magnetic braking

Magnetic braking is based on electromagnetic induction. The mathematics behind the phenomenon is governed by Faraday's law and Maxwell's second equation. The integral form of Faraday's law is given by

$$\oint \mathbf{E} \cdot d\mathbf{s} = -\frac{d}{dt} \iint \mathbf{B} \cdot \mathbf{n} dA \quad (3.1)$$

All vectors and matrices used in this text are given in bold letters.

In practice, equation 3.1 would mean that a conducting wire placed in the vicinity of a changing magnetic field would carry a current if a closed loop is formed that replaces the imaginary boundary path. The same principle, but geometrically much more complex than in a conductor, can be observed when a magnet is falling through a thin metal tube; in this case, a two dimensional geometry has to be considered since not only a single thin wire is exposed to a change in flux but the entire part of the tube in the vicinity of the magnet. Also, the three dimensional field of a cylindrically or spherical shaped magnet is complicated and non-uniform.

Equation 3.1 also shows that a change in magnetic flux, which is the area integral of the right hand side of the equation, can be generated by changing the enclosed area while leaving the magnetic field static. This principle can be easily observed in a simple generator as the effective flux changes sinusoidally with the rotation of the conducting loop(-s). Eddy current brakes work similarly; however, the unconstrained geometry of the exposed disk part adds considerably more complexity to the problem and hence, this process is proving difficult to describe quantitatively. Figure 3.1 shows a 2D example of eddy currents in a conducting metal sheet. The shadowed region, i.e. the B-field is indicated by the square projection onto the sheet where the B-field points into the page. The diagram also shows the opposing field (in green in the figure) induced by the eddy currents where the induced force is directed from the enforcement of the original field towards the weakening net force.

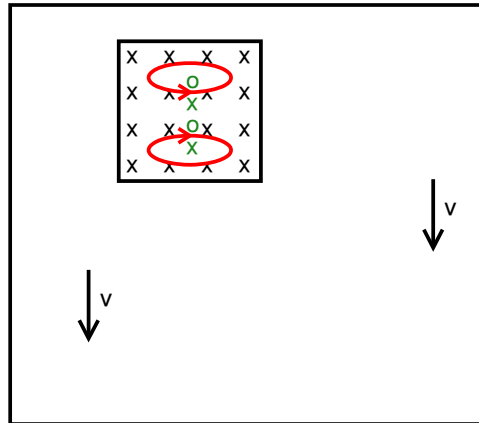


Figure 3.1: Eddy currents in a thin metal sheet

To describe the process somewhat qualitatively, a conducting square loop can be imagined that enters a magnetic field perpendicularly to the field lines with a certain speed. In this example, the area of the field is larger than the area of the loop. When entering the field, the loop experiences an increase in magnetic flux as the area increases. The opposite happens when the loop exits the field. While moving through the magnetic field completely exposed, the area does not change and therefore no voltage can be induced. Plotting the induced field against the travelled distance x would result in steps from $-Bav$ to 0 to Bav , where the speed v is the derivative of x in terms of t and a the length perpendicularly to v [36]. Figure 3.2 below shows the geometry of the example.

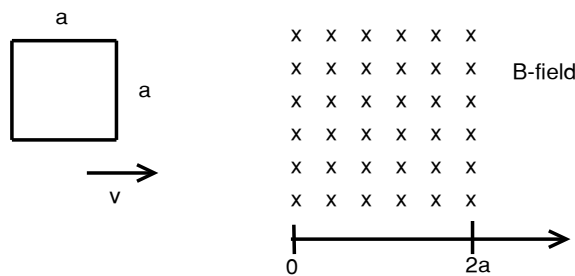


Figure 3.2: Stepwise eddy currents

It is conceivable that having an unconstrained geometry where the resistance of the disk brake is unknown makes it difficult to predict where the eddy currents travel and how long the decay lasts. Another modelling difficulty concerns the spreading out of the magnetic field across the gap and outside the iron core cross section. The increased geometric

complexity of the field outside the iron core adds to the problem, as well as the non-linear behaviour of the iron magnetization.

However, literature and experiments suggest that in the low speed region, the braking torque is proportional to both the speed and the square of the applied field. These findings were also confirmed for the experimental model of the brake, as will be shown later.

To illustrate a simplified quantitative measure of the generated force on a conductor cutting magnetic field lines, the following paragraph shows how the force on a straight conductor can be directly calculated from a generated current, the magnetic field and the geometry of the conductor.

The force on a charged particle q moving in a magnetic field is given by

$$\mathbf{F} = q \cdot \mathbf{v} \times \mathbf{B} \quad (3.2)$$

If this equation is modified to be valid for a differential of the vector F , it becomes

$$d\mathbf{F} = dq \cdot (\mathbf{v} \times \mathbf{B}) = I \cdot dt \cdot \left(\frac{d\mathbf{L}}{dt} \times \mathbf{B} \right) \quad (3.3)$$

The above equation can be used to form an integral that depends on the path which the charge travels, since

$$d\mathbf{F} = I \cdot (d\mathbf{L} \times \mathbf{B}) \quad (3.4)$$

If a conductor is straight and exposed to a uniform magnetic field, equation 3.3 becomes

$$F = I \cdot l \cdot B \cdot \sin \theta \quad (3.5)$$

This magnetic force actually acts on the electrons inside the conductor but if only a thin wire is placed in a magnetic field, the electrons are moved towards the surface of the conductor (in the case of the current flowing perpendicularly to the magnetic field) and therefore cause the conductor to move.

3.2 Literature review on magnetic brake models

Several authors have attempted to solve the problem of magnetic braking analytically [37] [38] [39]. Davis and Reitz completed an analysis carried out by Sommerfeld which is based on his image technique. The image theory is a method for simplifying the field solution for a radiating source that concerns non-free space. It can be applied if the problem can be divided into free space and non-free space, such as a non-magnetic conductor [40]. In the process of solving a boundary-value problem derived for the eddy current decay in a perfectly conducting half-plane (semi-infinite super-conducting sheet), Sommerfeld found a

Green's function for a point charge in the vicinity of the half-plane. He intended to extend his analysis to an infinite, perfectly conducting strip which would have involved a coordinate transformation of the original function but he never finished his work. Davis and Reitz carried out the same analysis for a magnetic monopole in the vicinity of a perfectly conducting half-plane and, after a coordinate transformation, they found the geometry lead to a conducting disk rather than to an infinitely long strip, as originally proposed by Sommerfeld. Finding the forces on the magnetic monopole involves deriving a stream function $\Phi(x,y,t)$ for the current in the sheet and relating this function to the magnetic potential. The problem is solved by treating the current decay as a "trail of receding images" of the field. Once an expression has been found for the magnetic potential due to the eddy currents, that equation can be differentiated to obtain the magnetic field components from the scalar magnetic field and thus the forces on the monopole. The magnet experiences a lift force, due to the eddy currents expelling the net field and a drag force that stems from the Joule losses in the sheet which the magnet has to provide. The authors relate this problem (assuming ideal conductivity) to the high speed case where the magnet is moving away from the trail of images quickly enough that the two cases are comparable.

Determining how the stream function or current circulation function $\Phi(x,y,t)$ decays becomes more complex when considering finite conductivity. Davis and Reitz noticed they could not provide a receding-image solution and, instead of solving the problem numerically which would have produced an exact solution, they provide two approximations which they found to be in accordance. One of those approximations has been utilized by Smythe [39]. If the initial conditions are found to be correct, a closed-form solution is obtained [37]. His result of the drag force of an electromagnet with a round core is

$$T = \frac{\omega \gamma R^2 \Phi^2 D}{(R + \beta^2 \gamma^2 \omega^2)^2} \quad (3.6)$$

where D and β are complex parameters that can be calculated from the geometry of the setup, R is the reluctance, γ the conductance and Φ the magnetic flux.

Schieber solved the eddy current problem analytically as well and utilized the same geometry as Smythe to be able to compare the results [38]. He found the models to be in reasonable accordance and verified the theoretical results by experiments. Both models proved valid for a low speed region up to a critical speed; for higher speeds, the added magnetic field from the eddy currents could no longer be neglected.

A lumped circuit approach has also been suggested by H. D. Wiederick et al and L. Cadwell [41] [42]. In this method, the eddy currents are treated as currents flowing through a confined conductor which is considered to be a wire with a rectangular cross section and the disk resistance is parametrized as an unknown variable. In the work of Wiederick et al, the voltage creating the eddy currents is treated like a battery with an internal resistance, where the generated voltage equals the induced voltage less the eddy current times the internal resistance. The eddy currents in turn equal the total voltage divided by an unknown external resistance. The induced voltage can be found using Faraday's equation. The left hand of equation 5.8 is the circulating electric field integrated over the closed circular path. It is the induced voltage. The right hand side describes the rate of change of the magnetic flux. If the magnetic field is perpendicular to the area, the projection of \mathbf{B} onto the area equals the magnitude of B :

$$\mathbf{B} \cdot \mathbf{n} = B \quad (3.7)$$

Furthermore, if the magnetic field is uniform across the area and the effects of non-uniformity outside the iron core are neglected, then no integral has to be formed.

This simplifies Faraday's equation to

$$V_{ind} = \frac{-d\Phi}{dt} = -|\mathbf{B}| \frac{d}{dt} \iint dA = -B \cdot \frac{dA}{dt} \quad (3.8)$$

since the magnetic field is uniform and perpendicular across the area. The area increases with time, one side is fixed whereas the other side increases along a circular path. The motion is described by the angle times a radius to the middle path, the centre of the magnet core:

$$V_{ind} = -B \cdot r_F \cdot w \cdot \frac{d\phi}{dt} \quad (3.9)$$

with ϕ being the angle of rotation, r_F the centre of the middle path and w the width of the core. The increase in angle with time is given by the angular velocity and therefore

$$V_{ind} = v_{tan} B_0 w \quad (3.10)$$

As mentioned before, Wiederick et al suggested that the total voltage be equal to the induced voltage less the internal resistance of the shadow region cube multiplied by the eddy current:

$$V_{tot} = RI = V_{ind} - rI \quad (3.11)$$

Furthermore, the authors use the assumption that the currents travel through an external resistance R and relate the internal resistance to the geometry, comparable to the specific resistance of a square conductor:

$$RI = v_{tan} B_0 w - \frac{w}{\sigma l \delta} I \quad (3.12)$$

The width in this case is actually the length that the eddy currents travel through and the length l times δ is the cross section of the conductor. σ and δ are the conductance and the air gap width, respectively. Solving this equation for the eddy current introduces a parameter 'a'

$$a = \left(1 + \frac{R}{r}\right)^{-1} \quad (3.13)$$

so the eddy currents are

$$I = v B_0 \sigma l \delta a \quad (3.14)$$

The braking force is found by converting the above equation into a spatial equation by first dividing by an infinitesimal volume piece dV and integrating over the volume in question. Equation 3.14 then becomes

$$F = \iiint (J \times B_0) dV \quad (3.15)$$

and the solution is

$$F = \mathbf{j} (a \sigma l \delta w B_0^2 v) \quad (3.16)$$

with the unit vector \mathbf{j} pointing towards the tangential direction, as expected. The above equation also reveals the force to be proportional to the speed as well as the square of the magnetic field. As will be seen, this relationship was confirmed in the experimental modelling section found later in this chapter.

Another parametric solution has been suggested by J. H. Wouterse [43]. He assumed a super-conducting ring below the iron core that encloses the exposed area of the disk and creates a short circuit, inhibiting currents to spread out the shadow region of the core. He could derive the total power dissipation from this assumption which is given by

$$P_{diss} = \frac{1}{4} \frac{\pi}{\rho} D^2 d B_0^2 v^2 \quad (3.17)$$

and divide both sides by the velocity 'v' to find the dragging force. The parameters in equation 3.17 are the diameter of the core D, the thickness of the disk d and the specific resistance, respectively. The drag force is given by

$$F_{br} = \frac{1}{4} \frac{\pi}{\rho} D^2 d B_0^2 v \quad (3.18)$$

He then compares his idealized model to the analytical result found by Schieber and adds a parameter 'C' to the above equation which is given by the geometry:

$$C = \frac{1}{2} \left[1 - \frac{1}{4} \frac{1}{\left(1 + \frac{R}{A}\right)^2 \left(A - \frac{R}{D}\right)^2} \right] \quad (3.19)$$

A last modelling approach was examined by Scherf which utilizes Matlab/Simulink to describe the magnetic braking process [44]. The author assumes the same proportionality for the induced voltage as given by equation 3.9 and uses that voltage as the source for the eddy currents, neglecting an internal resistance. Additionally, he treats the shadowed region as a single conducting loop and postulates that the eddy currents move within this region. When the loop enters the B-field, the induced voltage is negative whereas when it exits the field, the voltage becomes positive. The induced eddy currents are assumed to travel the width of the iron core, which is square in this case, and add up to a net force like in a straight conductor, given by equation 3.1. Moreover, the impedance encountered by the eddy currents includes the inductance of the hypothetical loop. The resulting force is obtained by multiplying the eddy currents by the B-field and the width, as mentioned before. The author uses this simulation to test several speeds. He wrote a Matlab script that runs a for-loop through a speed range and plots the torque results against the speeds used. In each loop, the simulation is invoked and runs as long as it takes for the loop to enter and completely exit the field. The resulting force is then obtained in the script by integrating the simulated force over that time. The model given by Scherf was also tested against experimental results but it was not considered satisfactory enough for the low speed region as torque increases too rapidly with a speed increase. Furthermore, it could not serve as a modelling starting point since the speed is assumed to be fixed. In a closed-loop simulation, iteration has to be considered, i.e. the initial speed is decreasing while the braking force is applied, hence, the force itself is decreasing. In theory, this also means that a magnetic brake can never completely stop a system; however, bearing friction and air resistance usually help bring a system to a halt.

3.3 A modelling approach from a control perspective

Simeu and Georges have developed an approximate brake model for the low speed region as well as a compensator design based on that model [45]. They used the feedback linearisation method, or more precisely, input-output feedback linearisation, as opposed to utilizing an approximated linear model, reasoning that large deviations about the operating point chosen cannot be accepted. Simeu and Georges based their brake model using equation 4.2 and the braking parameter C established by Wouterse:

$$F_{br} = \frac{\pi}{4 \cdot \rho} \cdot D^2 \cdot d \cdot B^2 \cdot C \cdot v \quad (3.20)$$

Assuming a non-linear B/H curve, the authors give an approximation for B with two equations for a positive as well as a negative current/H-field. Substituting B in equation 3.20 yields the following dependency between the force F_{br} , the exciting current i_e and the speed:

$$F_{br} = (\alpha_0 + \alpha_1 \cdot i_e + \alpha_2 \cdot i_e^2) v \quad (3.21)$$

Equation shows parameter constants $\alpha_0 - \alpha_2$ and the direct dependency of the force on the square of the exciting current and the speed. This brake model is then inserted into a state space equation derived by Newton's second law. The state-space representation then takes the form

$$\begin{aligned} \dot{\mathbf{x}} &= \mathbf{F}(\theta, u) \cdot \mathbf{x} \\ y &= \mathbf{H} \cdot \mathbf{x} \end{aligned} \quad (3.22)$$

where u is the excitation current, θ a vector with the parameter constants $\alpha_0 - \alpha_2$ divided by the system inertia and \mathbf{H} is the row vector $\mathbf{H} = [1 \ 0]$. The states of the vector \mathbf{x} are the system speed and a state proportional to the dragging torque; the latter variable should be nearly constant or slow in response. Two observer-based control techniques are suggested in this work for controlling the speed of the brake and estimating the torque to be compensated. The first proposal uses a dynamic and the second one a static feedback law in u . The model shown in 3.22 is linear in state and quadratic in the control input. However, comparing the equation to the standard state-space form

$$\begin{aligned} \dot{\mathbf{x}} &= \mathbf{A} \cdot \mathbf{x} + \mathbf{B} \cdot \mathbf{u} \\ y &= \mathbf{C} \cdot \mathbf{x} + \mathbf{D} \cdot \mathbf{u} \end{aligned} \quad (3.23)$$

it is also apparent that the matrix \mathbf{A} contains a function of the input u . This type of state-space equation requires advanced control techniques which were considered beyond the

scope of this work. Therefore, a more practical approach was utilized using Wouterse's model since the latter showed close resemblance to the experiments.

3.4 Prototype design suggestion

In this section, the braking prototype suggestion is introduced which is intended for creating an efficient and repeatable controller development regime. The following sections highlight the components that complete the system and their suitability for the VAWT setup judging from the experiments conducted. The brake model verification achieved in this chapter is also based on the test bench setup developed.

Figure 3.3 shows a CAD 3-D model of the eddy current brake test setup which consists of an excitation coil (in this case, two are shown in brown) with a C-shaped soft magnetic steel core (material: S235JR, dark gray) and an aluminium disk mounted on a shaft. A DC motor drives the eddy current brake disk through a gear box enclosed with a gear ratio of 30:1 (see top of figure) which was intended to replace the slow speed vertical axis wind turbine in the prototype setup [46]. The scale of the figure is approximately 1:5. The following sections document the hardware setup as well as the rapid prototyping system and describes the selection and development of a novel sensor setup and a two-fold power stage circuitry.

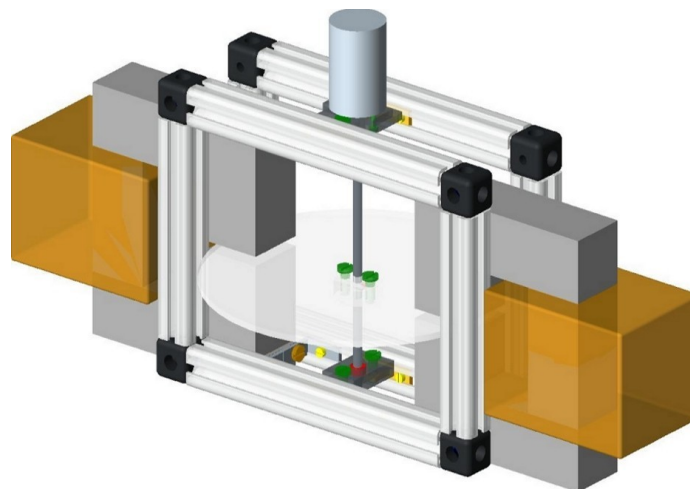


Figure 3.3: Magnetic brake assembly [46]

The eddy current brake model and the controller developed are verified using a procedure called hardware-in-the-loop (HIL). Running HIL tests with a controller in the actual system validates or refines a developed control system. Tests can be automated by running Matlab scripts invoking a HIL simulation with different parameters for evaluation.

The HIL development board, a Q2-USB from Quanser (see figure below), has 8 bidirectional digital pins, four of which are needed for the motor driving circuit. Furthermore, an encoder channel reads the sensor signal described in the following section. Additional software is needed for developing HIL applications, the development suite Quarc [58] from Quanser which is commercially available. The software fully integrates with the Matlab/ Simulink environment which is also used for the simulations and requires the Microsoft Software Development Kit (SDK), and an MS C++ compiler. For this project, Windows 7/ 64 bit OS was used with MS Visual C++ Express 2010, MS SDK 7.1 and Quarc 2.2.

The encoder channels of the Q2-USB board have five connectors; two are used to provide the supply voltage for the sensor, two channels are used for angular counts with a phase shift of 90° and an optional pin can be connected to a direction bit. The counter register takes 16 bit counts and if the counter reaches the lower limit of -32768 in a simulation, it is reset to the positive end of +32766. Only 4x quadrature encoding is supported on the I/O card which refers to the mode of detection of the edges. In 4x mode, all edges from both channels are counted which yields a full 4096 bit resolution with the encoder used.

In the following sections, the I/O card Q2-USB and the development suite are described in detail. The Quarc software environment supplies custom Simulink block libraries necessary for generating target code for the board. The software also integrates with the Matlab extension Simulink Coder [47] and its external mode which is needed for HIL experiments.

3.4.1 Hardware description

The Q2-USB is designed for analogue and digital data acquisition and data output [48]. A dedicated CPU on the target board accommodates the digital signal processing unit of the inputs and outputs. All analogue interfaces are accessed using shielded audio cables, i. e. cables with cinch and 5-pin DIN connectors. In every simulation, the sampling rate of the analogue and encoder channels equals the simulation step size. The bidirectional communication between host and target is established through a USB 2.0 connection which can achieve a throughput of maximum 60 MB/s. The board has 8 digital I/O pins, two of which can be alternatively configured as PWM outputs. The PWM frequency can be set in the configuration block and is based on either the simulation step size or a separate PWM time base; however, it is then fixed to the frequency chosen. The duty cycle is variable and can be applied as an input to a PWM Simulink block.

3.4.2 Software environment

The software targets that can be specified in the Simulink Coder configuration setup include the Quarc Windows Target which is a soft real-time system, i. e. a system that meets soft real time requirement constraints [49].

Amongst other blocks, Quarc provides input and output Simulink library blocks. Any continuous transfer function contained in a model does not have to be converted to the z-domain when conducting HIL-experiments, however, the simulation step size has to be fixed. When a model is ready for compilation, the Simulink coder generates a real-time application if the Windows target is selected in the configuration pane settings. The binary is downloaded directly after the compilation. A daemon running on the target, the Quarc Target Manager, services the requests from the host. When the application is running on the target, it can respond to any requests to stream data on the host or to update model parameters online. The connection is established over the external mode interface [50].

3.4.3 Development of a novel sensor setup

The following discussion provides an overview of the sensors that can measure the angular speed. The interfacing with the main software component, Simulink, used for modelling and HIL development is considered as well.

Suitable sensors include

- tachometers
- magnetic sensors
- optical sensors

Tachometers are in essence small permanent magnet DC generators that are driven by a shaft of the system to be measured. The rotational speed is directly proportional to the generated voltage and the generator constant of the motor is the proportionality factor relating the two physical variables. The generator constant needs to be calculated using the no-load speed from the motor datasheet:

$$C_g = \frac{V_{in}}{\omega_{no-load}} \quad (3.24)$$

Tachometers are reliable speed sensing elements but they are mechanically more intricate to install than compared to other solutions. However, it would be advantageous to use the generated analogue voltage which simplifies the interfacing to the digital system. Using an analogue voltage, the input to a microcontroller is automatically sampled and held within the intervals that are selected for the step size in the simulation parameters dialogue.

Magnetic sensors come in a variety of forms. One of their main advantages is that they can be reliably deployed in cases where optical sensors are prone to malfunction due to a contaminated environment. For rotating ferromagnetic bodies, variable reluctance sensors and hall effect sensors can be used [51]. In both cases, the sensors generate a magnetic

field and detect a change of the latter. A change, however, requires a varying field due to motion in the near vicinity which means that the sensors are typically used for gears or bodies which are slotted on their circumference. Hall-effect sensors can also be used in conjunction with magnets attached to the rotating body. However, the magnets use up space between the sensor and the magnet and the resolution is limited to the number of magnets being used. Furthermore, each cycle requires two magnets.. This setup is therefore unsuitable for measuring the speed of rotating shafts in the lower ranges (<100 RPM).

In this context, a minimum speed limit may narrow down the selection of sensors as well. Variable reluctance sensors, for example, require a certain minimum speed to be able to detect changes in the output which varies proportionally with the actual speed. Other measurement errors may result from a "cogging" type motion due to a torque that might be generated by the magnetic field interference [52].

For materials such as aluminium, an equivalent concept exists – the eddy current killed oscillator (ECKO) principle. By means of eddy current losses in the rotating conductive non-ferromagnetic material, induced oscillations are literally "killed" and a triggered detector produces a signal. However, these sensors are usually designed for industrial applications and were therefore considered out of the price range for this project.

The third major category of sensors, optical transducers, need a light emitting diode and a receiving photo transistor. Usually both components come in one IC package. There are two methods in use of conveying a light beam, either by reflection or directly. Using the reflection method requires the emitting diode to be at an angle towards the receiver whereas in the direct configuration the components oppose each other. The direct method utilizes light interruption to generate an alternating signal. In the case of a rotational measurement setup, this method requires an encoder disk with alternating opaque and transparent segments. The reflection version of the transducer can be used in a similar setup using an encoder ring which can be applied to the bottom of the rotating disk, as for example. The encoder is divided into periodic black and white segments that absorb and reflect the light beam, respectively. Both methods may be sensitive to the surrounding light conditions, depending on the type of light emitted and the distance between the transducer and the encoder. The reflection method allows a simple configuration that can be easily added into a finished test bench. This variant was experimentally tested but then dropped due to its limited resolution. It has been verified that the sensor's recovery time was too slow when a critical number of fields were used on the applied encoder printout. Furthermore, when considering the interfacing with Simulink, it was found that no software building blocks were found that count the angular impulses within a fixed time interval which has to correspond to the step size of the configuration parameters. The step size has

to be equal to the digitization of the sensor. Due to the lack of a ready selection of software building blocks of the latter sensor, a complete US Digital E5 encoder unit with a resolution of 4096 steps per revolution has been chosen instead [53].

Figure 3.4 shows the disassembled view of all the components, i. e. the encoder disk, the sensor and the housing. The hardware encoder interface takes two channels A and B and provides the supply voltage. The sensor could be installed on the bottom of the shaft where the lower bearing is situated. Mounting the encoder was comparable to the reflective photo interrupter and the requirement for a good resolution due to the slow rotational speeds could be met.

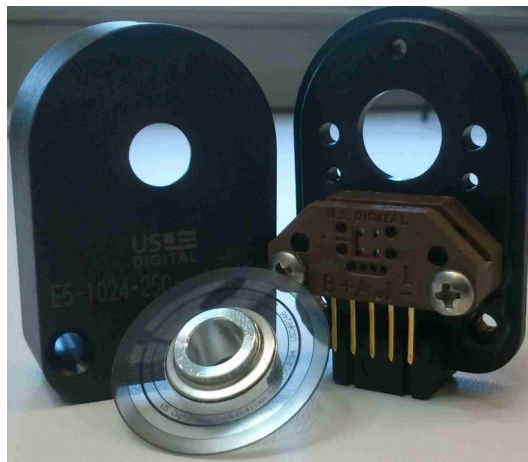


Figure 3.4: US Digital Encoder

The encoder pulse count can be readily obtained from a Quarc encoder block. A simulation using a scope shows that the pulses are counted from zero initially and that the encoder is reset to the negative end once the upper limit of a 16 bit register is reached. If the counts could continue indefinitely, the actual speed would simply be the slope, or expressed in discrete terms, the number of counts in a given interval. The resets, however, require some form of signal processing to filter out sharp peaks that result from the counter reset. Also, the signal was found to contain high and low frequency noise components, with the latter being a result of the alignment between the rotating encoder disk and the sensor. If the encoder disk is not rotating centrally, the tangential speed is changing sinusoidally and hence a low frequency adds to the signal. The high frequency components are filtered using a first order Laplace transform block. The filter was calculated using the Laplace transform for a first order filter using a cut-off frequency of $\omega_c=50 \text{ s}^{-1}$:

$$G(s) = \frac{\omega_c}{s + \omega_c} = \frac{50}{s + 50} = \frac{1}{0.02s + 1} \quad (3.25)$$

The encoder counts are converted to the equivalent angular speed by means of a custom Embedded Matlab function. A Simulink diagram is given in the figure below. It shows the blocks for reading and processing the encoder signal.

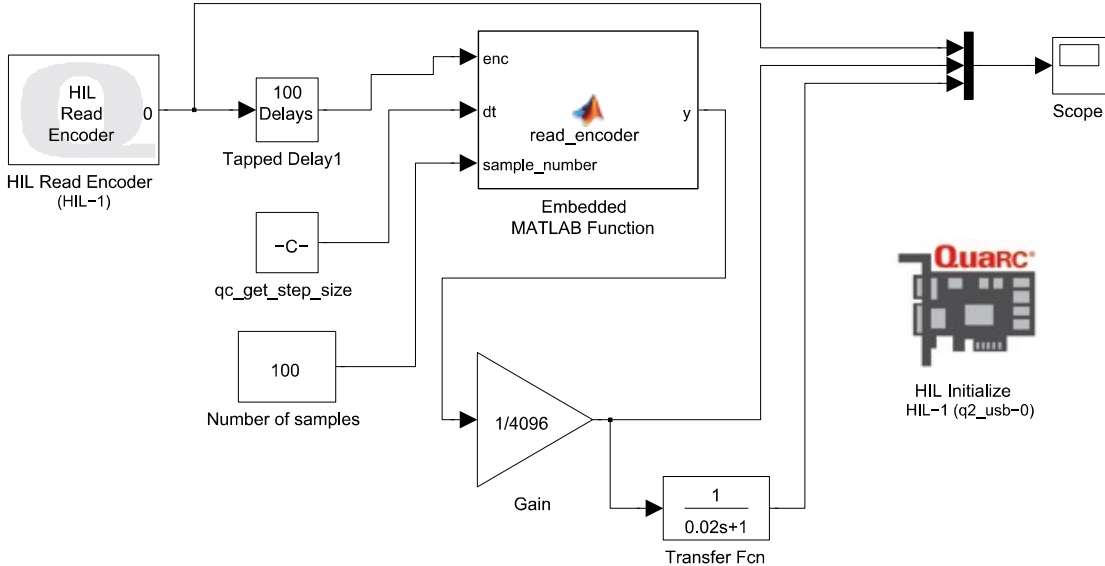


Figure 3.5: Encoder signal processing

The aforementioned encoder block from the Quanser Simulink library is used to read the encoder counts. The signal is then tapped to store a block-defined number of previous values including the current one which is written to a field of a structure. For each simulation iteration, a row of 100 values is stored in the field 'values' which is also a vector input to the Embedded Matlab function code denoted with 'enc'. Further inputs are the simulation step size 'qc_get_step_size' defined in the 'Configuration Parameters' pane, which is 2 ms, and the number of samples. The output of the function is divided by the resolution of the encoder and then further filtered with the first order Laplace transform calculated previously. The content of the averaging function is listed in the frame below. Apart from the three inputs mentioned before, two more variables are declared for local use in the function only. Defining the local array variable 'speed_array' as empty produced a compiler error as dynamic storage allocation induces significant overhead for any controller. The array has therefore been fixed to a size of a 100 elements. In each simulation iteration, a 'for' loop is executed, starting with the second element of the array to the number of samples given to the function. The second local variable is used for indexing the variable 'speed_array' while the loop is running. The for loops wraps around an if statement which tests whether the encoder reset is encountered. In the alternative branch, the difference between two adjacent encoder entries is written into the local array and the index is increased by one to point to the next position. After the for-loop, the angular speed

divided by the step size is calculated for each encoder difference and a Matlab function sums up the speeds stored in the array. The function returns the latter divided by the size of the array, which in turn is the output to the next Simulink block.

```
function y = read_encoder(enc,dt,sample_number)
speed_array = [100];
index = 1;
for n = 2:sample_number
    if abs(enc(n) - enc(n-1)) > 30000
        ;
    else
        speed_array(index) = enc(n) - enc(n-1);
        index = index + 1;
    end
end
sum = 0;
speeds = (speed_array / dt * 2 * pi)/4096;

sum = sum(speeds);

y = sum / size(speeds,2);
```

3.4.4 Development of a novel power stage setup

Microcontrollers are dedicated microprocessors that are designed to read a sensor, process the information and actuate on a process according to the signal input. However, due to the low power consumption of a microcontroller, large loads cannot be driven directly. Therefore, an external circuitry is needed which receives a driving signal from the microcontroller, either an analog or a digital signal. Generating an analog voltage requires the use of a digital-to-analogue converter (DAC) combined with signal conditioning and power stages to get the desired output specifications for a given load. One drawback of this method, however, is that the selection of a DAC depends on the load to be driven [54]. Utilizing a digital signal to drive a load has the advantage of simplified interfacing with power electronics circuitry.

For controlling the electromagnet of the test bench setup, a modulated pulse width (PWM) has been deployed. Varying the root mean square (RMS) value, i. e. controlling the digital equivalent of a given analogue voltage range can be accomplished by using a digital signal with a varying duty cycle and amplifying this signal. The general formula for calculating the RMS value is given by:

$$V_{RMS} = \sqrt{\frac{1}{T} * \int_0^T f(t)^2 dt} \quad (3.26)$$

For the specific application of a PWM with a fixed duty cycle, the formula above reduces to

$$V_{RMS} = V * \sqrt{\frac{\tau}{T}} = V * \sqrt{D} \quad (3.27)$$

with τ being the duration when the signal is logically high. The duration of the active length compared to the whole period length of the signal is defined as the duty ratio D or duty cycle [55].

However, driving an electromagnet with a PWM is tied to eddy current losses due to the soft iron core. In transformers, core lamination steel prevents eddy currents from developing but unfortunately, this requirement was neglected by the designer of the electromagnets due to the wrong assumption that a DAC would be used instead of a PWM. Therefore, a quantitative measure of the losses is given in this section to be able to compare model with experiment.

For controlling the electromagnet, a two stage power circuitry has been deployed using printed circuit boards (PCB) for this purpose. The first stage is controlled by the full bridge driver IC L298 which is directly connected to the PWM signal generated by the Q2-USB card. The data sheet indicates that the power rating suffices for the wattage of the electromagnet; however, it was found that the IC could not drive the load as the exciting voltage was drastically reduced when a connection was enabled. Therefore, a second driving stage was introduced utilizing a MOSFET circuit. The PCB were designed using Cadsoft Eagle [56].

With the L298 IC, two full bridge circuits can be driven simultaneously. Any developing heat is dissipated by a heat sink which should be mounted on the driver IC using thermal conductive paste. The signals needed for the full bridge driver are the PWM signal itself, a common ground signal, a reference voltage level signal from the Q2-USB board and a logic Enable-signal for one current flow direction in the circuit. For controlling the magnet, the directional signals have been chosen to be fixed; that is, one PWM input is high and the other one is directly connected to the common ground plane.

The L298 is shown as IC1 in the schematics of figure 3.6. For the input signals, a standard pin header with one row has been selected as indicated by CON_DATA*. Since the supply voltage and the motor outputs usually carry high currents, RIACON screw terminals were used which can be found as CON* in the schematics. According to the datasheet, the motor IC needs two 100 nF capacitors against faults from the TTL supply voltage and the power supply that should be placed close to ground. The capacitors can be found on the left hand side of the schematics. Furthermore, fast switching diodes D1-D8 (Schottky diodes) with a recovery time < 200 ns were added to the circuit as recommended in the datasheet. The

latter suggests that with this solution, the IC can drive up to three Amperes which is more than the maximum ratings of either electromagnet for the test bench and wind turbine, respectively [57]. Unfortunately, as it turned out in various experiments, driving the low resistive load with 1.25 A in one channel was enough to lower the output voltage of the driver circuit. With motors, this problem is usually avoided by utilizing additional circuitry to cut off current spikes. However, limiting the current was not desirable for a braking application, hence, an additional driving stage was added. The schematics and its operation are discussed after the following hardware layout description of the L298 PCB.

In the datasheet of the L298, the layout is mostly dictated by the Schottky diodes as they need to be placed in the immediate vicinity of the L298. The L298 also facilitates a current measuring unit on the chip for both channels and for completeness, high power shunts were included on the board. Furthermore, each direction of both high current outputs are visualized by using differently coloured LEDs. The power supply is also equipped with an LED.

The finished PCB layout can be viewed in the appendix. Two layers have been utilized in the PCB design as indicated by the different colours of the conductive paths. Parts directly added from the Eagle library included the pin headers, the capacitors, the LEDs as well as their protection resistors. The hardware package for the L298, a Multiwatt 15 housing, was manually added to the library using an open source package [58]. No appropriate libraries were found for the screw terminals; therefore, custom libraries were created from existing libraries that needed minor modifications. For clarity, a major part of the wire connections in the schematics have been omitted. However, signals which carry the same name are still connected. This method ensures that the signals will be connected in the board design mode, i. e. schematics and board design are consistent. The required trace width of the driving connections was calculated using an online calculator [59]. A bill of materials is included in the appendix which also lists the components needed for the second stage (Appendix I). The PCB was ordered from SEED studio/ Fusion PCB Service [60]. An image of the finished and assembled board is shown in the figure below the schematics.

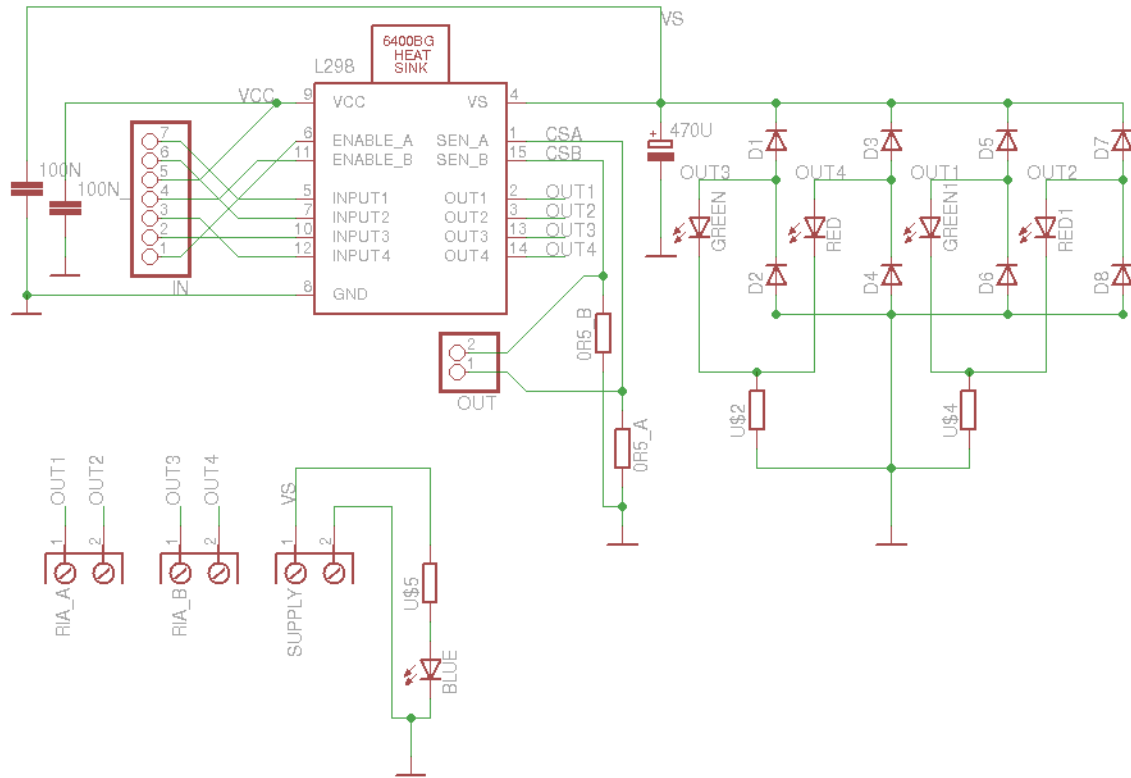


Figure 3.6: Schematics of L298 bridge driver

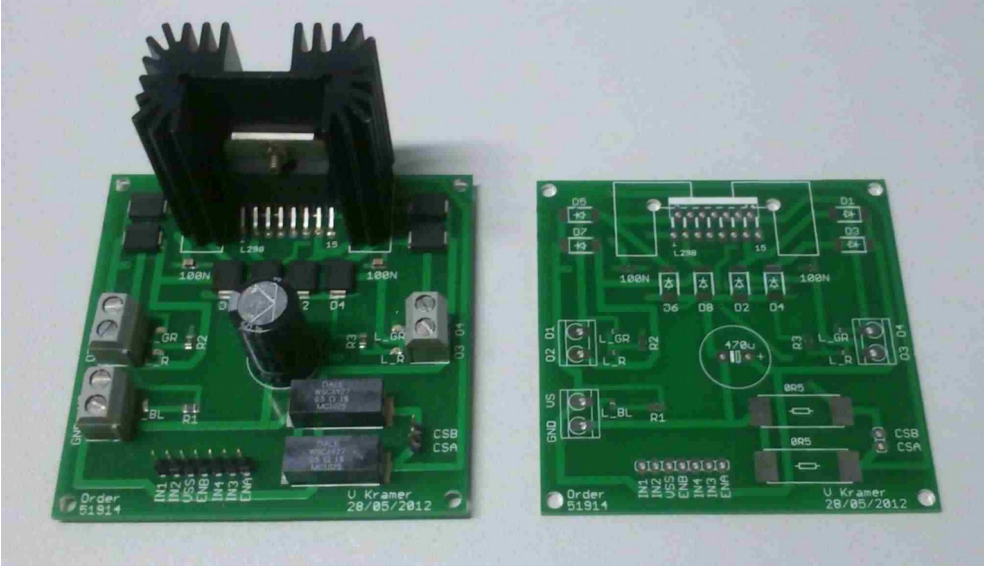


Figure 3.7: Assembled L298 PCB

The second driving stage was designed on a separate PCB. It contains a few components only, i. e. an N-channel MOSFET IPP80CN10NG for driving the load, again a fast recovery diode MBR2045CT to enable the induced voltages from the coil to be dissipated, three screw

terminals and a voltage divider that ensures that 10 V are exceeded at the gate. It is common for power MOSFETs to have a 10 V threshold to be fully switched on, also referred to as a 'gate overdrive' [61]. Furthermore, another resistor was added as minimum protection for the gate. At higher frequencies, the input capacitance may lead to heating problems if enough current accelerates the charging process. The recovery times of the on-/off-states are 18ns maximum and therefore the MOSFET is suitable for being driven with a frequency of up to about 50 MHz.

The voltage supply for the amplifying stage is 15V, and the maximum power consumption of the MOSFET during the on-stage is

$$W = I^2 \cdot R_{on} = \frac{V}{R_{coil}} \cdot R_{on} = \left(\frac{15V}{9.5\Omega}\right)^2 \cdot 0.078\Omega = 194 mW \quad (3.28)$$

which is well below the maximum rating of 31W. The Schottky diode can take up to 10 A which is also well above the currents that are applied in both the test bench setup and the wind turbine setup. In this two-stage configuration, the L298 circuit serves as a voltage amplifier only and the actual driving stage is given by the IPP80CN10NG MOSFET and the MBR2045CT Schottky diode. A circuit diagram of the second stage with the components mentioned before is given below.

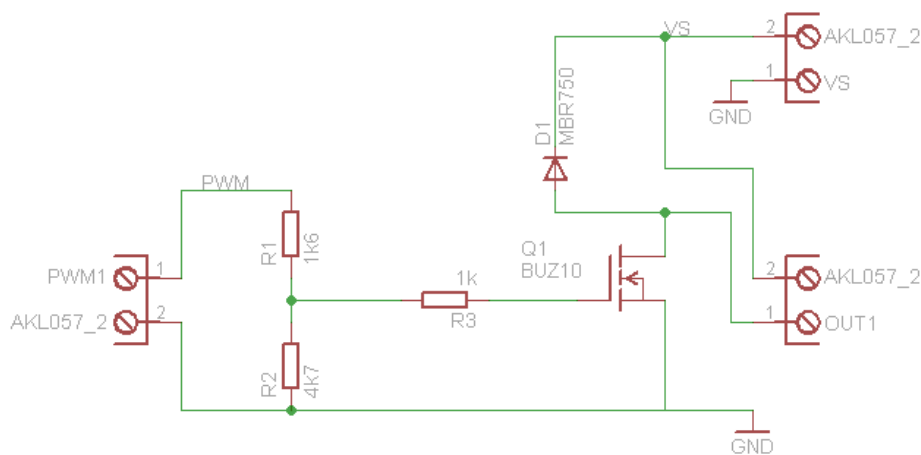


Figure 3.8: Second PWM driver stage

As already mentioned in the section about the use of PWM in general, a compensation function needed to be derived for the eddy current losses that can develop in the soft iron core. For this experiment, a Phywe Teslameter was used to measure the actual B-field in the air gap of the iron core. Since the field tends to spread out in the air gap, an average value was obtained from nine different samples across the core area. The results are shown

in figure below. All the current values on the x-axis were calculated from different duty ratios of $D = 0.1-1$. The green data in the figure shows the experimental results whereas the red data points are the theoretical values calculated from the formula

$$N \cdot I = \frac{B_g \cdot l_g}{\mu_0} \tag{3.29}$$

which is derived at a later point in this chapter.

The difference between the two data sets is given with the pink data set and fitted using a quadratic equation:

$$y = -109.6x^2 + 201x - 7.94 \tag{3.30}$$

The output of the polynomial is given in mT.

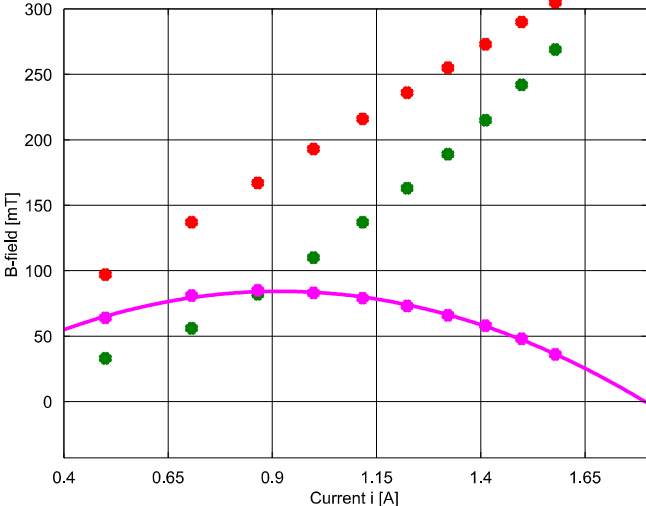


Figure 3.9: PWM losses from iron core

A block diagram of the PWM setup has been created for the experiment above. Figure below shows the required blocks and a HIL Initialize instance block for setting the type of I/O card, the number of PWM channels and the data direction of the digital I/O pins. Two digital pins are used as output pins for setting the Enable signal for the first power stage and providing the VCC signal. The first digital pin 0 has been configured for PWM use. The input to the PWM block sets the duty cycle (any input ranging from 0-1).

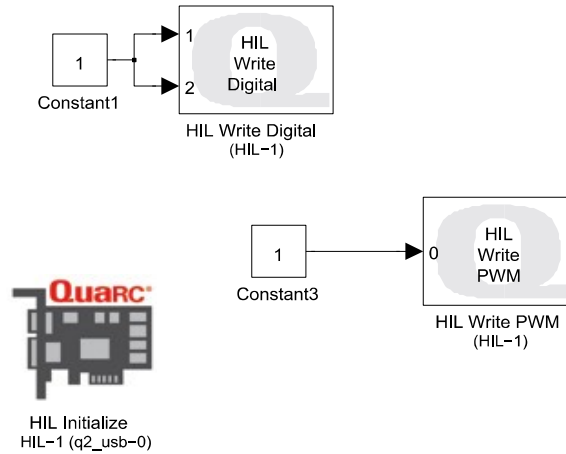


Figure 3.10: PWM output

3.5 Brake model comparison with experiment

The process of magnetic induction has already been discussed at the beginning of this chapter and can be mathematically described by Faraday's law. The magnitude and direction of the force on a particle moving perpendicularly to the exciting B-field is shown in equation 3.2. Rearranging this equation shows that the induced electric field equals the cross product of the velocity and the B-field and that it has the same direction as the force on a given particle:

$$\mathbf{E} = \frac{\mathbf{F}}{q} = \mathbf{v} \times \mathbf{B} \quad (3.31)$$

Considering a rotational motion, the direction of the velocity vector is constantly changing as it is always perpendicular to a given radius. With a uniform B-field that is perpendicular to the conducting disk, this means that the resulting electric field is pointing radially inward or outward, depending on the direction of both the velocity vector and the B-field. The electric field causes the movement of charges on circular paths and the developing currents generate an opposing field which adds up to a net repelling magnetic force, due to Lenz's law and by superposition.

As shown by Wouterse, Schieber and other authors, the low speed region can be modelled by using a simple proportionality between generated force and the angular speed and square of the magnetic field, respectively. This dependency between inputs and output can be seen qualitatively by combining Faraday's equation with equation 3.31 and inserting the result into equation 3.7:

$$\oint \mathbf{E} \cdot d\mathbf{s} = \oint (\mathbf{v} \times \mathbf{B}) \cdot d\mathbf{s} \quad (3.32)$$

The result of this operation is the generated voltage. Due to Ohm's law, the eddy current must be proportional to this voltage. Assuming an unknown parameter for the resistance c_1 , the eddy current is

$$I = c_1 V_{gen} \quad (3.33)$$

Inserting the above result into equation 3.7 reveals the quadratic dependence of the B-field as well as the dependence on the speed:

$$d\mathbf{F} = c_1 V_{gen} (d\mathbf{L} \times \mathbf{B}) = c_1 \left[\oint (\mathbf{v} \times \mathbf{B}) \cdot d\mathbf{s} \right] (d\mathbf{L} \times \mathbf{B}) \quad (3.34)$$

Rewriting this equation as a scalar equation assumes the generated vector field \mathbf{F} to be a net force that is applied to the centre of the shadowed region r_F , as shown in the figure below.

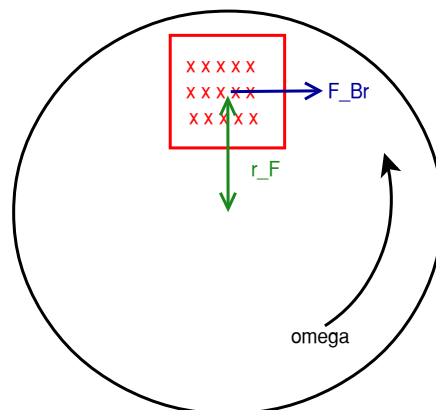


Figure 3.11: Net braking force

Vectors $d\mathbf{s}$ and $d\mathbf{L}$ are summarized as integrated scalars, together with c_1 , yielding a constant c_F :

$$F = c_F v B^2 \quad (3.35)$$

This proportional relation has been confirmed with an experiment which has been performed to evaluate the parameter and also to compare the result with the model developed by Wouterse and Scherf. As mentioned before, Wouterse used a cylindrical core geometry in his calculations and Scherf used a rectangular shape for his Matlab script. Despite different

assumptions about the geometry, Wouterse's model was found to be in close agreement with the actual experiment. The figure for all three functions is shown in the figure below where the dependent variable was calculated using the parameters for the testbench setup. The experiment confirmed the relationship between ω and T_{Br} to be linear. During the sampling, the B-field was fixed.

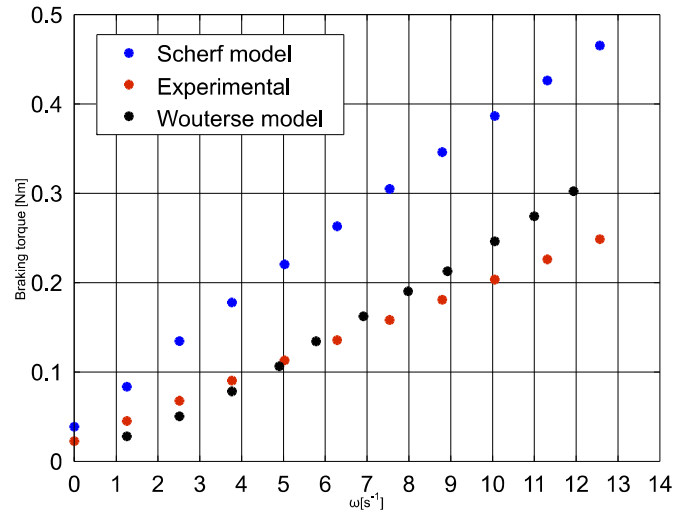


Figure 3.12: Model comparison

The previous experiment is still lacking the linearity between B^2 and T_{Br} , therefore, a set of measurements was taken to determine c_{Br} as in the rearranged equation:

$$c_{Br} = \frac{T_{Br}}{B^2 \cdot \omega} \quad (3.36)$$

The speed of the motor was varied by changing the armature voltage while testing an array of different exciting voltages for the electromagnet. The torque can be calculated from the motor current, as will be explained in the error calculations following. Propagation of uncertainty was determined by first evaluating the relative standard errors of each physical quantity and then calculating the propagated relative error of c_{Br} using the formula below:

$$\frac{\Delta c_{Br}}{c_{Br}} = \frac{\Delta T_{Br}}{T_{Br}} + 2 \cdot \frac{\Delta B}{B} + \frac{\Delta \omega}{\omega} \quad (3.37)$$

The relative error is calculated by dividing the standard error of mean by the mean value of the sampled data. The standard error of mean ω is calculated according to

$$SEM = \frac{s}{\sqrt{N}} = \frac{\sqrt{\left(\frac{1}{N} \sum_{i=1}^N (x_i - x_{mean})^2\right)}}{\sqrt{N}} \quad (3.38)$$

where s is the sample standard deviation, N the number of samples, x_i the i th sample and x_{mean} the mean value of the sampled data. This analysis was carried out for one set of fixed samples to be able to estimate the absolute error of the brake parameter. With the relative error, the absolute error can be calculated by multiplying the error percentage with the mean value of the quantity. For further refinement, a multiple non-linear regression analysis should be performed when deriving a brake model from the wind turbine setup. Verification tests allow for an estimate of the error band. For the testbench experiments described in this chapter, the parameter estimation was found to be sufficiently accurate.

The braking torque has been determined indirectly by measuring the motor armature current. The idle current due to bearing friction was measured beforehand by taking current samples of the free running motor armature and subtracted from the motor current. In total, 25 samples were taken and the absolute error of each value was calculated by subtracting the minimum value from the maximum value of each sampled quantity. The absolute error of the friction current was $i_{fr_err} = 0.01$ A and the absolute error of the motor current was found to be $i_{M_err} = 0.004$ A. The absolute error of the braking current is therefore $i_{Br_err} = (0.01+0.004)$ A = 0.014 A and the actual value is calculated by subtracting the mean values $i_{Br} = i_M - i_{fr} = (0.307 - 0.057)$ A = 0.251. The braking current is therefore $i_{Br}=0.251 \pm 0.014$ A with a relative error of $\Delta i_{Br}/i_{Br}=0.056$. The relative error for the braking torque can be calculated using

$$\frac{\Delta T_{Br}}{T_{Br}} = \frac{\Delta k_m}{k_m} + \frac{\Delta i_{Br}}{i_{Br}} \quad (3.39)$$

A Matlab command calculates the relative errors from the sampled data, such as

```
>> rel_SEM_k_m=(std(k_m) / sqrt(length(k_m))) / mean(k_m)
```

where k_m is a vector with the samples of the generator constant. It calculates the standard deviation, divides the result by the square root of the number of samples and divides the latter by the mean value of the vector. The relative error of the braking torque has been calculated to $\Delta T_{Br}/T_{Br} = 0.02 + 0.056 = 0.076$ and the mean value is $T_{Br} = k_m \times i_{Br} = 0.562$ Vs $\times 0.251$ A = 0.141 Nm. The braking torque is therefore $T_{Br}=0.141 \pm 0.011$ Nm. The braking parameter has been calculated accordingly using formula 3.37. With $\Delta\omega/\omega = 0.002$, $\Delta B/B = 0.01$, mean values of $\omega = 9.26$, $B = 227$ mT, the braking parameter c_{Br} was found to be $c_{Br} = 0.31 \pm 0.03$ A² s m⁴ Nm⁻¹. with a relative error of $\Delta c_{Br}/c_{Br} = 0.1$.

As demonstrated before, the low-speed model developed by Wouterse showed close resemblance to the experiment above using a fixed B-field. Using the geometric parameters of the test bench and inserting the latter into Wouterse's equation where the diameter was assumed to be the diagonal of the square core cross-section, it was found that the parameter derived above only differed by 1.3% from Wouterse's model. According to his formula, the parameter is $c_{Br} = 0.35$, corresponding to the parameters

$$c_{Br} = \frac{\pi}{4\rho} D^2 d C R^2 = 0.35 \tag{3.40}$$

3.6 Magnetic Field B

The magnetic H-field is directly proportional to the excitation current whereas the magnetic field strength is related to the H-field by the permeability μ which depends on the core material. Hysteresis effects were found to be negligible; the soft iron material was chosen for the experiments as it exhibits a narrower hysteresis loop. Figure 3.13 shows the material hysteresis which only consists of a small hysteresis band about the origin. The author refers to the hysteresis curve to as a Rayleigh curve within larger hysteresis loops where the outer loops are not reached due to the excitation current limit [46].

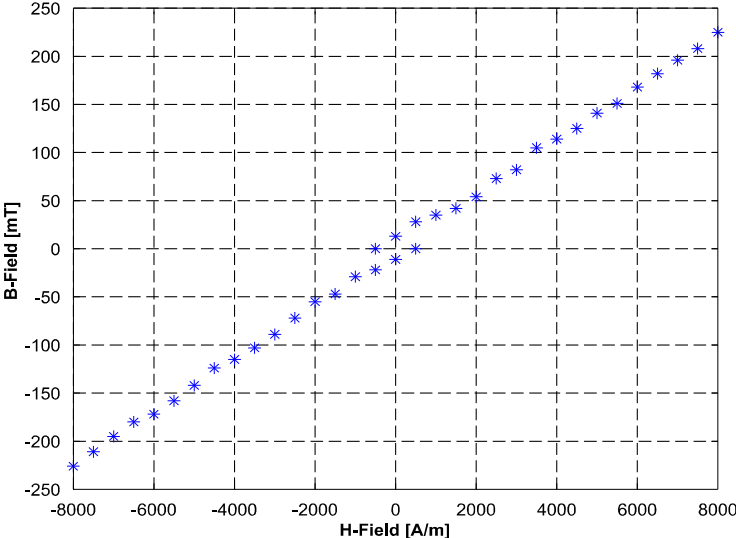


Figure 3.13: Hysteresis: H-field – B-field [46]

The B-field across the air gap, can be derived by using Ampere's law and Gauss's law. The following simplifications are made using Ampere's law for free currents in a single conductor:

$$\oint \mathbf{H} \cdot d\mathbf{L} = \mu_0 \cdot \iint \mathbf{J} \cdot \mathbf{n} \cdot dA = I_{enc} \quad (3.41)$$

The path of the integral on the left hand side is the length of the average magnetic path. It divides into the path across the gap and the remaining path along the core material. Therefore, equation 3.41 becomes

$$N \cdot I = H_c \cdot L_c + H_g \cdot L_g \quad (3.42)$$

As already mentioned, the magnetic H-field is related to the B-field by the material permeability

$$\mathbf{H} = \mu \cdot \mathbf{B} = \mu_0 \cdot \mu_r \cdot \mathbf{B} \quad (3.43)$$

where μ_r is the relative permeability of the material and μ_0 the permeability of free space. Combining the latter two equations yields

$$N \cdot I = \frac{B_c}{\mu_0 \cdot \mu_r} \cdot l_c + \frac{B_g}{\mu_0} \cdot l_g \quad (3.44)$$

Gauss's law demands that the magnetic flux through a closed surface should be zero. Thereby, no flux can escape the magnetic circuit and the flux leaving the core at the beginning of the air gap must be entering the magnetic core at the other end. This also means that the total flux leaving the core must equal to the total flux in the air gap

$$\Phi_c = \Phi_g = B_c \cdot A_c = B_g \cdot A_g \quad (3.45)$$

and therefore

$$B_c = \frac{B_g \cdot A_g}{A_c} \quad (3.46)$$

Entering equation 3.46 into equation 3.44 reveals the reluctance of each path:

$$N \cdot I = B_g \cdot A_g \left(\frac{l_c}{\mu_0 \cdot \mu_r \cdot A_c} + \frac{l_g}{\mu_0 \cdot A_g} \right) = B_g \cdot A_g \cdot (R_c + R_g) \quad (3.47)$$

The reluctance of the core is considerably less than the reluctance of the air gap due to the high relative permeability of iron and hence the term can be neglected. Over a range of different exciting voltages, μ_r is larger than 1000 for iron [62]. Equation 3.47 then simplifies to

$$N \cdot I = \frac{B_g \cdot l_g}{\mu_0} \quad (3.48)$$

It can be seen that under all above considerations, B across the gap is indeed proportional to the exciting current.

3.7 Complete Simulink model

In the following section, deriving the DC motor model is described and the parameter estimation documented. After the DC motor model, the section moves on to the brake model previously derived. The section then finishes with documenting the entire plant model.

3.7.1 DC Motor

The two governing equations for a DC electromechanical converter are derived using Kirchhoff's voltage law and Newton's second law of motion. Input to the system is the motor voltage and the desired output for the brake model is the angular velocity.

The equivalent circuit for an armature driven motor is shown in figure 3.14 and consists of the supply voltage V_m , the voltage across the armature resistance R_a in the figure, the transient voltage across the inductance L_a and the generated opposing voltage V_g .

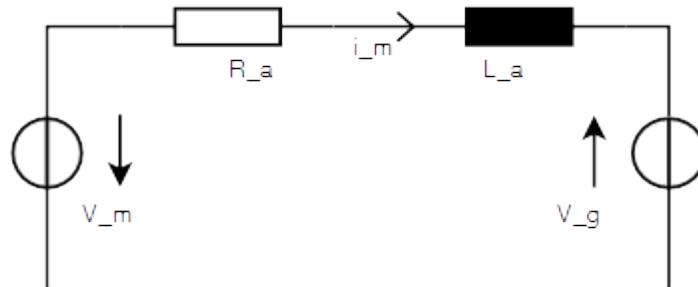


Figure 3.14: Motor equivalent circuit

The generated voltage is proportional to the angular velocity given by

$$V_g = k_m \cdot \omega_m \quad (3.49)$$

with k_m , the motor constant, which is also referred to as the generator or torque constant. k_m is a parameter specific to the armature of the motor and can be measured, as will be shown below.

Summing all voltages clockwise yields the motor equivalent circuit equation

$$-V_m + R_a \cdot i_m + \frac{di_m}{dt} \cdot L_a + k_m \cdot \omega = 0 \quad (3.50)$$

Rearranging for di/dt , this equation represents a first order differential equation where the current i_m is the state variable in state-space:

$$\frac{di_m}{dt} = \frac{-k_m}{L_a} \cdot \omega - \frac{R_a}{L_a} \cdot i_m + \frac{1}{L_a} \cdot V_m \quad (3.51)$$

For estimating k_m , equation 3.51 can be simplified if the electric time constant is negligible. The complex equation for an inductance in series with its winding resistance is given by

$$I(s) = \frac{1}{L} \cdot \frac{1}{s(s + \frac{R}{L})} \quad (3.52)$$

If a step voltage is supplied, this form directly yields the electric time constant in time domain, i. e., if L_a is found to be significantly smaller than R_a , then $\tau = R_a/L_a \approx 0$:

$$i(t) = \frac{1}{L} \cdot \frac{L}{R} \cdot (1 - e^{-\frac{R}{L}t}) \quad (3.53)$$

With this simplification, equation 3.51 can be rewritten as

$$-V_m + R_a \cdot I_m + k_m \cdot \Omega = 0 \quad (3.54)$$

or

$$k_m = \frac{V_m - R_a \cdot I_m}{\Omega} \quad (3.55)$$

Calculating k_m from 10 values of each sampled physical quantity in steady state, the constant was estimated to be 0.565 Vs or 0.565 Nm/A, both in SI units, yielding the generator constant and the torque constant, respectively. Both constants are equal, as will be explained below. The armature resistance was estimated by stalling the motor to further reduce equation 3.51. Since there is no generating voltage, the armature current is directly proportional to the motor voltage and therefore R_a can be calculated from a number of samples of V_m and I_m . Again, R_a was calculated by taking 10 samples in total and it was estimated to be 10 Ohms. The winding inductance was estimated with a voltage bump test and stalling the motor again. Using the time constant τ_{el} , the inductance could be calculated from:

$$L_a = \tau_{el} \cdot R_a \quad (3.56)$$

where the time constant was determined using graphical system identification.

The DC motor includes a gear box and therefore, measuring the motor constant results in the gears being reflected in the constant, thus the gears do not need to be included in the model. A second linearly independent state variable has to be found, the angular speed. If the speed is the only variable of interest and the angular displacement can be neglected, only two equations are required as both equations are first order equations. Using Newton's law, which assumes the net force of the rotating armature be zero, yields:

$$-T_j + T_m = 0 \quad (3.57)$$

Other torques such as the braking torque are omitted at this point. The T_j is proportional to the angular acceleration:

$$T_j = J \cdot \left(\frac{d\omega}{dt} \right) \quad (3.58)$$

where J is the entire inertial load of the armature. With the motor constant known, the motor torque can be calculated with

$$T_m = k_m \cdot i \quad (3.59)$$

Based on the introduction of this chapter, equations 3.56 and 3.59 are understood by imagining a single current carrying square loop in a DC motor. It is subject to a force proportional to the current over the length of the wire. Constant factors of proportionality are the magnetic field strength B and the length L of the wire and the force is generated twice. The resulting torque is then:

$$T_m = 2 \cdot B \cdot L \cdot r \cdot i \quad (3.60)$$

k_m is increased by adding numerous windings. It may seem surprising that the torque does not vary sinusoidally as a rotational motion would vary the angle between the vectors $d\mathbf{l}$ and \mathbf{B} , according to equation 3.7 and 3.8. However, this is only the case for a straight field and the magnets of DC motors are designed such that the field is pointing in the radial direction when considering cylindrical coordinates. This means that the angle between the conductor and the B-field is always at right angles. The generated voltage can be derived from Faraday's law of induction. The magnetic field strength is uniform and the area is constant, i. e. the dot product can be resolved:

$$V_{ind} = - \iint \frac{d}{dt} (\mathbf{B} \cdot \mathbf{n}) da = - \iint |\mathbf{B}| \cdot \frac{d}{dt} \cdot \cos \theta dA \quad (3.61)$$

With $\theta = \omega t$, the above equation becomes

$$V_{ind} = - |\mathbf{B}| \cdot \frac{d}{dt} \cdot \cos(\omega t) \cdot \iint da \quad (3.62)$$

Taking the derivative and integrating over the area yields

$$V_{ind} = 2 \cdot r \cdot l \cdot B \cdot \omega \cdot \sin(\omega t) \quad (3.63)$$

Again, the geometry of the magnets ensures that the sine of the angle is always at a maximum since the unit vector of the field, a_ϕ , is perpendicular to the area normal vector found in the dot product of Faraday's law. As a result, the induced voltage is proportional to the angular velocity:

$$V_{ind} = 2 \cdot r \cdot l \cdot B \cdot \omega \quad (3.64)$$

Comparing the constant factors in equation 3.60 and 3.64 shows that they are equivalent.

Substituting equations 3.56, 3.58 and 3.59 into equation 3.50 and 3.57 yields in time domain

$$-V_m + R_a \cdot i + \frac{di}{dt} \cdot L + k_m \cdot \omega = 0 \quad (3.65)$$

$$-J \cdot \frac{d\omega}{dt} + k_m \cdot i = 0 \quad (3.66)$$

and in Laplace domain

$$-V_m + R_a \cdot I + s \cdot I \cdot L + k_m \cdot \Omega \quad (3.67)$$

$$-J \cdot s \cdot \Omega + k_m \cdot I = 0 \quad (3.68)$$

The open loop transfer function from the voltage being applied to the resulting shaft speed can be found by substituting equation 3.68 into 3.67 and rearranging for $G(s)$:

$$G(s) = \frac{\Omega(s)}{V_m(s)} = \frac{k_m}{J \cdot L \cdot s^2 + J \cdot R_a \cdot s + k_m^2} \quad (3.69)$$

A bump test reveals this transfer function to be linear, i. e. a first order step response. This is owing to the fact that the inductance is usually significantly smaller than the resistance of the armature, yielding a short and invisible current transient. The first term in the denominator is therefore approaching zero and can be neglected. Equation 3.69 then simplifies to

$$\frac{\Omega}{V_m} = \frac{k_m}{J \cdot R_a \cdot s + k_m^2} = \frac{1}{k_m} \cdot \frac{1}{\frac{R_a \cdot J}{k_m} \cdot s + 1} \quad (3.70)$$

A block diagram can be derived using the basic Simulink blocks gain, sum and subsystem input/ output blocks. The Simulink motor model is best derived from the Kirchhoff equation in equilibrium 3.50

$$-V_m + R_a I_m + k_m \omega = 0 \quad (3.71)$$

and rearranging for I_m :

$$I_m = \frac{1}{R_a} (V_m - k_m \omega) \quad (3.72)$$

and the torque equation 3.59 to yield the output T_m as shown in the figure below:

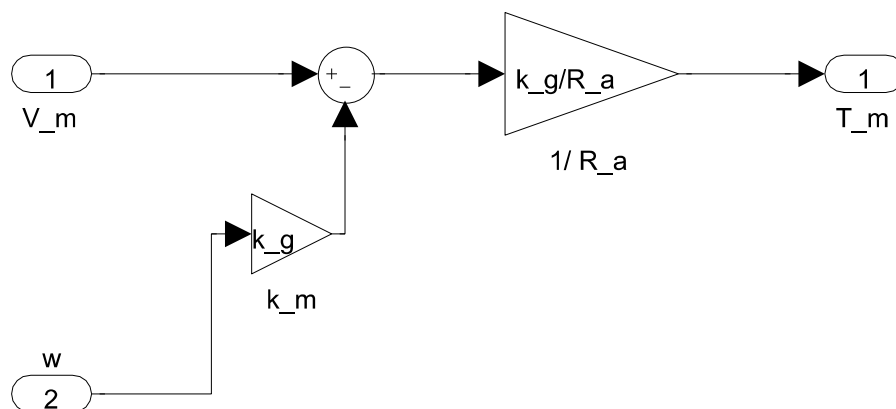


Figure 3.15: Motor model subsystem

The torques are summed up in the upper model which also yields the angular speed. The subsystem diagram shown takes the armature voltage V_m and ω as input, calculates the difference between V_m and the generated voltage and then the motor current and torque, respectively, by multiplying the voltage with the generator constant divided by the armature resistance.

3.7.2 Brake model

Figure 3.16 below shows the Simulink model of the brake. In order to use the brake model derived in section 3.5 for comparison to the HIL experiments, it still needs to be adapted to account for PWM eddy current losses, as given in section 3.4.4. This was done by adding the polynomial function obtained from the polynomial fit. The coil current is multiplied by both theoretical and loss functions and the loss result subtracted from the theoretical B-field. The complete brake model including the adaptation of the B-field is shown in figure below. The brake was modelled using a subsystem that receives its inputs from the level above, i. e. the coil voltage and the feedback of the speed. The former input is limited by a saturation block since the controller signal can exceed the physical limitations. The block limits the voltage to 0 – 15V. The coil current is calculated using the impedance. As explained earlier, the B-field is theoretically calculated from the current and then run through a polynomial loss function that outputs the loss depending on the current applied. The loss is then subtracted from the theoretical B-field given in mT and converted to T for unit matching purposes. The strength of the field is squared, multiplied by the angular speed obtained from the output of the system and multiplied by the brake constant that was evaluated by the experiments previously explained. The subsystem then calculates the resulting torque in Nm.

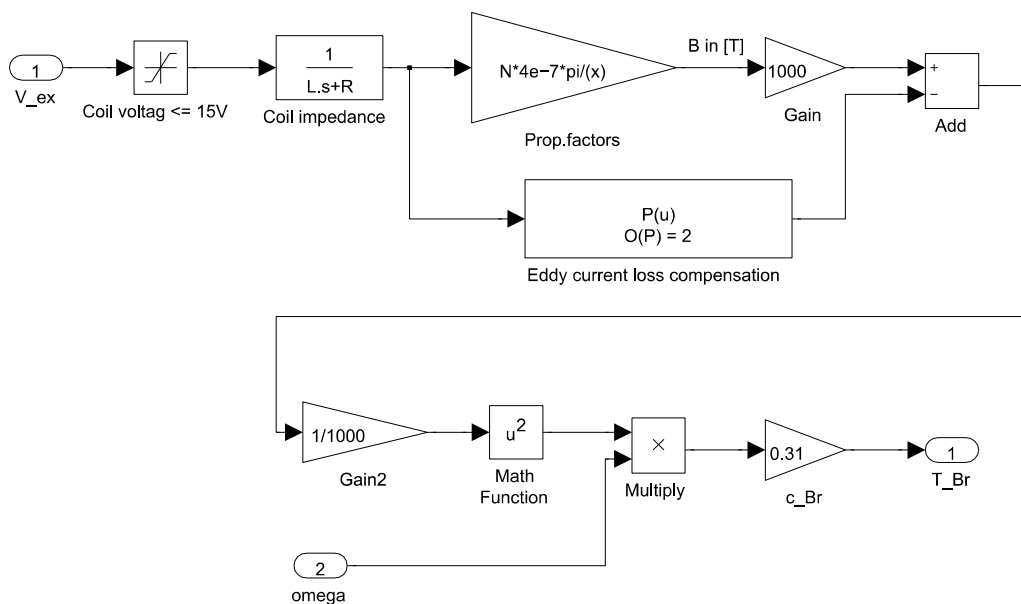


Figure 3.16: Brake model subsystem

3.7.3 Complete model

In this section, the DC motor model and the brake model are combined and an additional feedback path is shown. The parameters of the test bench prototype can be found in the

appendix. The basic equation that was used for modelling the system in Simulink is Newton's second law of motion for rotation. It is given by

$$T = \sum T_i = J \dot{\omega} \quad (3.73)$$

and the torques applied to the low speed shaft are the motor torque, the braking torque and a frictional torque from the mechanical setup. The modelling equation is therefore

$$J \frac{d\omega}{dt} = T_M - T_{Br} - T_{Fr} \quad (3.74)$$

The frictional torque was found to be nearly constant once the shaft is rotating. The subsystem of the equation above is given in the figure below. It includes the inputs to both motor and brake subsystem, which are the control signal for the brake and the feedback paths of ω to both models; the angular speed as output to the upper model, the sum of torques and the calculation of the angular speed. The total shaft torque is divided by the rotor inertia to yield the angular acceleration which is then integrated to provide the angular speed to the upper level. Comparing model simulations with the real system revealed an unmodelled dynamic characteristic which is likely induced by a slip-stick effect of the gears. For completeness, a transport delay was therefore included to match the dynamics of the actual system. It delays pass through of the input for the number of desired simulation steps.

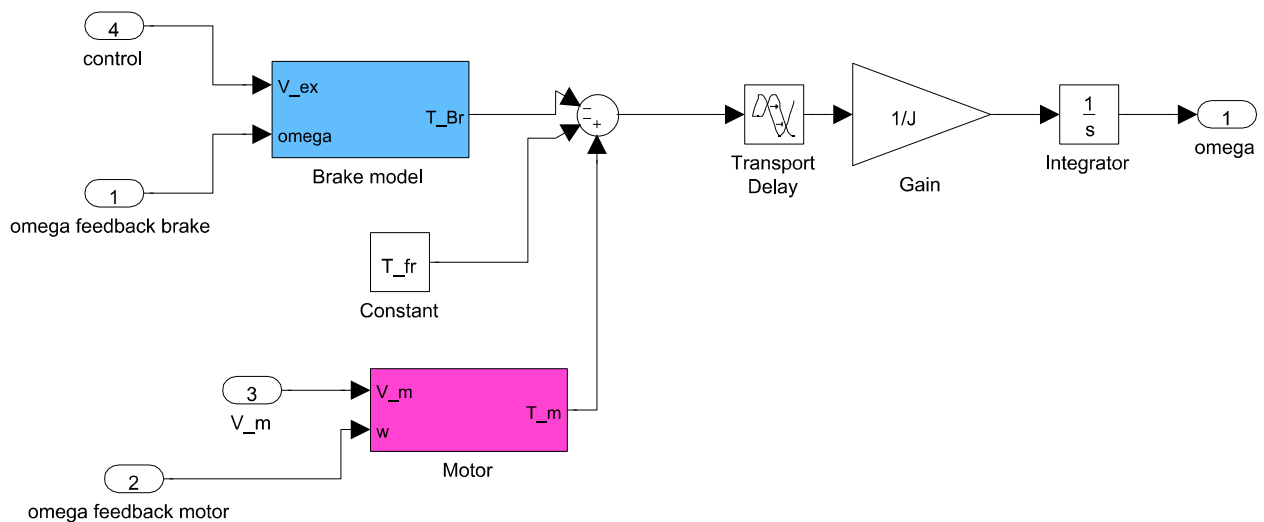


Figure 3.17 Subsystem: sum of torques and calculation of angular speed

Inserting the braking torque $T_{Br}=c_{Br}B^2\omega$ and the steady state equation for the motor current into equation 3.74 yields the complete equation representing figure 3.17 and its subsystems:

$$\frac{d\omega}{dt} = \frac{1}{J} [k_M (-R_a k_M \omega + R_a V_M) - c_{Br} B^2 \omega] \quad (3.75)$$

All constants and parameters are loaded into the simulation by calling an initializing script prior to executing the simulation. The subsystem in figure 3.17 was embedded in a closed loop to provide a feedback path for both the brake model and the motor model as shown in the figure below.

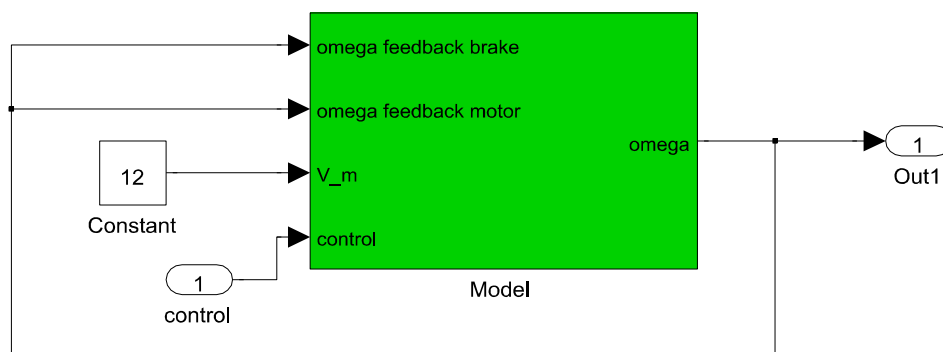


Figure 3.18 Subsystem: Feedback model

The top model then includes the above feedback model, a controller subsystem and a feedback path for speed control. The figure is given below. A control mechanism had to be included in the simulation since the brake should only be switched on when a step is being applied. The decision is made by a switch block which only passes the feedback signal through if the step input, i. e. the reference speed, is non-zero. If a step is applied, the feedback signal is passed through and the reference speed is subtracted from the former. An example would be the free-running angular speed of the motor, which is about $\omega=22\text{rad/s}$ using a motor voltage of $V=12\text{V}$ and a reference speed of $\omega=19\text{rad/s}$ that is switched on after 1s. The error would then calculate to $\Delta\omega=4\text{ s}^{-1}$ once the step is applied and the signal is passed through.

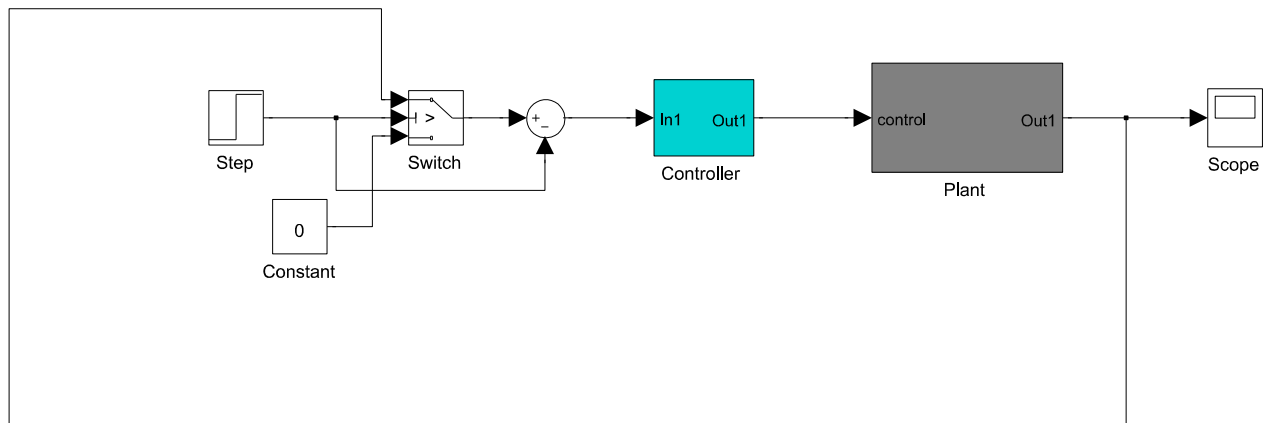


Figure 3.19 Top model: Feedback loop, controller and plant

3.8 Model verification

Finally, the accuracy of the model is evaluated in two different test runs. The test-bench shaft and disk are first driven by different test signals applied to the motor to be able to estimate any unmodelled dynamics. The brake is then included and tested against a variable signal applied to the electromagnet. The first test run is demonstrated in figure 3.20 below. The upper subplot shows the voltage applied to the motor in the form of steps and a ramp signal, the lower subplot shows two model responses, i. e. two independent experimental responses. The motor model has found to be precise as long as a large enough step change is applied such as the first input. However, the remaining inputs and lacking model correlation with the system suggest a strong frictional component, possibly due to an over-determined system. The deviation is present when a smaller step input or a gradual ramp input is applied and particularly, when the exciting voltage is turned off. Two test-runs as in the figure (green and blue) are conducted to verify the repeatability of the characteristics.

Due to the present non-linear behaviour, it was decided to utilize a motor voltage of $V_m=12V$. Lower angular speeds as a result of a step input applied to the electromagnet were not considered to exhibit the same non-linear characteristic due to the torque applied which was also confirmed by the braking experiment with different step/ ramp inputs. Figure 3.21 shows a plot of the latter. The motor runs with the no-load speed when excited with $V_m=12V$ and the brake is driven by the input given in the upper plot. The lower subplot shows the speed response of both the Simulink model as well as the HIL model.

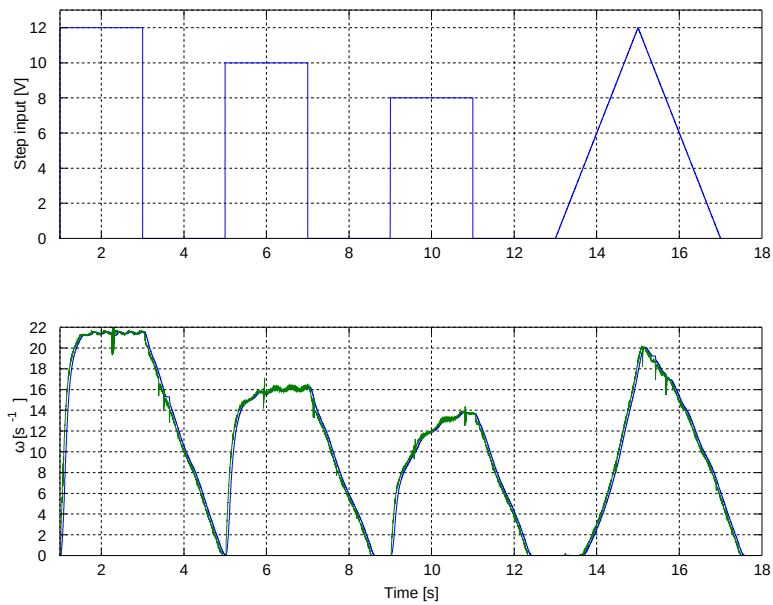


Figure 3.20: Motor model verification

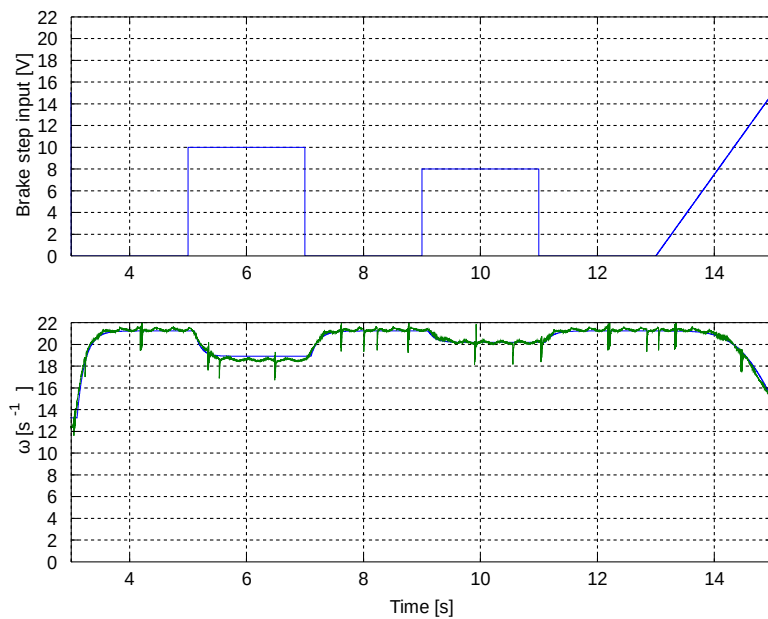


Figure 3.21: Plant model verification

3.9 Controller development

In this section, all steps necessary for developing and refining a brake controller are described in detail. As outlined in the section about the experimental setup, the test bench

design is used for verifying the brake model as well as for carrying out HIL experiments. Initial assumptions led to deriving a model from a closed-loop response, i. e. extracting a first order model graphically from the open loop model. However, Simeu and George's work shows why a typical Laplace model reduction is not possible due to the matrix \mathbf{A} of the state space model which contains a function of the input u . Aside from the input u , the losses induced by the PWM, would have added non-linearity. Therefore, the Simulink model was used for developing a controller by means of a modified Ziegler-Nichols tuning. It has been verified that proportional control did not suffice for eliminating steady state error due to the coil voltage saturation limit. An initial experiment using a brake bump test with the maximum voltage $V=15V$ and the no-load speed of the motor using a voltage $V_m=12V$ was used for verifying the shortest possible transition time, $t \approx 0.5s$. The requirement for the settling time was therefore set to $t=1s$. Once the Ziegler-Nichols tuning using the simulation is completed, the PI controller is then used in HIL iterations and refined according to the response characteristics. The PI controller found can be used for future implementation using an embedded microcontroller such as an Atmega MCU. The Laplace transform of the controller has to be converted first to a z-transform with the sampling time used. Matlab offers a command for these types of conversions, the continuous to digital function 'c2d'.

3.9.1 Ziegler-Nichols tuning

Having a precise model of a plant in Simulink has proven useful for developing a controller using a modified Ziegler-Nichols tuning. Any relevant unmodelled dynamics in the plant can be corrected in a HIL-tuning afterwards. The procedure shown has proven to be effective and repeatable and allows fast prototyping development.

As mentioned before, the brake model contains a saturation block which requires a slightly modified Ziegler-Nichols tuning. K_u , the marginally stable proportional parameter, cannot be found as the controller hits saturation beforehand. Therefore, an alternative parameter, K_q , has to be found which is the equivalent quarter-cycle damping [63] where the first dampened oscillation hump is 4 times the height of the second hump. This parameter was found to be $K_q=4$, i. e. $K_u=2*K_q=8$. The period, T_u , can be assumed to be equal to T_q , which was found to be $T_q=0.33s$. With these parameters, the PI gains can be calculated according to $K_p=0.4*K_u=4$ and $K_i=0.5*K_u/T_q$. They were found to be $K_p=3.2$ and $K_i=12$.

3.9.2 HIL verification

The model developed in Simulink has proven to be precise when compared with the experiment due to the detailed verification process described beforehand. However, if the Simulink model is lacking relevant dynamics, it can nonetheless serve as a valuable starting point for a Ziegler-Nichols tuning and hence, the actual system does not have to be driven into an unstable region. The hardware can then be used to estimate a suitable controller

range and if precision is required, the range found can be automatically tested in defined parameter intervals using automated scripting in Matlab. Automated scripting requires the use of the external mode interface, i. e. the simulation has to be set to 'External Mode'. The Simulink Coder commands `get_param` and `set_param` are used for a bidirectional communication for retrieving and setting values of the simulation and checking whether a simulation/ command has been exited. More specific, in order to initiate a simulation, the following command sequence has to be executed:

```
set_param('HIL_model', 'SimulationCommand', 'connect');
set_param('HIL_model', 'ExtModeCommand', 'ProcessMsg');
set_param('HIL_model', 'SimulationCommand', 'start');
set_param('HIL_model', 'ExtModeCommand', 'ProcessMsg');
```

The above parameter 'SimulationCommand' determines whether to connect to the target or to start a simulation using the model name specified as the first parameter, 'HIL_model' in this instance, and the parameter 'ExtModeCommand' and the option 'ProcessMsg' are used to allow for a time frame for executing the command issued before. This ensures that the function or the script embedding the communication commands do not exit before the external target application has finished executing the command issued beforehand. To query the simulation whether it has exited can be verified with the following code snippet:

```
while ~strcmp(get_param('HIL_model', 'SimulationStatus'), 'stopped')
    set_param('HIL_model', 'ExtModeCommand', 'ProcessMsg');
end
```

These commands are used in a Matlab m-script which utilizes a for-loop for testing different proportional and integral gains. The gains are set in each iteration and sent to the target application to initialize the parameters. The simulation is then executed for the length of time the simulation time is set to and any variables written to workspace during the simulation can be accessed while the script is still executing.

For completion, a PI controller is presented which fulfils the time constraints set at the beginning of this section. The integral gain is set high enough that the required steady-state value is reached within the required settling time. The proportional gain is set in the lower range in order not to saturate the system and therefore risk loosing system stability. The PI controller equation is

$$C(s) = \frac{K_p s + K_i}{s} = \frac{3.2s + 9}{s} \quad (3.76)$$

Figure 3.22 shows the response, i. e. the rotational speed, the driving signal $V(t)$ which has not hit the saturation limit, the speed error and the control signal $U(t)$.

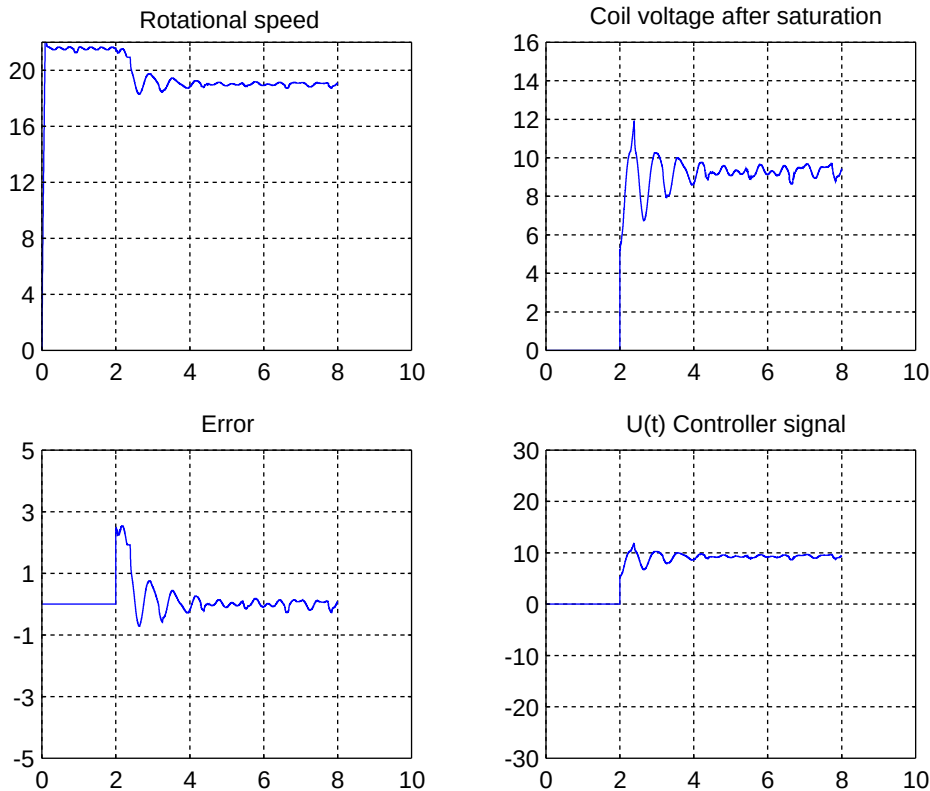


Figure 3.22: HIL controller development

In this chapter, a test bench prototype has been developed for verifying the brake model and for testing rapid prototyping methodology. A novel sensor and power stage setup had to be included in order to interface the Quanser HIL I/O card with the hardware. For measuring rotation, an encoder is utilized which can be used via Quarc encoder blocks in Simulink without any further signal processing. In the wind turbine system, a torque transducer provides the rotational measurement as will be seen in chapter 4.1. As for the power stage, it is recommended to utilize a DAC instead of a PWM in order to avoid the PWM losses encountered when developing the test bench design. For future development, however, a PWM should be considered and a laminated magnet core should be utilized since a rapidly changing magnetic field is likely going to improve the braking power and can thus aid to reduce size and cost of the magnet. In this chapter, the experimentally obtained proportional coefficient relating the braking torque to ω and the square of B strongly suggest a close correlation to the low speed model developed by Wouterse despite its differing geometry. It was therefore decided to use the formula for a scaled WT brake model which is described in chapter 5. The HIL methodology has proven to be valuable for testing different controllers as well as for using automated scripting with iteration.

4. Development of a novel wind turbine model

This chapter begins by introducing an existing experimental wind turbine setup located in the wind engineering laboratory in Huddersfield. In the following section, the results from determining the wind turbine power output characteristics are presented, which will be used to derive a novel numerical wind turbine model towards the end of the chapter. Section 4.3 compares and discusses the suitability of different turbine models in simulations, i. e. utilization of a look-up-table, a CFD-based model for control design and an analytical model. The section on CFD also evaluates the suitability of an analytical torque equation discovered by Park [64]. A perspective on possibilities for future development is then given to conclude the chapter.

4.1 Wind turbine laboratory setup

The VAWT prototype in Huddersfield consists of a stator with 8 inlet vanes as well as a rotor with 8 blades, as shown in figure 4.1 below.



Figure 4.1: VAWT prototype

As its name suggests, the stator position is fixed and the blades serve as wind guide vanes whereas the inner (rotor) part is driven by wind generated in the wind tunnel. The wind turbine interfaces with the Wind Blue Power alternator DC 540 [65] and its rectified output

can be used to connect a load, such as a variable power resistor. The rotor shaft is directly coupled to a torque transducer which also yields the actual rotational speed. Both outputs provide an analogue voltage; the speed output sensitivity has been measured for any future development which yielded 1.4 V/RPM. The transducer measures a torsional moment which requires an opposing torque to the driving rotor torque, i.e. any braking force can only be applied below the transducer. A gear train is connected to the latter that adapts the low speed shaft of the rotor to the shaft of the generator in a 1:8 ratio. The transducer/ gear train/ generator unit is shown in figure below where the red component depicts the torque transducer and the generator can be found below the gear train. The instant wind speed is measured at the outlet of the wind tunnel using a cobra probe [66].



Figure 4.2: Torque transducer, gear train and generator

4.2 Experimental evaluation of power output characteristics

The setup for the experimental determination of the ω -T or ω -P curves required sensing of the rotor torque and the rotor speed as well as the wind speed for reference. The measurements were taken in steady state. Varying the rotor speed was achieved using a variable power resistor with a range of 0-125 Ω . Three data sets for wind speeds of $v_w = [8 \ 9 \ 10]$ m/s existed already, however, the results were found to not correlate with the new data set of $v_w = [11 \ 12 \ 13]$ m/s, the details of which will be discussed in the sections

following. For future development it is strongly recommended to sample more data in order to confirm the model derived at the end of this chapter.

The plot in figure 4.3 below includes all power curves for wind speeds $v_w = [8\ 9\ 10\ 11\ 12\ 13]$ m/s from bottom to top and a polynomial fit generated by the Matlab function 'polyval' for plotting the polynomial function with the same range as the experimental data. The function 'polyfit' was used for finding the coefficient of the polynomial.

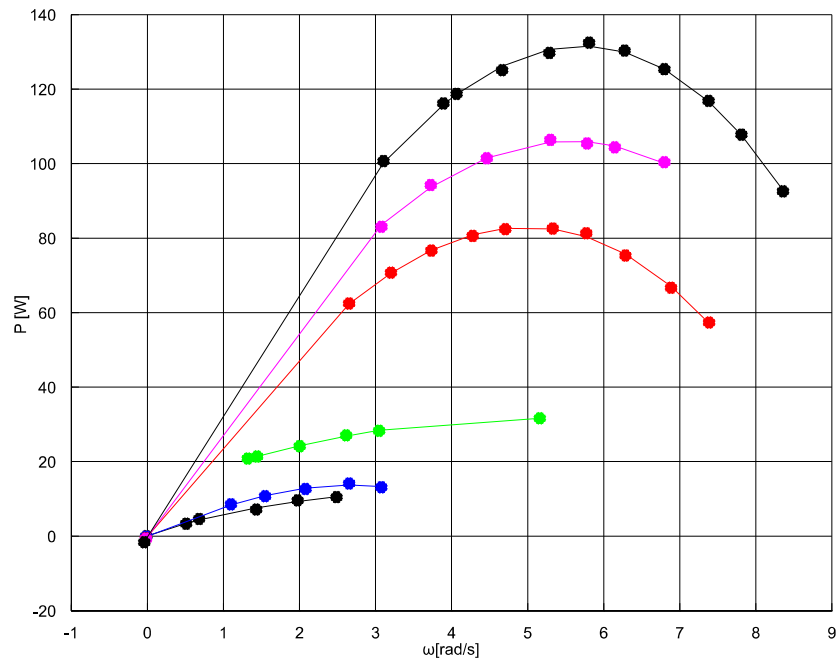


Figure 4.3: Set of power curves for VAWT

Figure 4.3 gives already an indication that the data sets were generated by differing settings in the experimental setup since an extrapolation of the wind speed curves for $v_w=8$ and 9 m/s would obviously not yield the upper curves. The power output curves for $v_w=8$ and 9 m/s as well as for $v_w = 10$ m/s run flatter as compared to the set of curves for $v_w=11$ to 13 m/s.

Possible causes for the differing power curves may be a different outlet size of the wind tunnel or a differing distance between outlet and wind turbine. Equation 1.1 also shows that the air density might be another factor of uncertainty, although it is considered negligible as fluctuations larger than 5 degrees Celsius and large humidity differences are not expected in a laboratory environment. The curve for $v_w = 10$ m/s must have been added with yet another experimental setting.

Since the λ - C_p characteristics describes the non-linear aerodynamic behaviour of the wind turbine, this graphic impression must be confirmed by plotting the λ - C_p curve for all experimental data. As expected, a plot generates three different characteristic curves for each experimental setup. The results are shown in figure 4.4 below. The data was calculated from inserting the experimental data into the power equation and rearranging for C_p :

$$C_p = \frac{2 \cdot P_T}{v^3 \cdot A \cdot \rho} \quad (4.1)$$

The tip speed ratio was calculated accordingly:

$$\lambda(P_T) = \frac{\omega \cdot r_T}{v_W} \quad (4.2)$$

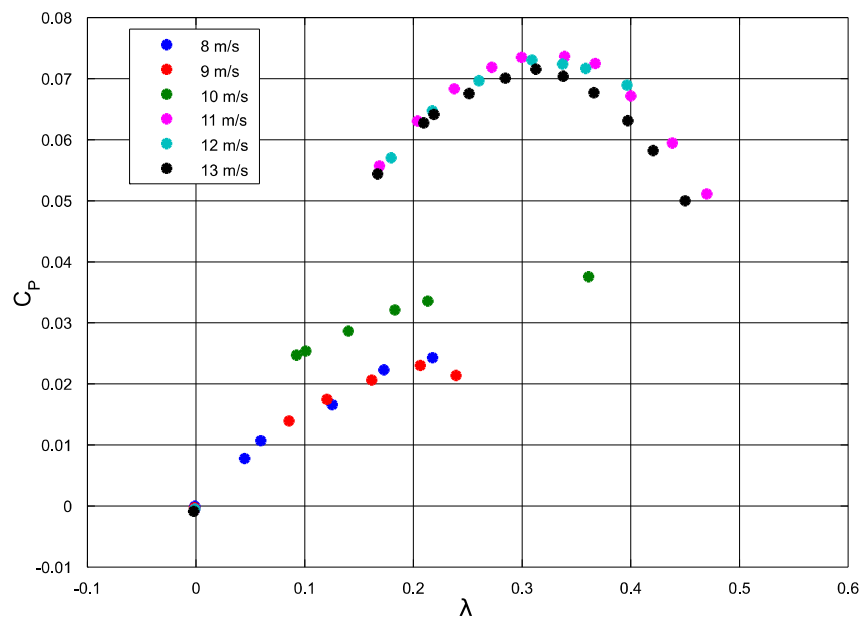


Figure 4.4: Three sets of λ - C_p curves

4.3 Comparison of wind turbine modelling

In the following sections, different modelling methods are presented and their suitability in control design discussed.

4.3.1 Look-up table design

As mentioned in the introduction, a common look-up table (LUT) design uses power feedback and a 1D-LUT or a function for finding the maximum power point as a reference input. In this section, the controller block diagram for the wind turbine is shown which may be used if measuring the wind speed is not planned in the WT setup. The figure below illustrates a typical example for a maximum power curve. Usually, the output of the function or LUT is zero before the turbine can start up and increases linearly with rising wind speeds.

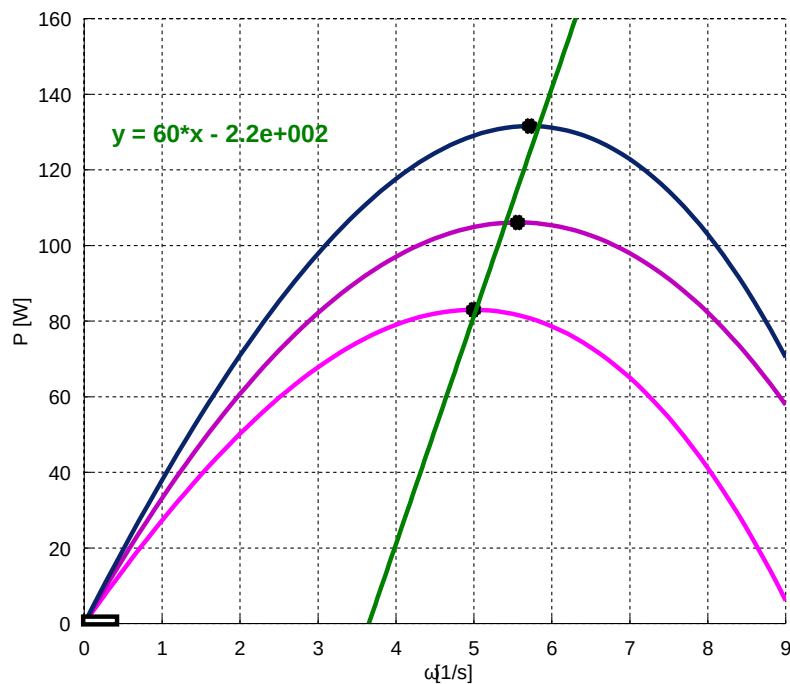


Figure 4.5: Fit of maxima

As shown in the previous section, the power curve has been obtained using the experimental data and a polynomial fit. These polynomial functions are used for finding the zeros of each function and the zeros provide the data for a linear regression. Again, more data should be sampled in a new experiment to ensure that the characteristic is accurate. The linear regression function in the figure above can be used instead of a LUT. A control regime is given in the Simulink block diagram below. It shows the linear function just explained which provides the reference power input to the summing function using the actual speed given by the system. The function parameters are the polynomial coefficients [60 -120]. The summing function then calculates the error, the difference between the power reference and the actual power output of the wind turbine, and the error drives the controller acting on the plant.

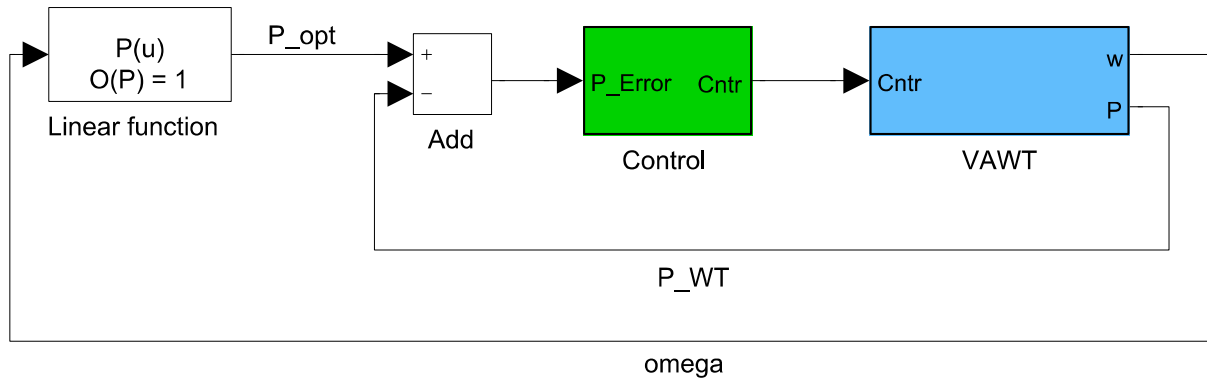


Figure 4.6: Power feedback MPPT

4.3.2 Analytical model

In the introduction, it has been shown that analytical equations exist for the aerodynamics of a HAWT. In this section, an analytical wind turbine model is derived from the aforementioned three sets of data, $v_w=[11\ 12\ 13]$ m/s. As shown in figure 4.4, the data can be used to derive a unique λ -Cp characteristic for the VAWT. A second plot below shows the three sets of data only and two different types of fits. The quadratic fit has been created with a polynomial fit using Matlab and the sinusoidal fit was estimated from the period and the amplitude. The equation can be further refined by using the Curve Fitting Toolbox which provides sinusoidal fitting. The sinusoidal function has been chosen since the fit appears closer to a least-square solution when trying to estimate the distance of the data to both curves on top and the right hand side. However, it is also obvious that the right hand side is lacking some data; therefore, as suggested before, more data should be sampled to confirm the model derived in this section.

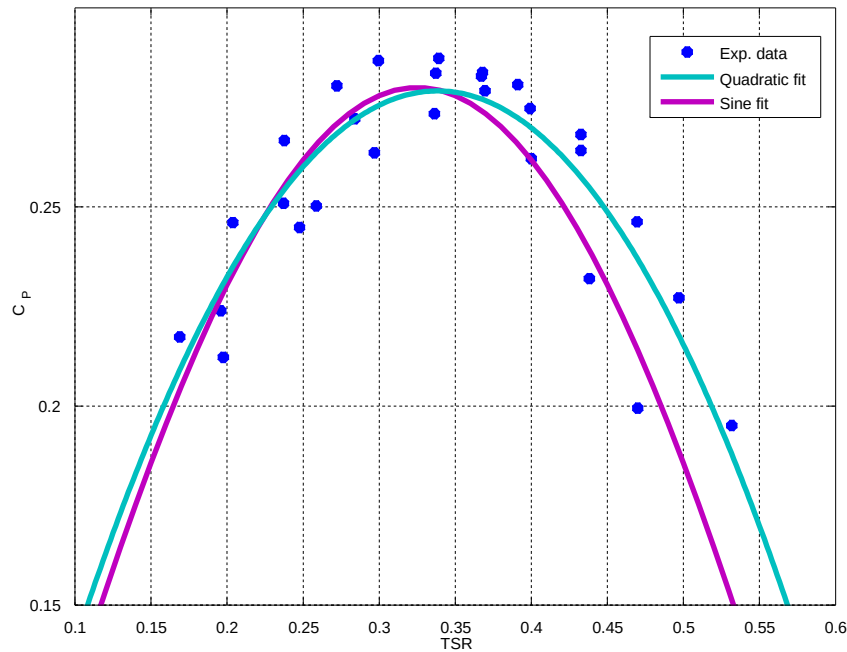


Figure 4.7: Analytical VAWT model

The equation of the sinusoidal fit is given by:

$$C_p = 0.28 * \sin(1.44 * \pi * \lambda) \quad (4.3)$$

This equation represents the key component of the aerodynamic rotor model and can be implemented in Simulink as a function block. The details are given in section 4.4. The optimal TSR can be calculated from the sinusoidal expression, i. e. $\sin(1.44 * \pi * \lambda) = 1$ and therefore $1.44 * \pi * \lambda = \pi/2$. If the value is to be maximal, λ has to take a value of $\lambda = 0.35$.

4.3.3 CFD-based control design

Fluid flow is described by partial differential equations (PDE) as interactions occur in three dimensions, similarly to the development of eddy currents in an unconstrained geometry. The flow of air, as in wind engineering, can be described by two incompressible Navier-Stokes equations. With the advent of computers, and, more recently, high performance computing, it became possible to utilize software packages that solve the governing PDE numerically by discretizing the equations and using initial and boundary conditions. Computational Fluid Dynamics, CFD, is mostly used for designing and optimizing aerodynamic structures in wind engineering. However, some researchers have also utilized CFD simulations in control design. Most of these works use CFD input-output data for system identification purposes and any controller development is based on the model

retrieved from the computational data. One of such examples is the development of an LQG controller for an aeroelastic wing model to suppress flutter [67]. However, Q. Meng et al suggest a flow chart on how to use CFD for system identification purposes and offline-modelling, as well as on how to utilize a developed control algorithm "online" in a CFD simulation [68]. In this scenario, the controller algorithm calculates the difference between a given reference signal and the CFD output data to provide the simulation with varying boundary conditions as inputs. A heat transfer example is chosen to test the feasibility of the procedure.

K. S. Park has used CFD extensively for optimizing VAWT designs in his work [64]. Usage of the current sliding mesh technique has enabled him to capture the dynamics of the interaction between the static as well as the rotating VAWT structures. In his study, he tests different geometric parameters to examine their effect on the flow field. A generic design equation for the turbine torque coefficient has been derived using multiple regression analysis which takes into account all geometric parameters considered in his analysis. The equation for turbine torque then takes the form

$$T_r = 0.311 \rho A r_r v_w^2 C_T \quad (4.4)$$

with r_r being the rotor radius and C_T the torque coefficient, calculated from various geometric parameters such as the number of rotor and stator blades, different inlet/ outlet angles of the rotor and stator, respectively. The power output of a wind turbine as well as the TSR has been introduced in chapter 1.1. Combining both equations (1.1, 1.4) yields

$$P = \frac{1}{2} \rho A \frac{\omega^3 r_r^3}{\lambda^3} C_p \quad (4.5)$$

The instant torque at a certain angular speed can be calculated from

$$T_r = \frac{P}{\omega} = \frac{1}{2} \rho \frac{\omega^2 r_r^3}{\lambda^3} C_p = \frac{1}{2} \rho A \frac{r_r}{\lambda} v_w^2 C_p \quad (4.6)$$

Comparing Park's equation with the generic equation above reveals that the model is lacking information from a control perspective. Performing a parameter match yields:

$$\frac{1}{2} \frac{C_p}{\lambda} = 0.311 C_T \quad (4.7)$$

The turbine characteristics described in this chapter as well as the fit show a non-linear relationship between the TSR and C_p . However, rearranging the above equation shows a

supposedly linear relationship between the TSR and the power coefficient with a given geometry:

$$\lambda = \frac{0.5}{0.311 C_T} C_p \quad (4.8)$$

If the turbine design equation is to be used for modelling purposes, it has to provide the dependency between the TSR and the according C_p value.

The approach of combining CFD simulations with a control algorithm was also tested for feasibility. Current simulations are run by providing a wind speed input as well as a rotational speed for the rotor. As mentioned before, the sliding mesh technique provides means for running transient simulations; however, these transients still refer to the steady state when the rotor has reached its reference speed. Considered transient occurrences, such as torque pulsations, are cyclic. Interfacing the CFD simulations with a control algorithm would require the simulations to allow the rotor speed to be provided externally.

4.4 Development of a novel numerical wind turbine model

In this section, a novel numerical model for the VAWT prototype is provided in Simulink. It includes the sinusoidal equation derived in section 4.3.2 and an equivalent mechanical model which reflects upon the full plant including the generator and the gear train. However, an alternative two-mass model is provided first for future development which includes the single components. In this model, additional parameters have to be obtained from experimental data which are included in the simplified "black box" model utilized in this work.

The first component of the WT modelled is the rotor. Figure 4.8 below shows the entire wind turbine model. The WT subsystem (light-blue), i. e. the rotor model, takes two inputs, the wind speed v_W and the turbine shaft speed ω_T , and has one output, the turbine torque T_T . This subsystem has to be obtained by another trial as the analytical model developed earlier cannot be utilized. Due to the entire conversion chain deployed in the current experiment, the analytical model developed represents a "black-box". Therefore, a new data set for the speed-torque characteristic has to be obtained by using different wind speeds and applying different mechanical torques without the electromechanical conversion chain. The eddy current brake developed would be ideally suited for this type of experiment.

The remaining components of the WT system to be modelled are the mechanical characteristics of the shaft, the gear train and the generator. A mechanical model of the shaft is suggested by Barakati [20] which, as mentioned previously, is used for proposing a model in Simulink. The state space equations are given by:

$$\frac{d\omega_T}{dt} = \frac{1}{J_T} \cdot (T_T - K \cdot \delta\theta - B \cdot \delta\omega) \quad (4.9)$$

$$\frac{d\delta\theta}{dt} = \delta\omega \quad (4.10)$$

$$\frac{d\omega_G}{dt} = \frac{1}{J_G} \cdot \left[\frac{1}{n_{gear}} \cdot (K \cdot \delta\theta + B \cdot \delta\omega) - T_L \right] \quad (4.11)$$

where $\delta\theta$ and $\delta\omega$ are given by:

$$\delta\theta = \theta_T - \frac{\theta_G}{n_{gear}} \quad (4.12)$$

$$\delta\omega = \omega_T - \frac{\omega_G}{n_{gear}} \quad (4.13)$$

The generator load torque T_L in the third equation is assumed to be zero in the model. The equations are derived by modelling the low speed shaft of the wind turbine by an inertial load with a rotational spring and a damper. The stiffness is given by K and the damping by B . The rotor shaft is connected to the generator through a gear train with a gear ratio of $1:n_{gear}$. The high speed shaft of the generator is also modelled by an inertial load. The gears and the shafts are assumed to have a small inertia compared to the WT and the generator and are therefore neglected. The equations above are obtained by a free-body diagram with the speeds/ torques including the directions added to each body. Since the equations are in state-space, a block diagram can be derived directly. The Simulink model is shown below. It shows the WT rotor subsystem just described and sums the rotor output torque and the remaining shaft torques to yield the turbine torque which is given by equation 4.9. The sum of the torques is then divided by the turbine inertia, yielding the angular turbine shaft acceleration which upon integration yields the angular shaft speed. Further integration provides the current angle of the shaft, θ_T . The sum of the latter and the generator angle divided by the gear ratio $1/n_{gear}$ provides the angular difference $\delta\theta$. $\delta\theta$ is then multiplied by the stiffness, K , and added to the angular speed difference multiplied by the damping coefficient B to provide the sum of torques at the generator shaft (refer to equation 4.11, without disturbance torque). The parameters to be determined in this model are the shaft stiffness K , the damping coefficient B , the turbine inertia as well as the generator inertia.

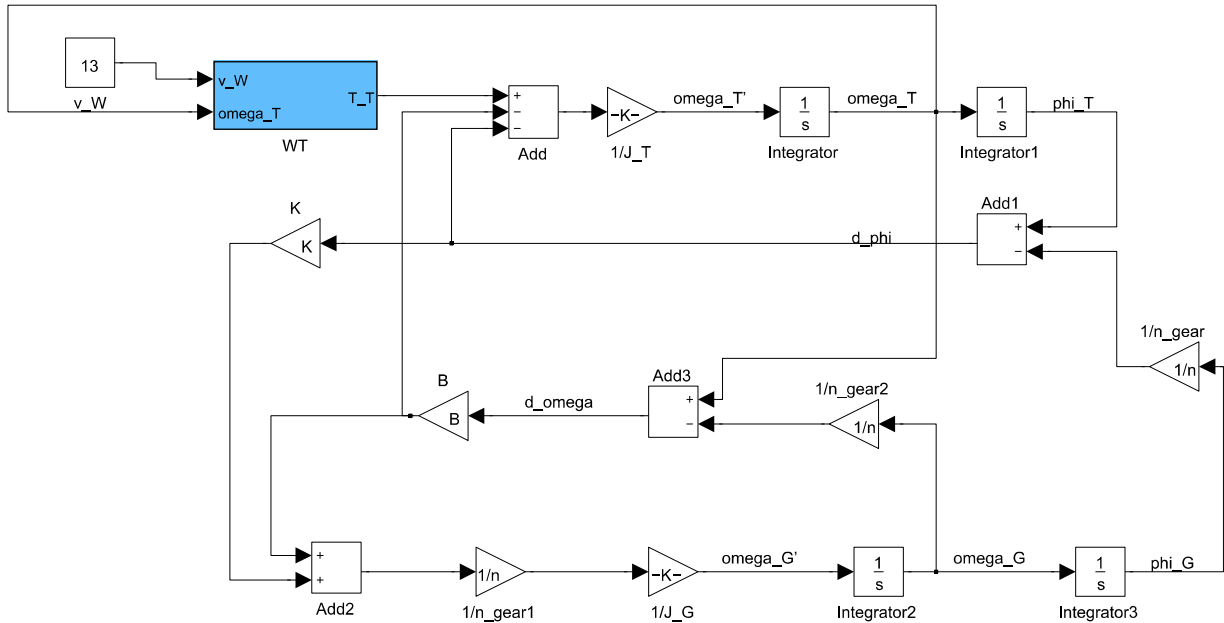


Figure 4.8: Turbine and generator shaft model

In the black-box/ equivalent model, the analytical function for the power coefficient C_p derived earlier is used as well as a simplified equivalent shaft model. For the equivalent rotor model, the TSR is calculated first and input to the sinusoidal function derived previously. The calculated power coefficient C_p is multiplied with the remaining constant parameters of equation 1.1, using a gain block, and the product is then multiplied by the cubed wind speed input via a math function block, yielding the WT power output. Dividing the latter by the angular shaft speed provides the turbine torque output. The equivalent rotor subsystem is shown in figure 4.9 below. The figure following shows the equivalent shaft model including the subsystem. On the left hand side, the wind speed input is shown which is used for applying different step inputs. The angular shaft speed is fed back to the subsystem model for calculating the TSR. The turbine torque provided by the subsystem is divided by the equivalent inertia, an estimation of the latter is provided in the next chapter. An integrator completes the inherent closed-loop system. The block embedded in the feedback path initializes the signal. Note that the system provides no means to prevent a division by zero in the subsystem. For the purposes of this simulation, however, the model suffices to develop for controller development.

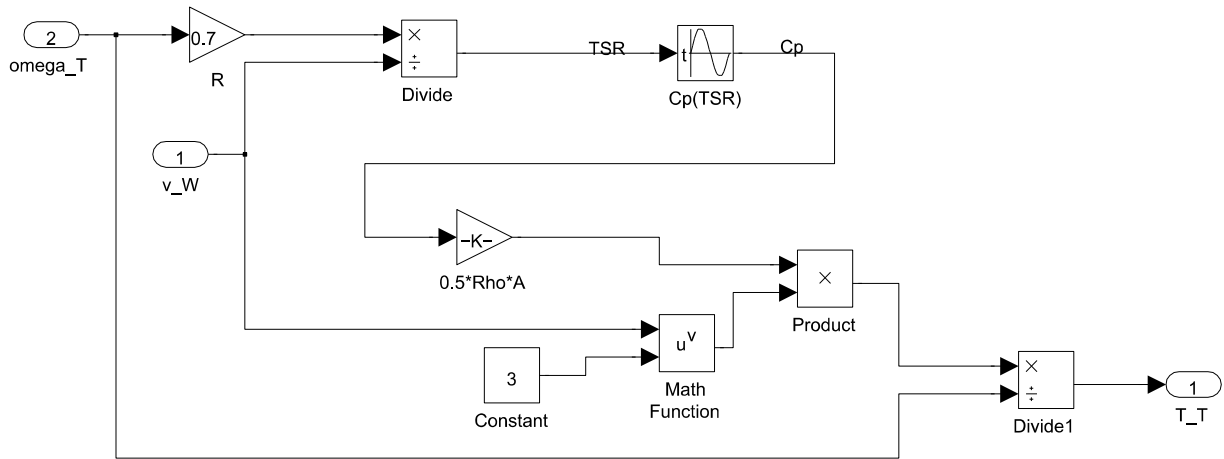


Figure 4.9: Equivalent rotor subsystem

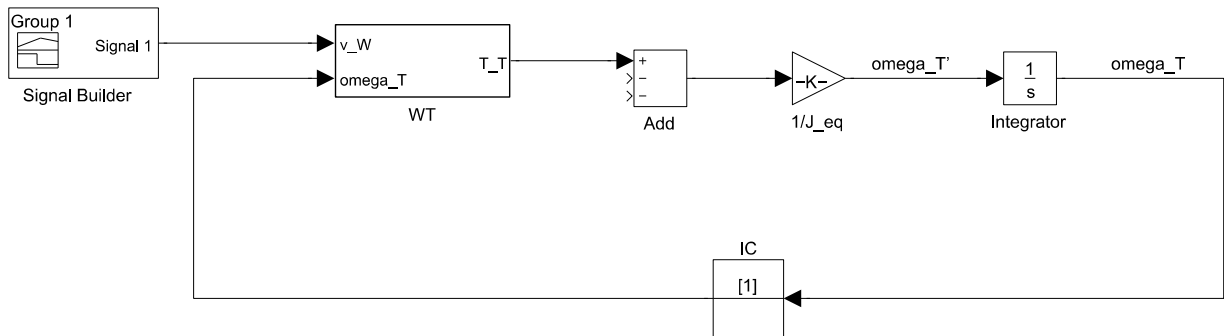


Figure 4.10: Equivalent shaft model

The steady-state no-load speed of the turbine model has been tested by applying three different wind speeds tested in the experimental trial and compared to the sampled data. According to the current data, the model provides a precise no-load speed, however, the equivalent inertia has to be ascertained. Theoretically this could be achieved by applying a wind speed step input to the actual turbine and calculating the mechanical time constant of the first-order system. However, the wind tunnel fan itself starts up with a first-order response, therefore a different solution for finding the turbine inertia would have to be considered. The current simulation response to a step input of $v_w=13\text{m/s}$ is shown in the plot below. The no-load speeds extrapolated from the experimental torque curves (which are presented in the next chapter) at wind speeds $v_w=[11\ 12\ 13]\text{ m/s}$ are $\omega_{\text{exp}}=[10.33\ 11.21\ 11.94]\text{ rad/s}$. The simulation yields a steady-state no-load speed of $\omega_{\text{sim}}=[10.21\ 11.15\ 12.05]\text{ rad/s}$, compared to the former vector the simulation deviates by less than one percent for each value.

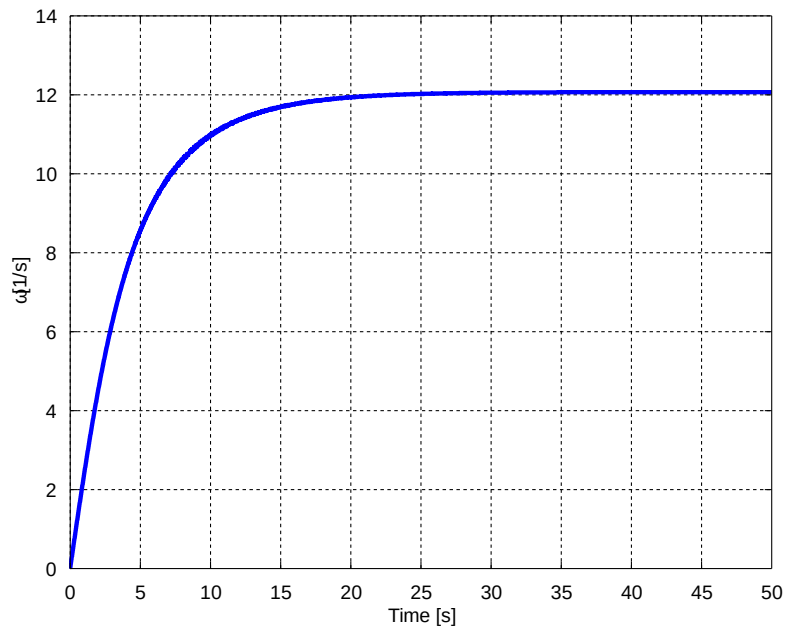


Figure 4.11: WT step response

5. Development of a novel SSWT controller

5.1 Brake design and brake rating

The parameters from the wind turbine rotor were used for an estimate of the overall maximum power that the magnetic brake will need to be able to brake. Equation 1.1 was used for calculating the maximum power the wind turbine prototype could yield. Both parameters C_p and the air density ρ are assumed to be at their maximum, i.e. $C_p = 0.15$ and air density $\rho = 1.3413\text{kg/m}^3$ (assuming dry air, altitude at sea level, i.e. 101.325 kPa, and bottom level temperatures, -10°C). With the swept area $A=1.4\text{m} \times 1\text{m}$, and an expected maximum wind speed of $v_w = 15\text{m/s}$, the maximum power of the WT was found to be approximately 635W.

In order to find a rough estimate for the braking power, the maximum allowable rotational speed is needed first. It was determined by finding the zeros of each experimental ω - T curve using regression analysis in Matlab for $v_w = [11\ 12\ 13]$ m/s, as in figure 5.1 below, and by extrapolating the values found for ω to $v_w = 15$ m/s.

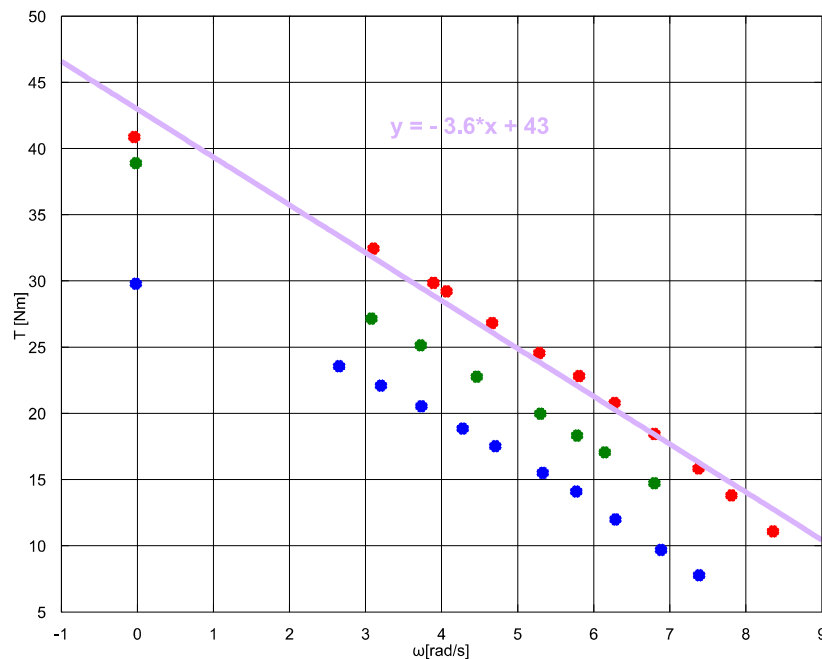


Figure 5.1: Linear regression of torque curves

The equations derived from regression analysis yielded a zero vector $\omega_{\text{zero}} = [10.33\ 11.21\ 11.94]$. With the wind speed vector $v = [11\ 12\ 13]$ and a new vector with inter- and

extrapolating points $vq=11.5:0.5:15$, the maximum allowable rotational speed was found to be $\omega=12.87$ rad/s. The resulting vector was determined using the Matlab command **interp1**($\omega, v, vq, 'pchip'$) which interpolates as well as extrapolates using piecewise cubic polynomials.

The maximum braking torque was calculated using the magnetic braking power formula Wouterse developed for a round core using the correction factor introduced in chapter 3. Wouterse's equation shows the parameters which contribute to the overall power output of a brake. Parameters that enhance the mechanical braking power include the windings of the electromagnet, the reciprocal of the air gap, the thickness of the sheet, the diameter of the magnet core, the conductivity of the sheet material and the radius to the centre of the magnet core. Three of these parameters are constrained, i.e. the thickness of the disk, the air gap and the conductivity. If the thickness of the disk were increased, the air gap would have to be widened accordingly, and a couple millimetres added for alignment tolerances. Including a safety gap is also considered necessary due to the flow interaction between wind and rotor which cause torque pulsations and therefore vibration of the wind turbine system. However, a very wide air gap is undesirable because the magnetic field lines spread out if the gap is too wide, which leads to an inhomogeneous magnetic field and non-linearities. Furthermore, if the conductivity of the disk is increased, it has to be kept in mind that the total moment of inertia might increase as well. Copper, for example, is a better conductor than aluminium but also has a higher density. The increased moment of inertia may be desirable for the braking force but it may be too large a load for the performance of the wind turbine. Therefore, an aluminium alloy with a percentage of copper was the material of choice for the wind turbine system since it is a common alloy as well as a material that is easily machinable. The material selected was AlCuMg₂ (DIN Standard), or AW-2024 (EU Standard), with a resistivity value of $0.018-0.021 \times 10^{-6} \Omega m$. The disk was manufactured at the University of Huddersfield and had to be cut with a water-jetting machine as the copper content did not allow the disk to be made with a laser-cutter. As mentioned previously, the core cross-section was chosen to be rectangular, in this case a geometry of 3 x 5 cm is suggested as the short side is suitable for increasing the radius of the centre point of action R. The measures represent a trade-off between choosing a large enough diagonal for a large braking torque and the weight increase aspect of the magnets since the turbine system should be a compact one.

The magnetic B-field across the air gap was calculated using the following formula as derived in chapter 3.6:

$$B_0 = \frac{N \cdot I \cdot \mu_0}{L_g} = \frac{1000 \cdot 2.5 \cdot 4 \cdot \pi \cdot 10^{-7}}{1.2 \cdot 10^{-2}} \cdot \frac{A \cdot V_s}{A m^2} \approx 0.262 T \quad (5.1)$$

In this case, the electromagnet has to have 1000 windings, it must allow a current of $I = 2.5$ A and the air gap must not be wider than 1.2 cm. Since the turbine is wide enough to accommodate a larger disk, a radius of $A = 30$ cm was chosen. With a rectangular core shape of 3×5 cm, a safety gap of 2 cm towards the rim was included using the geometric relationship according to the sketch in figure 5.2 below (all measurements in cm):

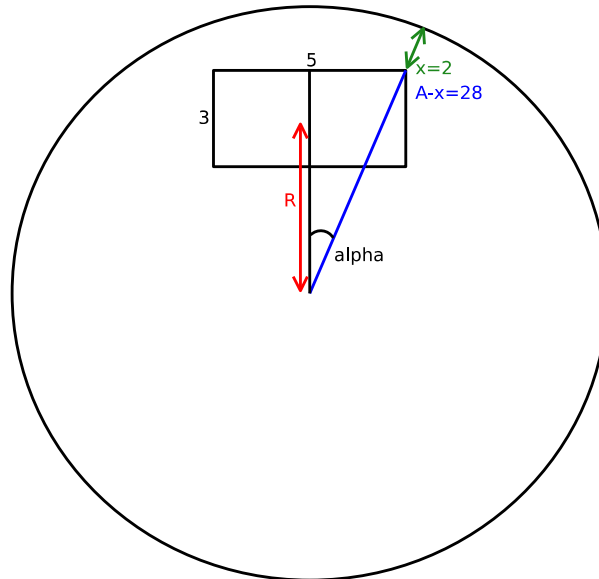


Figure 5.2: Magnetic core placement

The radius R can then be calculated according to

$$\tan(\alpha) = \frac{2.5}{R+1.5}, \alpha = \arcsin\left(\frac{2.5}{A-x}\right) \quad (5.2)$$

Rearranging the above equation yields a radius R of

$$R = \frac{2.5 - \tan(\alpha) \cdot 1.5}{\tan(\alpha)} \approx 26.4 \quad (5.3)$$

With the radius for the net braking torque equal $R = 26.4$ cm and the diagonal of the iron core replacing the diameter with $D \approx 6$ cm, the braking torque coefficient used by Wouterse can be calculated as:

$$C = \frac{1}{2} \left[1 - \frac{1}{4} \frac{1}{\left(1 + \frac{R}{A}\right)^2 \left(A - \frac{R}{D}\right)^2} \right] \approx 0.40 \quad (5.4)$$

Using a disk thickness of $d = 0.8$ cm, a value of $\rho = 0.021 \times 10^{-6}$ Ωm for the aluminium alloy and a maximum allowable angular speed of $\omega_{\max} = 12.9$ rad/s, the total braking power with one magnet calculates to $P_{Br} \approx 326$ W. Using two magnets would therefore theoretically suffice to completely brake the wind turbine to a halt at a wind speed of $v_w = 15$ m/s. Placing the disk on the high speed shaft behind the gear train would further improve the braking power. The current measurement setup also requires the disk to be located below the torque transducer as the sensor requires a differential (torsional) torque.

5.2 Wind turbine dynamics and control requirements

A requirement analysis was based on the braking power calculations introduced in the section above. As shown, the maximum rotational speed at $v_w = 15$ m/s would be $\omega_{\max} = 12.9$ rad/s. Extrapolating the torque-speed curves of the wind turbine yields a maximum rotational speed of about $\omega_{\max} = 17$ rad/s at $v_w = 20$ m/s, which is classified as storm and assumed to be never reached in an urban environment. Wind speeds are lower in urban areas than in countryside environments due to the friction of surfaces and induced turbulences. The braking power at an angular speed of $\omega_{\max} = 17$ rad/s is calculated to be approximately $P_{\max} = 566$ W, again using Wouterse's braking power formula equation. Since this amount of power is only available initially due to the reduction in speed, the following calculation of the shortest transition time is used as the lowest reference.

The braking torque available at $\omega_{\max} = 17$ rad/s is

$$T_{\max} = \frac{P_{\max}}{\omega_{\max}} = \frac{566}{17} \text{ VAs} = 33 \frac{\text{Nm}}{\text{As}} \text{ As} = 33 \text{ Nm} \quad (5.5)$$

With the maximum torque and an estimation of the inertial load of the wind turbine, the maximum angular acceleration can be roughly calculated and hence serve as a basis for defining the requirements for the system. The maximum angular acceleration is

$$\alpha_{\max} = \frac{T_{\max}}{J_{WT}} \quad (5.6)$$

The wind turbine inertia has been estimated as no CAD data was available about the physical parameters of the wind turbine in the laboratory. Since the rotor blades are made from thin aluminium sheets, a rough equivalent representation was used, i. e. a hollow cylinder with a thin aluminium wall and an average radius. The rotational inertia of a hollow

cylinder that rotates about the central axis of its circular cross section can be calculated from

$$J_{WT} = \frac{m}{2} \cdot (r_1^2 + r_2^2) \quad (5.7)$$

where r_1 and r_2 are the inner and outer radius, respectively, and the mass m is determined by

$$m = V \cdot \rho_{Al} = \pi \cdot h \cdot (r_2^2 - r_1^2) \cdot \rho_{Al} \quad (5.8)$$

with ρ_{Al} being the density of aluminium and h the height of the cylinder. With an estimated average radius of 0.85 m, a sheet thickness of 4 mm and an aluminium density of 2850 kg x m⁻³, the higher end of aluminium alloys, the rotational inertia of the rotor would calculate to

$$J_{WT} = \frac{\pi}{2} \cdot h \cdot (r_2^2 - r_1^2) \cdot \rho_{Al} \cdot (r_1^2 + r_2^2) = \frac{\pi}{2} \cdot 1 \cdot (0.854^2 - 0.85^2) \cdot 2850 \cdot (0.854^2 + 0.85^2) \frac{m \cdot m^2 \cdot kg}{m^3} \cdot n \quad (5.9)$$

= 14.1 kg x m². This calculation represents only a rough estimate, since the real rotational inertia cannot be calculated without the actual geometry and the alloy density. Therefore, a safety factor of 1.5 was used to assume a lower maximum acceleration, i. e. $J_{WT} = 21 \text{ kg} \cdot \text{m}^2$.

With the turbine inertial load and the maximum braking torque in extreme weather conditions, the maximum acceleration would be

$$\alpha_{max} = \frac{T_{max}}{J_{WT}} = \frac{33 \text{ kg m}^2}{21 \text{ kg m}^2 \text{ s}^2} = \frac{1.6}{\text{s}^2} \quad (5.10)$$

Given typical wind speeds of around 4 - 6 m/s in urban environments in the UK [69], it is realistic to assume that MPPT should stop at about $\omega_{max} = 12.9 \text{ rad/s}$ which is the no-load speed with a wind speed of 15 m/s. With the previous calculations of the maximum angular acceleration and a maximum difference of $\Delta\omega_{max} = (17 - 13) \text{ rad/s} = 4 \text{ rad/s}$, the shortest possible transition period would be

$$\Delta t = \frac{\Delta\omega_{max}}{\alpha_{max}} = \frac{4 \text{ s}^2}{1.6 \text{ s}} = 2.7 \text{ s} \quad (5.11)$$

As mentioned before, the above settling time calculation represents a theoretical value only since the initial braking power also reduces with decreasing rotational speeds. Therefore, the settling time for transitional periods using applied control is set to be $\Delta t = 4 \text{ s}$.

5.3 Scaled brake model in Simulink

This section provides the details of the wind turbine brake model according to equation 3.18 and 3.19. Figure 5.3 shows a Simulink model of the WT brake. The first input, the voltage V_m , is again limited by a saturation block for a range of 0-15V. The coil current is calculated by dividing the Voltage by the impedance comprised of the inductance and the resistance. Then, the B-field according to formula 5.1 is calculated and squared. The latter is multiplied by ω and a number of different factors which determine the proportional parameter introduced in chapter 3.5. A list of the brake parameters initially loaded into the simulation is given in the appendix.

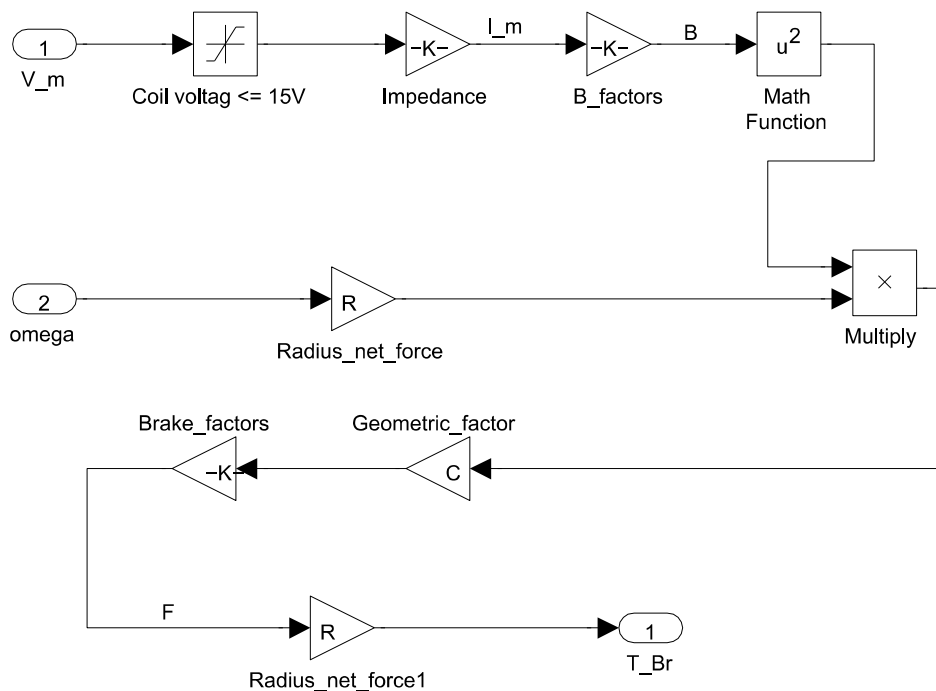


Figure 5.3: Scaled brake model

5.4 Braking to a reference speed above rated wind speeds

In chapter 4.4, a novel wind turbine model has been developed; the control regimes in this chapter are based on the former and the scaled brake model just introduced. In this section, a controller is developed for limiting the shaft speed to a set reference speed before the rated power has been reached [26]. This mode is applicable when a set maximum allowable rotor speed is exceeded before the rated power is reached, i. e. when supervisory control has to switch to a power limiting algorithm. Figure 5.4 shows a block diagram of the closed-loop control system. The variable to be controlled is ω , therefore a closed-loop has to be formed with ω in the feedback path. Furthermore, the shaft speed ω has to be fed back to both the wind turbine and the brake model since both models depend on ω . In this

model, two brakes are deployed, i. e. the braking torque is doubled behind the brake model (light blue in this diagram) due to the added parallel resistance of the coil. Two additional components have to be added to the closed loop; a feedback initializing block has to be included since otherwise a division by zero occurs in the WT model when the simulation is started and second, a logic controller has to be inserted so that the brake is only switched on when the shaft speed has reached the limit. The second input of the switch decides which input is to be passed through: in this case, if ω is larger than 10, the first input is selected which is the reference speed or limit; if ω is smaller than 10, the variable itself is selected and the difference at the summing point becomes zero.

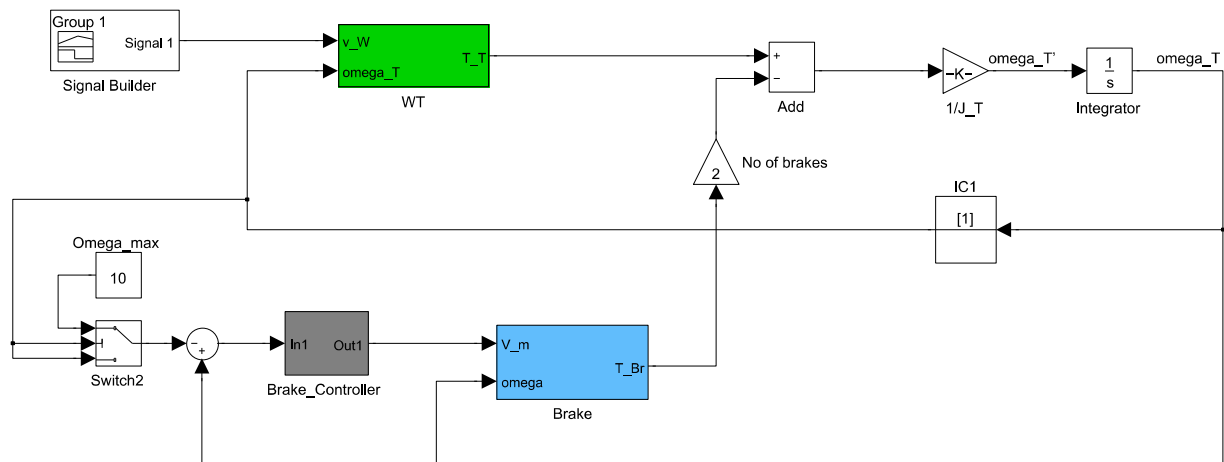


Figure 5.4: Simulink model – max. speed mode

Initial experiments with the wind turbine and the brake as well as the requirement analysis revealed the system to be slowly reacting due to the large inertia. It was predicted therefore that proportional control would suffice since the turbine can hardly react to changes faster than its own dynamics. Moreover, it was found that oscillations of the driving signal from hitting the saturation limit did not affect the performance of the system. Having proportional control only has the advantage of being straightforward to implement in a controller design for an MCU. A K_p value has been selected which does not hit the saturation limit of the driving signal but still eliminates steady-state error. With $K_p=500$, the brake can still reach a reference speed of $\omega=10$ rad/s when a wind speed input of $v_w=17$ m/s is applied.

5.5 Maximum power point tracking

Another simulation has been created for the purpose of MPPT. In this mode, the TSR has to be kept constant at the maximum C_p value, i. e. at $\lambda=0.35$ as shown in chapter 4.3.2. The Simulink model has been built with the same layout as the maximum speed control model,

only the variable to be controlled is λ . Figure 5.5 shows the logic of MPPT. The switch chooses the first input, the reference λ when λ exceeds a value of 0.35. Otherwise λ is subtracted from λ and therefore the error becomes zero. The TSR ratio is calculated using equation 1.4. Note that the wind speeds cannot take a value of zero, otherwise the TSR becomes infinity in the simulation. As it turns out, it also suffices to use a proportional gain in this simulation. Like in section 5.4, K_p is found to yield satisfactory results with a gain of 500.

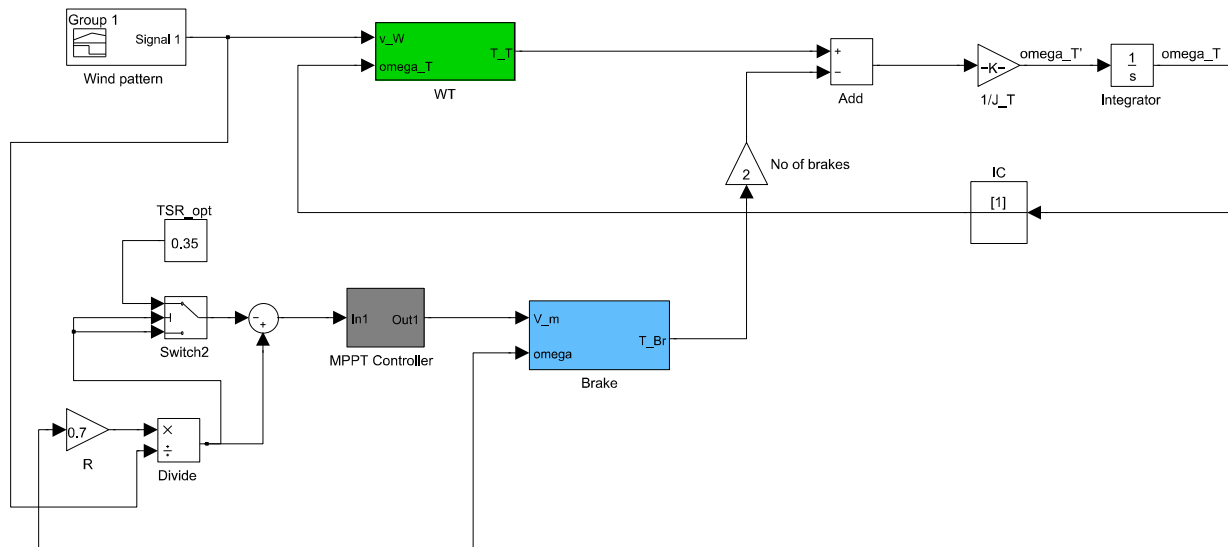


Figure 5.5: Simulink model: MPPT mode

5.6 Supervisory control regime

In this section, a supervisory control regime is suggested which implements the modes described previously. In Matlab/ Simulink, the Stateflow toolbox can be utilized to embed supervisory control in the simulation [70]. The flowchart here has been setup with a final controller design in mind, i. e. for use in an embedded microcontroller such as the ATmega series [71]. This control algorithm only implements supervisory control over the two modes developed in this work; however, it can also be enhanced with other modes. In this example, the algorithm is exclusively dedicated to controlling the wind turbine, i. e. it continuously monitors the rotational speed of the wind turbine and decides which control mode to select and execute. A flow chart is shown in the figure below. Note that the use of delays have not been included here. Delays in a polling MCU are used for synchronization with the actual hardware. In the diagram, only the shaft speed control mode is considered in detail; the MPPT mode is also included, however, the body of the program is hidden in a subroutine block. The program initializes with the start of the wind turbine. Either mode is selected by testing whether a steady-state speed has been established, i. e. if the derivative

of the rotational speed equals zero, and whether the actual wind speed lies in the range the mode is dedicated to. In the diagram, v_{su} denotes the start-up speed, v_{rs} the rated speed (ω_{max}) and v_{rp} the wind speed when rated power is reached. Note that the two while-loops still need to be embedded in another loop that ensures continued execution of the mode selection. The derivative test of ω is suggested to be used as a boolean condition. In speed-limiting mode, the first if-statement tests whether the reference speed has been reached. If not, execution of the program starts at the beginning again. If the reference speed has been reached, the error is calculated by subtracting the reference speed from the measured angular speed. The control signal then calculates to $cntr = error * K_p$ and the next step of the program tests if the controller signal has reached or exceeded the saturation voltage. Once the correct voltage signal has been calculated or set, the duty cycle is calculated from rearranging equation 3.27 to $D = (V_{RMS}/V)^2$. A subroutine block is then responsible for initiating the PWM.

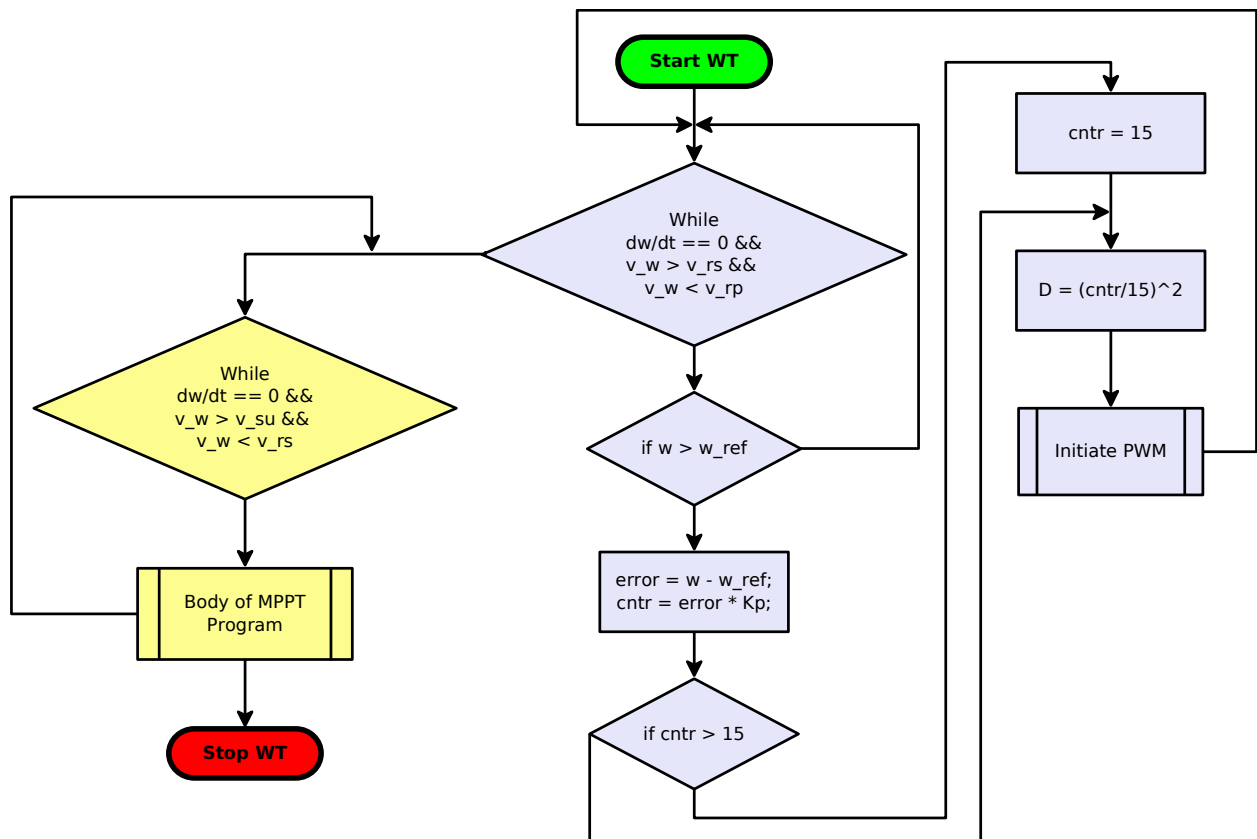


Figure 5.6: Supervisory control

5.7 Performance evaluation

This section discusses the performance of the system and the controller algorithms applied. Different inputs have been utilized to show that the controller performs equally well in each scenario.

5.7.1 Speed control

As said before, different wind speed inputs have been utilized for validation purposes. Figure 5.7 shows the input signal (blue), the open-loop response of the rotor (light blue) and the closed-loop performance of the controller using K_p (red). The slow dynamics discussed previously can be observed in this plot showing both responses. When the first step input falls from 13 rad/s to 3 rad/s, it can be seen that the no-load speed of the turbine stays virtually at the same value as before. The rotational speed is limited to $\omega=10$ rad/s as required in this simulation. Another plot has been created by slightly modifying the Simulink model and the logic for passing through the signal for the summation. In this case, a brake step input is applied when the wind turbine has reached its steady-state value at $v_w=17$ m/s. The switch selects the step input if the input is larger than zero and the feedback signal ω if no step has been applied. The plot in figure 5.8 retrieved from this simulation shows that the settling time requirements were met.

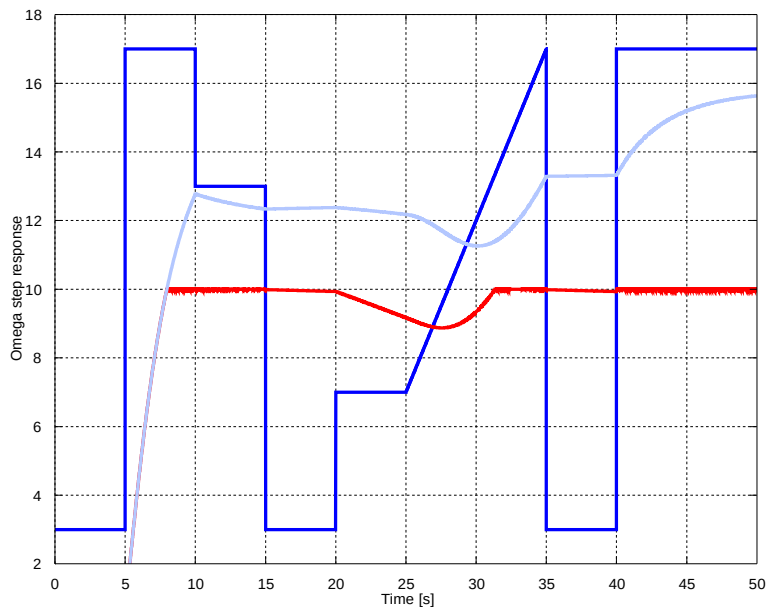


Figure 5.7: Speed control mode

The figure below shows the step response when the brake is switched on after the wind turbine has settled at its no-load speed. In this case, only one magnet has been utilized. The x-axis has been set to only show the wind turbine rotating at its no-load speed before the brake is switched on.

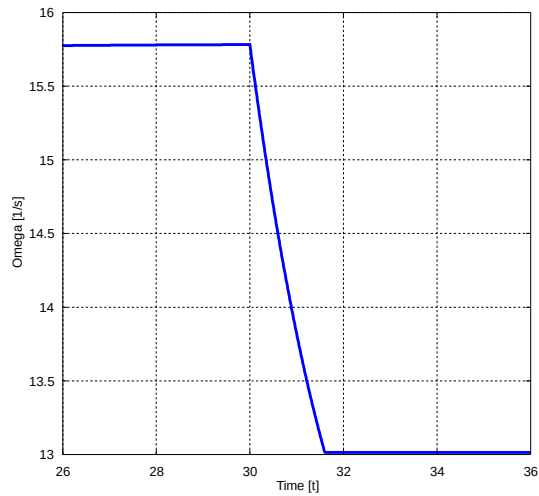


Figure 5.8: Step response

The plot shows that the reference value, in this case $\omega_{ref}=13$ rad/s, is reached after under 2s. Clearly, a fast response has been achieved without compromising the stability of the system.

5.7.2 MPPT

This section shows the response of the MPPT Simulation introduced in section 5.5. Different wind speed inputs have been applied as well and the response of the closed-loop system using a proportional controller is shown in the figure below. The input variation has been chosen to vary significantly so that the response characteristics can be seen more clearly. The input is shown in blue and the rotational speed in green. Clearly, the controller is keeping the speed constant at a lower speed than the no-load speed. It has been verified that the output at $v_w=12$ m/s corresponds to the optimal shaft speed of the experiment shown in chapter 4.2.

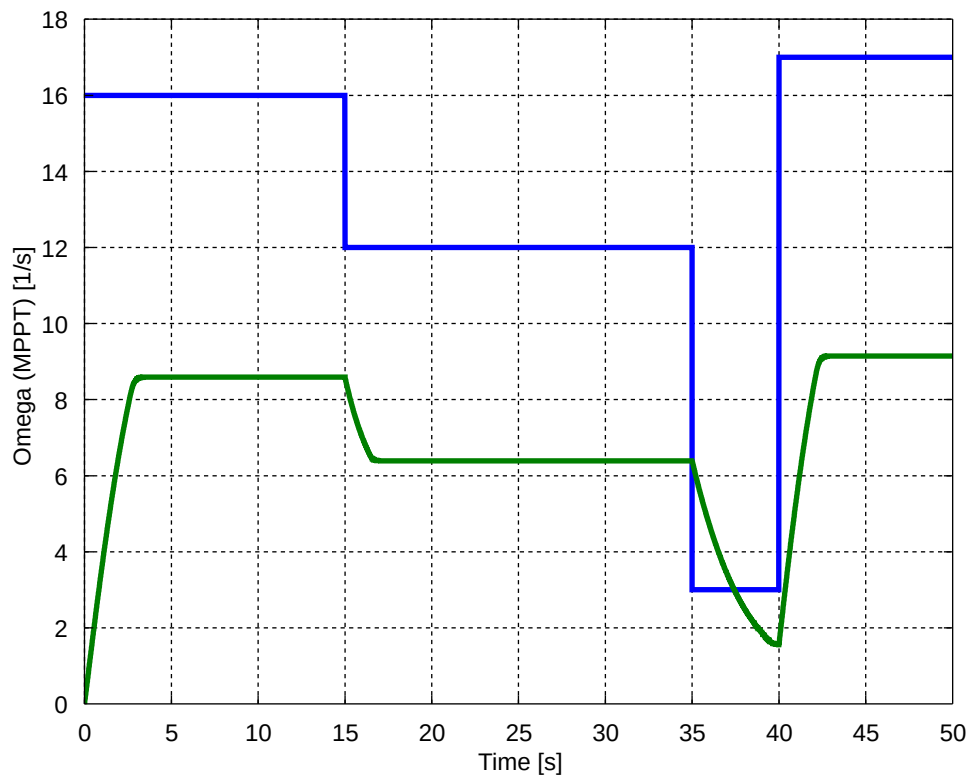


Figure 5.9: MPPT mode

6. Conclusions

In this chapter, the research aims set in Chapter Two as well as the attainments in this work are reviewed first. The section following then highlights the original contribution to current knowledge. Finally, the chapter finishes with concluding remarks and recommendations for future work.

6.1 Review of objectives and attainment

The achievements from the research goals defined in Chapter Two are discussed in this section, along with any limitations encountered.

Aim 1.a – Development of a novel sensory system/ power stage

For prior investigations, a novel test bench prototype was developed requiring a novel interfacing system to a HIL I/O card. Available building blocks of software had to be considered as well as hardware requirements and ratings. One of the hardware constraints concerned the selection of a suitable sensor for the low-speed motor driven application and the recovery time of the sensor since a digital sensor was favoured. The sensor has to be able to follow a high enough resolution suitable for the prototype. Furthermore, the signal availability in Quarc software blocks were considered. These constraints were met by the US Digital Encoder unit E5 which provides a resolution of 4096 steps per revolution, a sufficiently fast recovery time and the correct type of encoder signal needed for connection with the Q2-USB card. Digital filtering and signal processing could be achieved with an Embedded Matlab function, taking an averaged derivative by summing up encoder differences and dividing by the sampling time.

The next decision had to address whether the power stage should be driven by an analogue or a digital signal. A DAC has to match the load to be driven; furthermore, a different HIL system had been utilized initially which did not provide a DAC channel. A novel power stage was designed which utilizes a double motor driving IC, the L298. However, despite not having reached the maximum ratings, it was found that the driving voltage became unstable which brought up the necessity to provide a secondary power stage for stabilization purposes. The MOSFET IPP80CN10NG was selected as well as a fast recovery diode MBR2045CT for dissipating the induced voltages from the electromagnet. With this combined configuration, the loads can be driven.

Aim 1.b – Development of a brake model for the setup

A literature review at the beginning of Chapter Three revealed the electromagnetic braking torque of a slowly rotating wind turbine to be linearly dependant on the rotational speed as well as the square of the B-field. Measurements were taken and errors calculated, considering propagation of uncertainty, and compared with a formula developed by

Wouterse for the low-speed region. Despite the differing geometry of the magnet cores, only a deviation of 1.3% was found. This model was utilized in the simulations for controller development.

Aim 1.c – Controller development

For the test bench design simulation, the model had to be completed by adding the DC motor drive. The parameters of the first-order system were determined by calculating the averages of sets of measurements. A complete model was presented which also had to include a PWM loss function due to the PWM inducing eddy currents in the soft iron core. The model response was compared to the hardware response and a transport delay was added for an unmodelled slip-stick effect. Furthermore, it was found that the motor had to be driven with $V_m=12V$ in order not to include a strong frictional component present at lower speeds. With the motor model deployed at $V_m=12V$ and the brake design, a controller was developed by utilizing a modified Ziegler-Nichols tuning suited for a saturating system. Due to the significantly smaller prototype design, the setup was sensitive to oscillations, particularly to a PI controller driving the system into saturation. The PI gains retrieved from the Ziegler-Nichols tuning could be verified in the HIL experiment and therefore an automated controller design procedure for future designs could be established.

Aim 2 – Development of a novel numerical wind turbine model for a laboratory setup

Chapter Four describes the laboratory setup of a VAWT cross-flow prototype and how an experiment with the wind turbine, power transmission, as well as a variable power resistor load could provide data for use in an analytical model of the wind turbine system. Different modelling techniques were evaluated and compared in terms of suitability for the control design, and the analytical model chosen. The latter was tested using different inputs and the resulting rotational shaft speed was compared to the experiment, validating the model for the wind speeds tested.

Aim 3.a – Requirement analysis

For the brake rating, a rough estimate of the braking power needed for the wind turbine prototype was obtained first to be able to dimension the parameters of the brake. The brake model developed by Wouterse was used for the estimate as it showed satisfactory accordance when compared to the braking parameter developed in Aim 1.b. It has been concluded that two magnets suffice to stop the turbine at a wind speed of $v_w=15$ m/s. A requirement analysis has been based on the expected turbine performance at a wind speed of $v_w=20$ m/s which is assumed to be never reached in an urban environment. With a rough estimate of the turbine inertia and a maximum required speed difference of $\Delta\omega=4$

rad/s, a minimum settling time of $\Delta t=4s$ has been set as a control requirement for the speed control modes considered in this thesis.

Aim 3.b – Development of a control scheme for braking to a reference speed

This goal has been achieved by building a complete model of the plant first and performing a manual tuning using proportional control. The plant in the simulation consists of the analytical WT model developed in Aim 2, along with an equivalent shaft model, as well as a scaled brake model using the parametric equation developed by Wouterse. A closed-loop form with ω being the controlled variable has been created with a logic element deciding when to switch on the brake. The rotational speed has been arbitrarily set to $\omega=10$ rad/s as the recommended rotor speed limitation has to be verified in an experiment. The proportional gain was found to be $K_p=500$.

Aim 3.c – Development of a simulation for MPPT control

The model for this mode has been developed based on the plant model explained in Aim 3.b. A closed-loop was formed as well, in this case, however, with λ being the controlled variable. The reference TSR has been set to $\lambda=0.35$ which was given by a data fit provided in Chapter Four and by the condition that the sinusoidal expression reaches its maximum. Like in Aim 3.b, the same controller gain yielded satisfactory results.

Aim 3.d – Performance evaluation

For both modes, different wind speed inputs with varying amplitudes as well as slopes have been utilized to verify the controller developed. In speed control mode, the controller is only switched on when the maximum allowable rotor speed has been reached. It has been found that no steady-state error remains. Likewise in MPPT mode, the rotational speeds are kept constant at the appropriate optimum rotational speed shown in the experimental speed-power curves plotted in Chapter Four. Since the speeds are held constant as soon as a threshold is exceeded, there are no response delays. A final test has been undertaken which required slight modification of the simulation to be able to simulate a step input with a reference speed yielding a large speed difference to be braked, such as in emergency situations. It showed that the settling time of $\Delta t \approx 1.5s$ met the requirement set in Aim 3.a well and that no steady-state error remains.

6.2 Original contribution to knowledge

In this section, the contributions achieved for each research aim are listed.

Contribution 1.a – Development of a novel sensory system/ power stage

A novel test bench design has been developed which can be utilized in further experiments such as for developing a plant model of an eddy current brake with a laminated steel core,

using a fast frequency PWM. Also, a model can be developed for the high-speed region, provided a DC motor with a different gearing ratio is deployed.

Contribution 1 b - Development of a brake model for the setup

A brake model has been developed for the low speed region of the test bench setup. In the process of comparing different models, it was discovered that the experimentally found parameter corresponded well to the model developed by Wouterse despite differing geometries.

Contribution 1 c - Controller development

A HIL design regime has been suggested which has proved to enable fast prototyping of a controller. It is expected that this regime can be deployed for adapting or newly developing a controller for different SSWT designs.

Contribution 2 – Development of a novel numerical wind turbine model for a laboratory setup

A novel WT model based on an experiment has been developed and verified. The development procedure shown can be utilized for future designs such as when experimental data is available or, more importantly, when CFD input-output data is available since WT designs are easily created or modified and simulated in CFD.

Contribution 3.a - Requirement analysis

An example calculation of the required brake parameters as well as the control requirements have been presented which are adaptable to any new VAWT design.

Contribution 3.b - Development of a control scheme for braking to a reference speed

This research goal constitutes an innovative software-based model for braking to rotational reference speeds when a set rotor speed should not be exceeded.

Contribution 3.c - Development of a simulation for MPPT control

Deploying a magnetic brake adds the advantage of the SSWT to be operated in optimum power extracting conditions since precise control can be achieved when using a digitally controlled brake. This contribution provides a novel software-based model for MPPT using an eddy current brake.

An innovative controller has been developed for the previous applications with the added advantage of straightforward implementation in an embedded controller design for stand-alone operation.

6.3 Conclusions and future recommendations

This section finishes with concluding remarks and possibilities for future development.

Conclusion 1.a - Development of a novel sensory system/ power stage

The power stage was intended for digital control using a PWM, however, the magnets were developed by a different designer who assumed a DAC was going to be utilized. With a laminated steel core and a high frequency PWM, it is expected to yield a higher braking torque characteristic due to the fast changing magnetic field.

Conclusion 1.b – Development of a brake model for the setup

In this form, the test bench deploying a DC motor drive could not yet serve as a scaled equivalent model for the turbine. However, with rising armature voltages, a DC motor exhibits a speed-torque characteristic similar to that of wind turbine systems where rising wind speeds are related to rising speed-torque curves. Several works have attempted to control a DC motor drive such that the behaviour of a wind turbine is emulated [72] [73]. Such a configuration can be used if access to a wind turbine testing facility is not available. However, the test bench model developed could be deployed for experimental evaluation of the proportional brake model parameter and for developing an efficient controller design procedure using HIL technology.

Conclusion 1.c - Controller development

With the use of a precise model in Simulink, a controller can be quickly developed with a Ziegler-Nichols tuning without imposing any risk on the actual hardware to find a marginally stable proportional controller. Without a model, automated HIL testing using iteration allows gradual increasing of controller gains and setting small intervals for each iteration.

Conclusion 2 - Development of a novel numerical wind turbine model for a laboratory setup

The analytical model found has shown accurate results when deployed in the simulation and compared to the experimental data available. However, it is strongly recommended to obtain more data in order to validate the model further or for the development of a new model. In particular, it is suggested to retrieve multiple datasets for each rotational speed combined with a torque output at a particular wind speed to provide an average for each steady-state value of ω and T . Furthermore, it is suspected that at higher rotational speeds, vibrations of significant amplitude in the setup may cause inaccuracies in the model and induce unwanted dynamics in any experiment. The setup may possibly be improved by embedding the bearings of the wind turbine in a rubber bed. Another recommendation concerns the detailed model developed in Chapter Four which includes the shaft dynamics on the generator side. The parameters such as the stiffness or the dampening coefficient are still missing which requires the development of an experiment, ideally using the wind turbine setup. At last it is suggested for future development with the prototype to utilize a common sensor card for the cobra probe (wind speed measurement) and the torque

transducer in order to synchronize the measurement if transient data is needed. It is also recommended to develop a method for determining the dynamics of the rotor from the first-order start-up behaviour of the wind tunnel fan.

Conclusion 3.a - Requirement analysis

The requirement analysis only included a calculation for the settling time. Since the wind turbine is slow to react to changes induced by the brake, it is not expected that an integral controller will be needed in other designs and hence, no overshoot percentage has to be provided in the requirement analysis.

Conclusions 3.b – 3.c - Braking to a reference speed and MPPT

In chapter 5.6, a supervisory control regime has been suggested for use in an embedded microcontroller. However, as mentioned before, supervisory control can also be implemented in Simulink using the Stateflow designer.

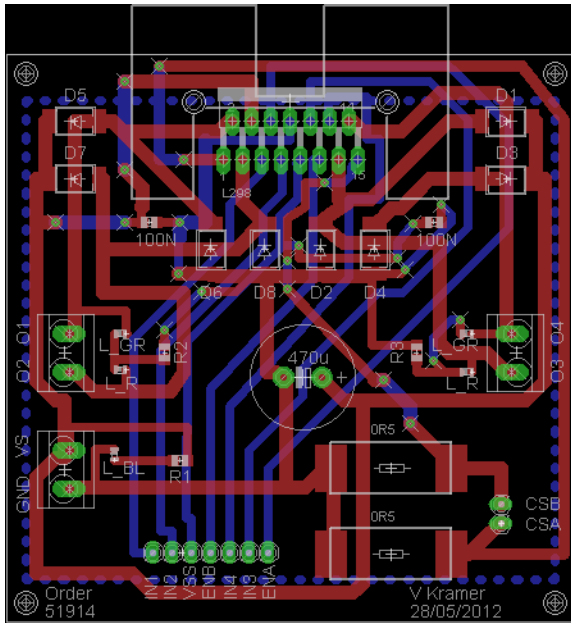
Conclusion 3.d - Performance evaluation

The simulations of the above control modes provided satisfactory results; however, a HIL validation experiment is missing in this work which provides opportunities for future development.

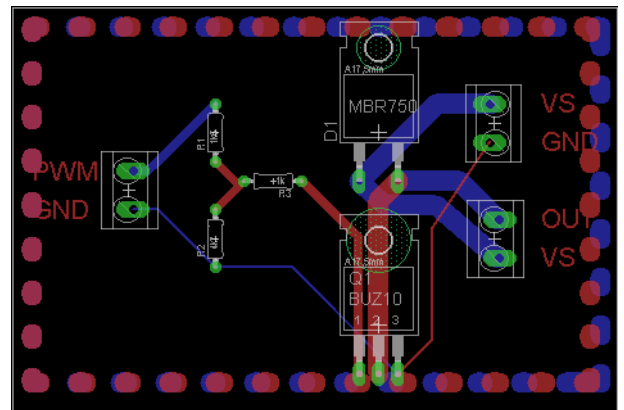
Appendices

Appendix 1 - L298 Driving PCB and MOSFET PCB

Note that the command 'ratsnest' has not been executed so that the signals are shown. Both top and bottom side include a ground polygon indicated by the surrounding dashed line.



L298 Driving PCB



MOSFET PCB

Appendix 2 – Test bench parameters

%% Brake parameters

```
d=4e-3; %thickness of disk [m]
l=4e-2; %length of square core [m]
x=6.5e-3; %length of air gap [m]
R=8.25e-2; %distance from rot. axis to middle of iron core [m]
rho=0.0286e-6; %specific resistance of aluminium [Ohms*m]
my0=1.257e-6; %magnetic field constant [Vs/Am]
N=1000; %number of windings [-]
L_a=36e-3; %inductance of coil [H]
```

%% Motor parameters

```
R_a=10; %Armature Resistance
L_a=7.53e-3; %Armature inductance (measured)
T_fr=15e-3; %friction torque [Nm] (measured)
J=4.3e-3; %moment of inertia (rotor, disk, shaft, adapt.)
% (rough estimation)
k_g=0.565; %calculated generator constant of motor [Vs]
```

%% Parameters according to Wouterse

```
d=4e-3; %thickness of disk [m]
L=4e-2; %length and width of magnet core cross-section [m]
D=sqrt(L^2*2); %diagonal of magnet core cross-section [m]
```

```

x=6e-3;           %length of air gap [m]
R=8.25e-2;       %distance from rot. axis to middle of iron core [m]
rho=0.021e-6;   %specific resistance of aluminium [Ohms*m]
A=10e-2         %disk radius
C=1/2*(1-1/4*1/((1+R/A)^2 * ((A-R)/D)^2))
                %geometric parameter C
c_Wou=R^2*C*pi/(rho*4)*D^2*d
                %proportional parameter calculation

```

Appendix 3 - Wind turbine and scaled brake parameters

```

%% Scaled brake parameters
d=0.8e-2;       %thickness of disk [m]
x=1.2e-2;       %air gap [m]
A=30e-2;       %eddy disk radius [m]
R=26.4e-2;     %radius to centre point of action for net force [m]
D=6e-2;        %"diagonal" of core [m]
rho=0.02e-6;   %specific resistance aluminium alloy [Ohms*m]
R_m=6;         %Resistance magnet [Ohms]
V_m=15;        %Exciting voltage for magnet [V]
I_m=V_m/R_m;   %Exciting current [A]
N=1000;        %windings of magnet [-]
B=N*4*pi*1e-7*I_m/x %magnetic B-field [T]
C=1/2*(1-1/4*1/((1+R/A)^2 * ((A-R)/D)^2))
                %geometric parameter C

```

Bibliography

- [1] I. Munteanu et al, *Optimal Control of Wind Energy Conversion Systems*. London: Springer-Verlag, 2008.
- [2] M. Laughton, *Renewable electricity and the grid: the challenge of variability*. USA/ Canada: Earthscan, 2007.
- [3] J. Björnstedt, M. Ström, "Power Electronic Voltage And Frequency Control For Distributed Generation System," Lund University, Sweden, 2005.
- [4] "MIT study on the future of the electric grid."
- [5] "IEA Energy Statistics - for Electricity/Heat." [Online]. Available: <http://www.iea.org/stats/prodresult.asp?PRODUCT=Electricity/Heat>. [Accessed: 20-Apr-2012].
- [6] "Small-scale wind energy - Carbon Trust." [Online]. Available: <http://www.carbontrust.com/resources/reports/technology/small-scale-wind-energy>. [Accessed: 18-Jan-2015].
- [7] I. Troen, E. L. Petersen, *European Wind Atlas*. Risø National Laboratory, Roskilde: DTU National Laboratory, Denmark, 1989.
- [8] "IEA Energy Statistics - for Electricity/Heat." [Online]. Available: <http://www.iea.org/stats/prodresult.asp?PRODUCT=Electricity/Heat>. [Accessed: 02-Mar-2012].
- [9] H. Riegler, "Wind turbine research/ HAWT versus VAWT." [Online]. Available: <http://www.victordanilochkin.org/research/turbine/>. [Accessed: 21-Apr-2012].
- [10] M Tutar, G Oguz, "Large eddy simulations of wind flow around parallel buildings with varying configurations," *Fluid Dyn. Res.*, vol. 31, pp. 289–315, 2002.
- [11] "Ch B Page 265: Sustainable Energy - without the hot air | David MacKay." [Online]. Available: http://www.inference.phy.cam.ac.uk/withouthotair/cB/page_265.shtml. [Accessed: 29-Sep-2012].
- [12] "Fish hold the key to better wind farms | MNN - Mother Nature Network." [Online]. Available: <http://www.mnn.com/earth-matters/energy/stories/fish-hold-the-key-to-better-wind-farms>. [Accessed: 29-Sep-2012].
- [13] "Generator Ratings & Capacity Factors: Why You Should Avoid Them." [Online]. Available: <http://www.wind-works.org/articles/generatortratingandcapacityfactors.html>. [Accessed: 20-Apr-2012].
- [14] T. Burton, D. Sharpe, N. Jenkins, E. Bossanyi, *Wind Energy Handbook*. West Sussex, England: John Wiley & Sons, LTD, 2001.
- [15] D. J. MacKay, "Ch B Page 263ff: Sustainable Energy - without the hot air | David MacKay." [Online]. Available: http://www.inference.phy.cam.ac.uk/withouthotair/cB/page_263.shtml. [Accessed: 20-Apr-2012].
- [16] "Betz Limit - Wind." [Online]. Available: <http://www.reuk.co.uk/Betz-Limit.htm>. [Accessed: 14-May-2015].
- [17] S. Eriksson et al, "Evaluation of different turbine concepts for wind power," presented at the *Renewable & Sustainable Energy Reviews*, vol. 12 (2008), pp. 1419–1434.
- [18] G. Colley, R. Mishra, H.V.Rao, R.Woolhead, "Effect of rotor blade position on Vertical Axis Wind Turbine performance," *Eur. Assoc. Dev. Renew. Energ. Environ. Power Qual. EA4EPQ*, 2010.
- [19] A. Kadam, S. Patil, "A Review Study on Savonius Wind Rotors for Accessing Power Performance," *J. Mech. Civ. Eng.*, pp. 18–24.
- [20] S. M. Barakati, "Modeling and Controller design of a Wind Energy Conversion System Including a Matrix Converter," University of Waterloo, Canada, Ontario, 2008.
- [21] J.-Y. Park, S. Lee, T. Sabourin, K. Park, "A Novel Vertical-Axis Wind Turbine for Distributed & Utility Deployment," Korea.
- [22] E. Hau, *Windkraftanlagen: Grundlagen, Technik, Einsatz, Wirtschaftlichkeit*, 4th ed. Berlin, Germany: Springer.
- [23] "Wind Power - Vortexis Engineering." [Online]. Available: <http://www.vortexis.com/vortexis-engineering.html>. [Accessed: 14-Apr-2016].

- [24] F. Blaabjerg, Z. Chen, *Power Electronics for Modern Wind Turbines*. Denmark: Morgan & Claypool Publishers, 2006.
- [25] M. Bredsdorff, "Et batteri til en elbil koster 60.000 kroner | Ingeniøren." [Online]. Available: <http://ing.dk/artikel/et-batteri-til-en-elbil-koster-60000-kroner-109887>. [Accessed: 23-Jul-2013].
- [26] Y. D. Song, B. Dhinakaran, X. Y. Bao, "Variable speed control of wind turbines using nonlinear and adaptive algorithms | ResearchGate," 2000.
- [27] G. Colley, "Design, Operation and Diagnostics of a Vertical Axis Wind Turbine," University of Huddersfield, 2012.
- [28] C. J. Ramos et al, "Current control in the grid connection of the double-output induction generator linked to a variable speed turbine," presented at the IECON 02, 2002, pp. 979–984 vols.2.
- [29] Plamen Valentinov Yankov et al, "Successive Resistive Braking Circuit for Permanent Magnet Wind Turbine Generators," presented at the 14th International Power Electronics and Motion Control Conference, 2010, pp. T11-27-T11-31.
- [30] Niall M. McMahon et al, "On Electrodynamical Braking for Small Wind Turbines," *Wind Eng.*, vol. 39, no. 5, pp. 549–555, 2015.
- [31] Frank Jespen et al, "Disturbance Control of the Hydraulic Brake in a Wind Turbine," presented at the Energy Conference and Exhibition, 2010, pp. 530–535.
- [32] Estiko Rijanto et al, "Development of a Hydraulic Brake Control System for 100kW Horizontal Axis Wind Turbines using Pressure Relief and Directional Valves," *Int. J. Appl. Eng. Res.*, vol. 7, no. 4, pp. 383–396, 2012.
- [33] I. H. Jee et al, "A Magnetic Brake for Small Wind Turbines," *J. Magn.*, vol. 17, no. 1, 2012.
- [34] P. Mongeau, "Wind turbine generator having an eddy current brake, wind turbine having such a generator, and associated methods," US20140110947 A1, 24-Apr-2014.
- [35] "Bremseinrichtung einer Windkraftanlage und Verfahren zu deren Betätigung - Dokument DE19634464C2." [Online]. Available: <http://www.patent-de.com/19980716/DE19634464C2.html>. [Accessed: 17-Apr-2016].
- [36] "A Student's Guide to Maxwell's Equations." [Online]. Available: <http://www4.wittenberg.edu/maxwell/chapter3/problem4/>. [Accessed: 03-Jan-2013].
- [37] L. C. Davis, J. R. Reitz, "Eddy Currents in Finite Conducting Sheets," 1971, vol. 42, pp. 4119–4127.
- [38] D. Schieber, "Braking torque on rotating sheet in stationary magnetic field," in *IEEE Proceedings, The Institution of Electrical Engineers*, 1974, vol. 121, pp. 117–122.
- [39] W. R. Smythe, "On Eddy Currents in a Rotating Disk," in *IEEE Transactions*, 1942, vol. 61, pp. 681–684.
- [40] J. Jin, *Theory and Computation of Electromagnetic Fields*. Wiley-IEEE Press, 2011.
- [41] H. D. Wiederick et al, "Magnetic braking: Simple theory and experiment," in *American Journal of Physics*, Ontario, Canada, 1987, vol. 55, pp. 500–503.
- [42] L. Cadwell, "Magnetic damping: Analysis of an eddy current brake using an airtrack," Rhode Island, 1996, vol. 64, pp. 917–923.
- [43] J. H. Wouterse, "Critical torque and speed of eddy current brake with widely separated soft iron poles," in *IEE Proceedings-B*, 1991, vol. 138, pp. 153–158.
- [44] H. Scherf, *Modellbildung und Simulation dynamischer Systeme*, 4th ed. Oldenburg Verlag, 2010.
- [45] E. Simeu, D. Georges, "Modeling and control of an eddy current brake," in *Control Engineering Practice*, 1996, vol. 4, pp. 19–26.
- [46] P. Brauneis, "Praxisphase," University of Applied Sciences, Frankfurt, Germany, 2012.
- [47] MathWorks, "Simulink Coder." [Online]. Available: <http://www.mathworks.com/products/simulink-coder/>. [Accessed: 25-Apr-2012].
- [48] "Q2-USB User Manual." [Online]. Available: http://www.adaptech.com/IMG/pdf/Q2-USB_User_Manual.pdf. [Accessed: 23-Apr-2012].
- [49] Quanser, "QUARC Windows Target :: QUARC." [Online]. Available: http://www.quarcservice.com/ReleaseNotes/files/quarc_windows_target.html. [Accessed: 25-Apr-2012].

- [50] "Communicating with the Target :: QUARC Targets." [Online]. Available: http://www.quarcservice.com/ReleaseNotes/files/quarc_target_communication.html#target_uri. [Accessed: 25-Apr-2012].
- [51] "Choosing a sensor to measure rotation - Electronic Products." [Online]. Available: http://www2.electronicproducts.com/Choosing_a_sensor_to_measure_rotation-article-SEPCHER1-sep1999-html.aspx. [Accessed: 27-Apr-2012].
- [52] E. Ramsden, *Hall-Effect Sensors: Theory and Applications*, 2nd ed. Elsevier/ Newnes, 2006.
- [53] "US Digital | Products » E5 Optical Kit Encoder." [Online]. Available: <http://usdigital.com/products/e5>. [Accessed: 02-Oct-2012].
- [54] R. Mancini, *Op-Amps for Everyone*. Texas Instruments, 2002.
- [55] U. Probst, *Leistungselektronik fuer Bachelors*. Carl Hanser Verlag, 2008.
- [56] "CadSoft EAGLE PCB Design Software - EAGLE Shop, Support, Tutorials." [Online]. Available: <http://www.cadsoft.de/?language=de&lang=en>. [Accessed: 19-Sep-2012].
- [57] STMicroelectronics, "L298 datasheet - Dual full-bridge driver." .
- [58] "SFE Footprint Library Eagle - Open Circuits." [Online]. Available: http://www.opencircuits.com/SFE_Footprint_Library_Eagle. [Accessed: 26-Apr-2012].
- [59] "PCB Printed Circuit Board File Creation Calculator | Advanced Circuits." [Online]. Available: <http://www.4pcb.com/trace-width-calculator.html>. [Accessed: 18-Apr-2016].
- [60] "Fusion PCB Service [PCB08511P] - \$9.90 : Seeed Studio Bazaar, Boost ideas, extend the reach." [Online]. Available: <http://www.seeedstudio.com/depot/fusion-pcb-service-p-835.html>. [Accessed: 19-Sep-2012].
- [61] "Power MOSFET Basics - Power_MOSFET_Basics.pdf." .
- [62] Ivers-Tiffée, von Muench, *Werkstoffe der Elektrotechnik*, 9th ed. Teubner.
- [63] "ME 422 Ziegler." [Online]. Available: <http://www.calpoly.edu/~fowen/me422/ZieglerNichols.html>. [Accessed: 03-Jul-2013].
- [64] K.-S. Park, "Optimal Design o a Micro Vertical Axis Wind Turbine for Sustainable Urban Environment," University of Huddersfield, 2013.
- [65] Wind Blue Power, "Permanent Magnet Alternator Wind Blue Low Wind." [Online]. Available: http://www.windbluepower.com/Permanent_Magnet_Alternator_Wind_Blue_Low_Wind_p/dc-540.htm. [Accessed: 22-Jul-2013].
- [66] "TFI - Cobra Probe." [Online]. Available: <http://www.turbulentflow.com.au/Products/CobraProbe/CobraProbe.php>. [Accessed: 25-Jan-2015].
- [67] S. B. Choi et al, "LQG Control of a CFD-based Aeroelastic Wing Model," in *Decision and Control, 2003. Proceedings. 42nd IEEE Conference on*, 2003, vol. 5, pp. 4939–4944.
- [68] Q. Meng et al, "CFD assisted modeling for control system design: A case study," *Simul. Model. Pract. Theory*, vol. 17, no. 4, pp. 730–742, Apr. 2009.
- [69] Jorge L. Acosta, Saša Ž. Djokić, "Assessment of Renewable Wind Resources in UK," presented at the MELECON 2010 - 2010 15th IEEE Mediterranean Electrotechnical Conference, Valletta, pp. 1439–1444.
- [70] "State Machine - Stateflow - Simulink - MathWorks United Kingdom." [Online]. Available: http://uk.mathworks.com/products/stateflow/index.html?s_tid=gn_loc_drop. [Accessed: 23-Apr-2016].
- [71] "megaAVR Microcontrollers." [Online]. Available: <http://www.atmel.com/products/microcontrollers/avr/megaavr.aspx>. [Accessed: 23-Apr-2016].
- [72] S. M. El-Hakim et al, "Small wind turbine emulator with separately excited DC motor using analog electronic circuit," presented at the Renewable Power Generation, IET Conference on, 2011, pp. 1–6.
- [73] Trevor Hardy, Ward Jewell, "Emulation of a 1.5MW wind turbine with a DC motor," presented at the 2011 IEEE Power and Energy Society General Meeting, 2011, pp. 1–8.
- [74] S. Kuntoff, "Savonius Rotor." [Online]. Available: http://commons.wikimedia.org/wiki/File:Savonius_Rotor.png#mediaviewer/File:Savonius_Rotor.png. [Accessed: 21-Jan-2015].

- [75] "Darrieus wind turbine." [Online]. Available:
http://en.wikipedia.org/wiki/Darrieus_wind_turbine#mediaviewer/File:Darrieus.jpg.
[Accessed: 21-Jan-2015].
- [76] T. Knott, "Angle of attack." [Online]. Available:
http://commons.wikimedia.org/wiki/File:Angle_of_attack_two.png#/media/File:Angle_of_attack_two.png. [Accessed: 05-May-2015].